Measurement of the $\sqrt{s}$ Dependence of Isolated Direct Photon Production in Proton-Anitproton Collisions

A Dissertation

Presented to

The Faculty of the Graduate School of Arts and Sciences

Brandeis University

Physics Department

James Bensinger, Advisor

In Partial Fulfillment
of the Requirements for the Degree
Doctor of Philosophy

by

Dana Partos

May 2001

%noindent fulfillment of the requirements for the degree of

%begincenter

ABSTRACT

Measurement of the $\sqrt{s}$ Dependence of Isolated Direct Photon Production in $p\bar{p}$ Collisions

A dissertation presented to the Faculty of the
Graduate School of Arts and Sciences of Brandeis
University, Waltham, Massachusetts

by Dana Partos

We present a measurement of the $\sqrt{s}$ dependence of isolated prompt photon production in hadronic collisions. Prompt photon samples from 1.8 TeV and 0.63 TeV $p\bar{p}$ collisions were recorded with the Collider Detector at Fermilab. Two independent background subtraction methods, shower shape and conversion rates, were calibrated and used to calculate the photon cross sections. The measured shapes of the cross sections as a function of photon transverse momentum are consistent with each other yet disagree with current calculations of perturbative Quantum Chromodynamics (QCD). When comparing the cross sections as a function of photon x_T ($=2P_T/\sqrt{s}$), the two cross sections disagree by more than 3 σ. Therefore, the parameterized parton distributions of the proton are excluded as an explanation of the discrepancy between data and theory.

Contents

List of Tables

List of Figures

Chapter 1

Theory

1.1 Introduction

Currently, the best understanding of the fundamental constituents of matter and their interactions is expressed in a theory called the standard model. The theoretical foundations of the standard model were developed in the 1960's and 70's and has been extensively tested experimentally. When predictions can be made, the experimental agreement with theory has been excellent.

The standard model contains a number of free parameters that can only be obtained from experimental measurements, such as particle masses and the distribution of fundamental particles within the proton. The standard model's predictive power can be increased with precision measurements of those free parameters. For example, a precise measurement of the rate at which photons are produced in proton-antiproton collisions gives a better understanding of the gluon distribution within the proton.

1.2 Standard Model

In the standard model, there are three types of fundamental particles that interact through three forces [1]. The three types of particles are leptons, quarks, and gauge bosons. The three forces are called the strong force, the weak force, and the electromagnetic force. At the present time, the fourth known force, the gravitational force, has not been quantized and incorporated into the standard model. In addition, for every known particle there is an antiparticle counterpart, which has an identical mass and spin but the opposite electric charge. For example, the negatively charged electron's (e^-) antiparticle is the positively charged positron (e^+).

The lepton group is composed of six distinct particles which can be paired into three families. Each family consists of one electrically charged massive particle and one electrically neutral, essentially massless particle called a neutrino. The charged leptons, listed in order of increasing mass, are called electron (e), muon (μ), and tau (τ), and each carry an electric charge of -1. The corresponding neutrinos are then the electron neutrino (ν_e), the muon neutrino (ν_μ), and the tau (ν_τ) neutrino. Leptons are classified as fermions because they have a half integer spin and obey Fermi-Dirac statistics. The leptons only participate in electromagnetic and weak interactions. Table 1.1 lists the three families of leptons and their properties.

Quarks, like the leptons, are fermions. They come in six varieties, known as flavors, called up (u), down (d), charm (c), strange (s), top (t), and bottom (b). The quarks can be arranged in three families of weak isospin doublets. Along with carrying an electric charge, which is a precise fraction of an electron's charge, all quarks have a "color" charge of red, blue, or green. This color charge allows quarks to interact through the strong force. The quarks and their properties are listed in Table 1.2 [2].

The final group of fundamental particles are the carriers, or mediators, of the forces known as the gauge bosons. The gauge bosons are spin 1 particles and obey Bose-Einstein statistics. The carrier of the electromagnetic force is the photon. The weak force is mediated by three vector bosons, W^+, W^-, and Z^0, and gluons are the carriers of the strong force. They carry color characteristics in color-anticolor pairs. Since there are three basic colors one would naively expect that there are nine gluons, one for each color combination. However, because gluons obey $SU(3)$ symmetry, there is a "color octet" consisting of linear combinations of color-anticolor pairs and a color singlet. The color singlet state has not been found to exist in nature so there are only eight types of gluons [1]. The strength of each force is given by its coupling constant, α, and the average distance over which it acts is given by its range. The bosons and their properties are listed in Table 1.3.

All particles found in nature are colorless, and therefore, quarks must be bound together through the strong force to form hadrons. The are two possible ways to form a colorless combination. One way would would be for a quark of one color (red) and an antiquark of that same color (antired) to combine to form a type of particle known as a meson. One of the more common mesons is the π^+ which consists of a u quark and a $\bar{d}$ quark. A particle containing one quark of each color is also considered to be colorless. The three quark combinations are known as baryons. The most common baryons are protons (uud) and neutrons (udd). One consequence of the requirement that all particles must be colorless is that all particles end up having a whole unit of electric charge.

The standard model uses gauge theories to mathematically describe how the forces interact with the fundamental particles. Gauge theories are a special class of quantum field theories in which an invariance principle requires the existence of interactions among the particles. The gauge theory of electromagnetism, called Quantum Electrodynamics (QED), describes the photon mediated interactions of electrically charged particles. In QED the electric charge of an interaction must be conserved. The electromagnetic force is proportional to $1/r^2$, where r is the distance between the interacting particles, and its range is infinite.

In Quantum Chromodynamics (QCD), it is the color charge which must be conserved. QCD is modeled after QED and describes the gluon-mediated strong interactions. The strong force is proportional to r so as quarks move further apart, the force binding them together increases in strength. This is due to the fact that gluons themselves carry a color charge. This allows gluons to couple to themselves. Each time gluons emit other gluons, the strength of the color force is increased. Therefore, the longer the interaction, the more gluons can be emitted, and the stronger the force. In short range interactions, where the strength of the strong force is relatively small, the perturbation techniques can be applied to QCD processes.

1.2.1 Quantum Chromodynamics

The three main quarks that make up the proton are known as valence quarks. In addition to the valence quarks, other quarks are continually being created and destroyed inside the proton. Those quarks are called "sea" quarks. The sea quarks appear as virtual $q\bar{q}$ pairs, being quickly created and annihilated in the vacuum. The quarks are held inside the proton by a sea of gluons. Because both quarks and gluons make up some part of the proton, they are often referred to as "partons."

In order to illustrate a high energy collision process, consider the case where proton and antiproton collide to produce a photon and a quark [3]. Because proton-antiproton collisions are extremely complex and very difficult to describe mathematically, many assumptions must be made and mathematical techniques used to simplify the problem. One of the most basic assumptions used in that in high energy hadron collisions, called factorization, is that during a collision one parton from the proton interacts with just one parton from the antiproton. In this case the two partons that collide are a quark and a gluon. The quark and gluon are said to participate in a "hard scattering" process. The rest of the quarks and gluons are considered to be "spectator" partons. The hard scattering part of the collision can be dealt with mathematically using perturbation techniques. What happens to the spectator partons cannot be described using perturbation methods because they deal with the relatively low energy structure of the proton. All of that information must be extracted from experimental data. Detailed knowledge of the quark and gluon content of the proton (number and type of quark and what fraction (x) of the proton's momentum each parton is likely to have) is put into parton distribution functions (PDF).

One consequence of using the factorization technique is that an arbitrary momentum scale, the factorization scale, is introduced to the equation. The factorization scale is an artificial, non-physical parameter that exists only to simplify the mathematical description of what occurs in hadron-hadron collisions. The factorization energy scale is typically chosen to be approximately the produced photon's momentum, which is representative of the scale of interaction (Q^2). Any dependence of the resulting cross section on the factorization scale should be minimized if the calculation is done correctly.

In order to calculate the hard scattering part of the photon production cross section perturbatively, all possible final states containing a photon must be considered. The simplest final state, the leading order calculation, is a photon plus a single quark. It is also possible for that quark to radiate a gluon. In order to radiate a gluon, the quark must participate in another strong interaction. This puts another factor of α_s in the calculation. It is necessary to sum over all possible higher terms as well as all the different types the quarks and gluons. In addition, all possible parton momenta must be integrated over to produce a total cross section.

The complexity of the calculation makes it impossible to sum all the higher order terms in the calculation. This leads to unphysical results because the inifinities from the momentum integration no longer cancel. In order to resolve this problem, a mathematical method known as renormalization occurs. Renormalization removes the infinities, but it adds another arbitrary momentum scale known as the renormalization scale. The renormalization scale and factorization scale come from independent origins so they do not have to have exactly the same value, but they are often chosen to be the same.

The final thing to consider is what happens to the outgoing particles after the hard scattering occurs. As the particles move apart, the energy required to separate them increases. Eventually, enough energy builds up to produce quark-antiquark pairs from the vacuum. The new quarks recombine with themselves and with the original quarks to produce hadrons. The quark-antiquark pairs are created until the original energy is dissipated. This process is known as hadronization or fragmentation, and it results in a "jet" of particles. There is a finite probability of obtaining any given particle from parton fragmentation. Again, these probabilities (fragmentation functions) cannot be calculated in perturbative QCD and must be modeled from experimental data. A third scale, the fragmentation scale, is also introduced.

The probability of obtaining a parton a (b) from hadron A (B) with a momentum fraction between x and $x + dx$ is denoted by the distribution function $G_{a/A}(x)$ (Fig. 1.1). The probability of obtaining a hadron C with a momentum fraction between z and $z + dz$ is denoted by the fragmentation function $D_{C/c}(z)$. The cross section for parton-parton hard scattering is calculated in the lowest order of perturbation theory. The expression for the invariant cross section is given by:

$$\begin{aligned}
&E_C \frac{d\sigma}{d^3p_C}(A + B \rightarrow C + X) = \\
&\quad \sum_{abcX} \int dx_a dx_b dz_c G_{a/A}(x_a) G_{b/B}(x_b) D_{C/c}(z_C) \frac{\hat{s}}{z_C^2 \pi} \frac{d\sigma}{d\hat{t}}(a + b \rightarrow c + X) \\
&\quad \times \delta(\hat{s} + \hat{t} + \hat{u})
\end{aligned} \tag{1.1}$$

The δ function follows simply from the two-body phase kinematics for massless particles. Furthermore, the initial and final partons have been assumed to be collinear with the corresponding initial and final hadrons, i.e. no parton transverse momentum smearing has been included.

In the specific case of photon production, the final state photon is free from the complication of fragmentation. The photon is seen in the final state exactly as it was produced from the parton level interaction. This is an important advantage of the study of direct photon production. In contrast, jet production analyses suffer from ambiguities in reconstructing a parton from a spray of hadrons.

1.3 Prompt Photon Theory

The study of prompt photons gives experimentalists a useful tool for testing QCD. Photons are a clean signal which can be measured relatively easily and accurately by experimentalists. Due to their production mechanism, they are a useful way to learn about the gluon distribution within the proton.

There are two main ways that prompt photons can be produced in proton-antiproton collisions (see Fig. 1.2). The first way is when a quark and antiquark annihilate to produce a photon and a gluon. The second way is the QCD analogue to Compton scattering. In that case a quark scatters from a gluon producing a photon along with the scattered quark. For this type of Compton scattering to occur, the gluons do not need a large fraction of the proton's momentum. Since there is a large number of low momentum gluons inside the proton, this is the dominant method for producing low energy photons. To produce photons with an energy greater than approximately 100 GeV, the initial particles must have a high momentum. Quarks typically have a larger fractional momentum than the gluons so quark-antiquark annihilation is the dominant production mechanism for high energy photons. Because of the importance of Compton scattering, prompt photon production measurements are sensitive to the gluon content of the proton. The Compton scattering cross section can be written as

$$\frac{d\sigma}{dt}(qg \to q\gamma) = -\frac{\pi\alpha\alpha_s}{3s^2}e_q^2\frac{u^2+s^2}{su} \tag{1.2}$$

and the annihilation cross section can be written as

$$\frac{d\sigma}{dt}(q\bar{q} \to g\gamma) = \frac{8\pi\alpha\alpha_s}{9s^2}e_q^2\frac{u^2+t^2}{ut} \tag{1.3}$$

where e_q is the charge of the interacting quarks in units of the electron charge and $s, u,$and t are the Mandelstam variables.

Higher order diagrams as shown in Fig. 1.2 involve either initial or final state gluon radiation. The characteristic experimental signature is a photon plus two or more jets. Current QCD calculations only go up to the 2 jet level (order α_s^2), known as next-to-leading order (NLO), while experimental measurements include all the higher orders unless an explicit cut is made. These measurements are, therefore, known as inclusive. The NLO predictions should agree with inclusive measurements as long as all higher order terms are small, which is one of the assumptions that allows perturbation techniques to be used in the first place.

1.3.1 Bremsstrahlung Component and Isolation

One other source of single photons is bremsstrahlung radiation from an initial or final state quark [4]. These photons are not considered to be prompt photons as they are not produced directly from the proton-antiproton interaction, but their existence affects the way prompt photons are measured and modeled theoretically.

Because bremsstrahlung photons tend to be collinear with the quark, and therefore the jet, from which it radiated, an isolation requirement can be very useful. The isolation requirement is typically implemented by measuring the amount of energy in a cone surrounding the photon and requiring that the energy be smaller than a certain amount. Since bremsstrahlung photons are usually near jets, they have a large amount of energy in their isolation cone and will be removed. This requirement, unfortunately, can do nothing to remove bremsstrahlung photons that are radiated at a large angle with respect to the jets. Therefore, theoretical calculations include a bremsstrahlung/fragmentation component which is then partially removed by an isolation cut matching that of the experiment. This component contributes a large fraction (more than 50%) of the total non-isolated rate, which is reduced to $15-20\%$ after the isolation cut has been applied [5].

The isolation cut serves another important purpose in reducing the possibility that a jet is misidentified as a photon. During the fragmentation process it is possible for a single particle to gain most of the parton's energy. If that particle is a neutral meson, like the π^0 or η, that can decay to two photons, the decay product may be indistinguishable from a single photon. The isolation cut can reduce the probability that a multi-photon decay product is misidentified as a photon. While only one in 10^3-10^4 jets fragments this way, the dijet production cross section is 10^3-10^4 times larger than the photon cross section. Therefore, the rate at which single particle jets are produced is similar to the rate at which prompt photons are produced. A major part of any photon analysis involves finding ways to reduce that background.

1.3.2 Current Issues in Prompt Photon Theory

One issue that still needs to be resolved in QCD is the reason for the discrepancy between measured and theoretically predicted photon cross sections at both fixed target and collider experiments [5]. The theories tend to underestimate the number of low energy photons which alters the shape of the cross section. These discrepancies cannot be globally corrected by either a change in the normalization or factorization scales or by changing the gluon density functions.

One method of resolving this issue is by applying a transverse (k_T) smearing correction to momenta of the initial partons. The current theories assume that the partons inside the proton solely have longitudinal momentum. If, however, the partons do have a small amount of initial transverse momentum, then "softer" photons can be detected as a result of an enhancement in the photon P_T spectrum. The extra energy is assumed to have a Gaussian dependence and the choice of the average amount of initial transverse energy is typically determined by dimuon, dijet, and diphoton pair transverse momentum. The applications of the k_T corrections have successfully bridged the gap between data and theory.

Some theorists are trying to find the physical source of the extra transverse energy [6]. The extra transverse momentum can come from either the non-perturbative effects from parton binding and intrinsic transverse momentum or from additional hard multiple gluon emissions which can be calculated perturbatively. NLO calculations can be corrected to all orders through the techniques of gluon resummation or a parton showering algorithm. At the present time, the parton showering algorithm has had more success predicting the behavior of high energy photon cross sections.

1.4 Variables for Hadron Collider Physics

It is necessary to define a set of quantities which are used in the study of high energy hadron-hadron collisions. While the standard phase space variables of energy (E), momentum (P), polar angle (θ), and azimuthal angle (ϕ) can be used, the nature of hadron colliders makes the introduction of additional quantities necessary.

An important feature of hadron colliders is that while the hadrons can be given equal and opposite momenta, there is an inherent uncertainty in the momenta of the partons which interact. Therefore, in the lab (detector) frame, the momenta along the beam axis (defined to be in the z direction) will not usually sum to zero, and the overall system will be Lorentz boosted.

In the transverse $(x - y)$ plane, however, the final state momenta will cancel, as the initial state transverse momenta are negligible. Therefore, the *transverse* momentum and energy are defined as:

$$P_T \equiv \sqrt{p_x^2 + p_y^2} \tag{1.4}$$

which become important variables for collider physics. If the particle mass $m \ll E$, or for massless particles such as the photon,

$$E_T = P_T = E \sin\theta \tag{1.5}$$

The Lorentz boost also motivates a Lorentz invariant alternative to the polar angle θ called the *rapidity* (y):

$$y = \frac{1}{2} \ln \left(\frac{E + p_z}{E - p_z} \right) \tag{1.6}$$

which transforms under a Lorentz boost as $y \rightarrow y+$ [constant], thereby preserving the shape of the rapidity distribution under the boost. Again, if a particle's mass is much less than its energy, it can be simplified to form the *pseudorapidity* (η):

$$\eta = -\ln \tan \left(\frac{\theta}{2} \right) \tag{1.7}$$

Thus a pseudorapidity of $\eta = 0$ corresponds to $\theta = 90^\circ$ from the beam (z) direction, increasing to ∞ $(-\infty)$ as the angle grows nearer to the beam line. Since the condition $m \ll E$ is a good approximation for high energy jets and photons, the pseudorapidity is used almost exclusively, and is often referred to as the rapidity.

Particle	**Symbol**	**Charge**	**Mass** (MeV/c^2)
Electron	e	-1	0.511
Electron neutrino	ν_e	0	$< 3 \times 10^{-6}$
Muon	μ	-1	105.66
Muon neutrino	ν_μ	0	< 0.19
Tau	τ	-1	1777
Tau neutrino	ν_τ	0	< 18.2

Table 1.1: The three generations of leptons.

Particle	**Symbol**	**Charge**	**Mass** (MeV/c^2)
Up	u	+2/3	1-5
Down	d	-1/3	3-9
Charm	c	+2/3	1150-1350
Strange	s	-1/3	75-170
Top	t	+2/3	170000
Bottom	b	-1/3	4100-4400

Table 1.2: The three generations of quarks.

Particle	**Force**	**Coupling** (α)	**Range**
Photon (γ)	Electromagnetic	10^{-2}	∞
W^+, W^-, Z^0	Weak	10^{-13}	$< 10^{-16}$ cm
Gluon	Strong	1	$< 10^{-13}$ cm

Table 1.3: The standard model contains four vector bosons which carry the electromagnetic, strong, and weak forces. The coupling constant (α) is given as the strength at 10^{-13} cm in comparison with the strong force. The range is the average distance over which the forces act.

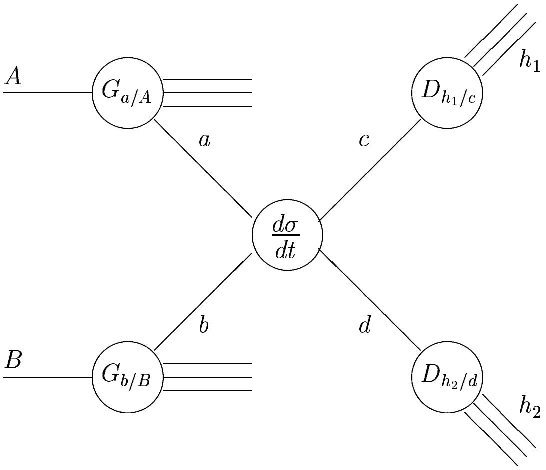

Figure 1.1: Schematic representation of a high P_T reaction factorized into parton distribution functions (G), parton fragmentation functions (D), and a hard scattering.

Gluon Compton Scattering

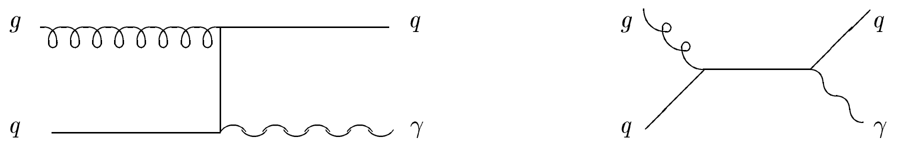

Quark-Antiquark Annihilation

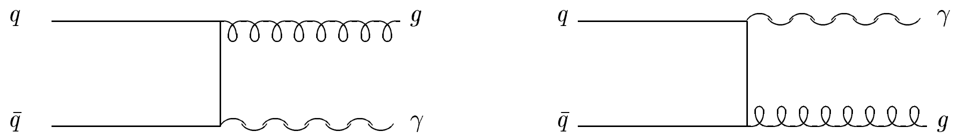

NLO Diagrams

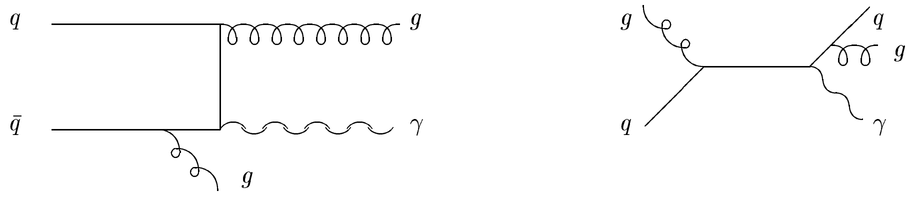

Photon Bremsstrahlung

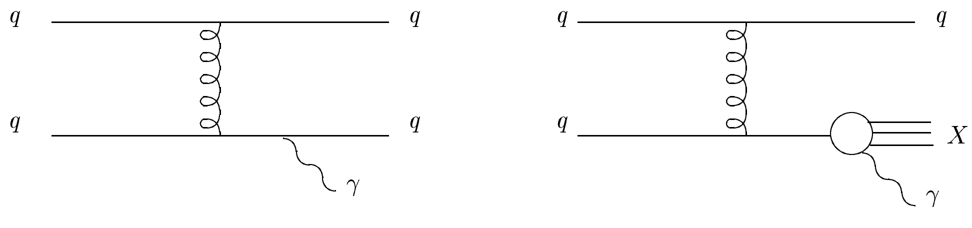

Figure 1.2: Feynman diagrams for prompt photon production.

Chapter 2

Collider Detector at Fermilab

2.1 The Tevatron

The Fermilab Tevatron collider is a large superconducting magnetic accelerator that collides bunches of protons (p) and antiprotons ($\bar{p}$). This accelerator, with a radius of 1.0 km, typically operates with 6 bunches of 900 GeV protons colliding with 6 bunches of 900 GeV antiprotons. The produced collisions have a total center of mass energy of 1.8 TeV. A diagram of the Fermilab Tevatron Accelerator is shown in Fig 2.1.

A series of steps are needed to produce the 900 GeV bunches of protons and antiprotons. The process for producing the protons starts with a bottle of H_2 gas. Two electrons are added to the gas to make H^- ions. The ions are accelerated to 750 kV by a Cockcroft-Walton electrostatic accelerator and then to 400 MeV in a 150 m linear accelerator, the Linac. At the end of the Linac, the ions pass through a copper foil to remove the electrons giving a bare proton. The protons are then put into a 475 m circumference synchrotron accelerator, the Booster, which accelerates the protons to 8 GeV. From the Booster, the protons are injected into the Main Ring. The Main Ring is a 6.3 km circumference synchrotron that accelerates the protons to 150 GeV. The Main Ring magnets are capable of generating magnetic fields up to 0.7 T to keep the protons in the ring. After reaching an energy of 150 GeV, the protons are coalesced into a single bunch and injected into the Tevatron. The Tevatron is composed of superconducting magnets which reside directly below the Main Ring magnets. The superconducting magnets can generate magnetic fields from 0.0 to 4.4 T. The Tevatron accelerates the protons to the colliding energy of 900 GeV. The entire process described above takes approximately one minute.

The process of producing antiprotons ($\bar{p}$) is more complex. A beam of 120 GeV protons is taken from the Main Ring and focused onto a tungsten target. A spray of particles is produced from which antiprotons are selected and focused with a lithium lens. The antiprotons are then passed to the Debuncher where they are stochastically cooled to reduce the phase space of the beam. From the Debuncher, the antiprotons are transfered to a concentric ring, called the Accumulator, where they are stored. The antiprotons are "stacked" at a rate of 4×10^{10} per hour until approximately 100×10^{10} antiprotons have been stored.

Six bunches of protons are injected into the Tevatron, each bunch having approximately 2×10^{11} particles. After the protons enter the Tevatron, six bunches of antiprotons are taken from the Accumulator and reverse injected into the Main Ring. Each bunch of antiprotons contains approximately 5.5×10^{10} particles. After the antiprotons reach an energy of 150 GeV, they are injected into the Tevatron. The transfer efficiency between the Accumulator and the Tevatron is low for antiprotons so by the time they reach the Tevatron, an antiproton bunch typically has dropped to 30×10^{9} particles. The proton and antiprotons bunches travel within the same beampipe but in opposite directions. They share the same magnetic and RF fields and travel in counter-rotating helical orbits.

There are two interaction regions at the Tevatron, B0 and D0, where the beams are made to collide by focusing quadrupole magnets. By colliding two beams, each with energies of 900 GeV, the center-of-mass energy available at the collision point is 1.8 TeV. Detectors enclose these interaction regions. Ideally the collisions would take place at the center of the detectors, but the actual collision point is a Gaussian distribution with a width in the x and y planes of $35\mu m$ and a width in the z plane, along the beam axis, of 30 cm. The beams traverse the Tevatron at approximately the speed of light, which means the bunch crossings occur in the interaction regions roughly every 3.5 μs. The beams are typically left to collide, "run", in the machine for approximately 10 hours. While the Tevatron is running, antiprotons are being stacked in the Main Ring. More detailed information about the Tevatron can be found in references [7] [8].

The instantaneous luminosity (L) of the Tevatron can be obtained from the following equation:

$$L = \frac{N_p N_{\bar{p}} B f_0}{4\pi\sigma^2} \tag{2.1}$$

where N_p is the total number of protons per bunch, $N_{\bar{p}}$ is the total number of antiprotons per bunch, B is the number of bunches of each type, f_0 is the frequency of bunch revolution and σ^2 is the cross sectional area of the bunches ($\sigma^2 \sim 5\times10^{-5} cm^2$). The instantaneous luminosity of the accelerator falls exponentially with time due to transverse spreading of the beam and losses from collisions.

2.1.1 The CDF Detector

The Collider Detector at Fermilab (CDF) is located at the B0 interaction region of the Tevatron. The CDF detector is a multipurpose detector which is designed to observe particles produced from high energy $p\bar{p}$ collisions. Specifically it is used to identify and measure the energy and momentum of electrons, muons, photons, and jets. Jets are sprays of particles which come from the decay of quarks and gluons created in the $p\bar{p}$ collision. A quarter view of the schematic drawing of the detector is shown in Fig 2.2. CDF is cylindrically symmetric about the transverse plane that passes through the interaction point.

The coordinate system at CDF is centered on the interaction point. The positive z-axis points along the beamline in the direction of the protons, the x-axis points horizontally toward the center of the ring and the y-axis points upwards. In terms of angles, θ is the polar angle, and ϕ is the azimuthal angle. Typically locations of particles are identified by the Lorentz invariant quantity of pseudorapidity, η. Pseudorapidity is defined in terms of the polar angle by the relation $\eta = -\ln[\tan(\theta/2)]$.

The overall design of the detector is dictated by the manner in which different types of particles interact with matter. CDF is composed of a variety of smaller detector elements. The detector can be viewed as being made up of three main functional sections; the tracking chambers, the calorimeters, and the muon chambers. Starting from the interaction point and moving radially outward, the tracking system is located inside a 1.5 m radius superconducting solenoid which produces a 1.4 T axial magnetic field. The magnetic field causes the trajectory of a charged particle to bend within the tracking chambers. The curvature of the trajectory, or “track”, is used to measure the momentum of the particle. The calorimeters surround the tracking chamber and are used to measure the electromagnetic and hadronic energy of electrons, photons, and jets. The outermost detectors are the muon detectors. Layers of steel outside of the calorimeters are used to absorb any remaining hadrons, leaving only the muons which can then be cleanly identified by the muon chambers. The following sections will give a brief overview of the detector components. A more complete description of CDF can be found elsewhere [9].

2.1.2 The Tracking Detectors

The CDF tracking system consists of three separate tracking chambers: the Silicon Vertex Detector (SVX), the Vertex Time Projection Chamber (VTX), and the

Central Tracking Chamber (CTC). All three of these detectors lie within the 1.4 T magnetic field. Each component is designed to perform a particular task. The SVX, which is closest to the beampipe, has the best position resolution and is used to identify displaced vertices. The VTX surrounds the SVX and is primarily used to identify the z position of an event's interaction point, its "vertex". Surrounding the VTX is the CTC. The CTC was designed for the precise measurement of a charged track's momentum and to give good two track separation. In addition, the absence of a track matched to an electromagnetic calorimeter cluster aids in the identification of photons.

The Silicon Vertex Detector provides precise $r-\phi$ information for the reconstruction of particle tracks. The SVX consists of two barrels that are aligned end-to-end along the beampipe. There is a 2.15 cm gap between the two barrels at $z = 0$. The total active length of the detector is 51 cm which gives a pseudorapidity coverage of $|\eta| < 1.9$. Since $p\bar{p}$ collisions occur with a spread of $\sigma \sim 30$ cm about z=0, the track acceptance of the VTX is $\sim 60\%$. Each barrel is divided into 12 azimuthal wedges of 30° and four concentric layers of silicon strip detectors. The innermost layer is at a radius of 2.86 cm and the outermost layer is at a radius of 7.87 cm from the beampipe. Each ladder has three 8.5 cm long single-sided silicon strip detectors with its readout strips running parallel to the beamline. The strips on the inner three layers have a 60 μm pitch, while the outermost layer has a 55 μm pitch. The single hit resolution per layer is approximately 13 μm with a 96% hit efficiency per layer. The SVX has a total of 96 ladders. The ladders are read out by readout chips with each chip responsible for 128 channels (strips). There are a total of 46080 channels for the entire SVX detector. This is nearly one third of all the channels for the whole CDF detector. The channels for each wedge are read out in parallel and in sparse mode, meaning that only the channels which register a hit are read out for an event. The SVX has one of the longest readout times in CDF with a typical event taking 2 ms.

Due to the high luminosities at the Tevatron, there is frequently more than one interaction per event. The Vertex Time Projection Chamber (VTX) is used to associate a track to its correct vertex along the beamline. The VTX is composed of 8 octagonal gas chambers which are segmented azimuthally. The chambers use a $50\% - 50\%$ mix of argon and ethane gas. The detector is 2.8 m long in z and extends from an inner radius of 8 cm to an outer radius of 22 cm from the beampipe. The sense wires in the chambers run radially outward from the beamline providing tracking information in the $r - z$ plane for $|\eta| < 3.5$. The endcaps consist of wires perpendicular to the beamline and the radial centerline of the wedges. Charged particles passing through the VTX ionize the gas and free electrons which drift in the axial direction to the sense wires. The axial drift time of an electron in a module provides the track position in the $r-z$ plane. The wire position gives radial information and the time of arrival to each wire position gives z information. This information for multiple tracks is used to locate the primary vertex of the event. The uncertainty in the measurement of the z coordinate of the vertex is 1 mm.

The Central Tracking Chamber (CTC) is a large cylindrical open-wire drift chamber that measured the transverse momentum of a charged particle by determining the curvature of its path in the 1.4 T magnetic field. The CTC is 3.2 m long in z, with an inner radius of 0.3 m and an outer radius of 1.3 m, giving coverage over the range of $|\eta| < 1.0$. The CTC is comprised of sense wires running the length of the chamber. There are 84 layers of wires which are grouped into 9 superlayers. The superlayers are divided into two types of alternating cells, axial and stereo. The five axial layers are cells of 12 sense wires which run parallel to the beamline and provide tracking information in the $r - \phi$ plane. The four stereo layers are cells of 6 sense wires which are offset by an angle of $\pm 3^\circ$ from the beamline. The stereo layers provide tracking information in the $r-z$ plane. The combination of the axial and stereo layers gives 3-dimensional tracking. The field wires of the CTC create a 1350 V/cm drift field. To compensate for the Lorentz angle produced by the crossed electric and magnetic fields the wires in each superlayer are grouped into cells which are tilted by 45° with respect to the radial direction. This gives drift electrons trajectories which are perpendicular to the radial direction and simplifies track reconstruction. Tracks are reconstructed by fitting hits in the CTC to a helix. The curvature of the track is related to the transverse momentum of the particle. The momentum resolution of the CTC is

$$\delta P_T/P_T = 0.002GEV^{-1} \times P_T$$

By combining tracking information from the CTC and the SVX, the momentum resolution improves to

$$\delta P_T/P_T = 0.001GEV^{-1} \times P_T$$

The CTC is also able to determine the identity of the particle by measuring the ionization rate of the particle's track.

2.1.3 Calorimetry

Particles with transverse momentum greater than 350 MeV are able to escape the magnetic field and be detected by the calorimeters which surround the solenoid. CDF has two types of calorimeters: electromagnetic and hadronic. Both types of calorimeters consist layers of an absorbing material alternating with layers of an active material. The absorbing layers cause the incident particle to interact and form a shower. The active material measures the particle's energy by sampling the energy flow as a function of depth. Electromagnetic showers develop faster than hadronic showers, therefore the electromagnetic calorimeters are positioned in front of the hadronic calorimeters. .

The calorimeters are segmented in into towers in $\eta - \phi$ space and point back to the geometric center of the detector (x = y = z = 0). The calorimeters surround the solenoid and tracking chambers and cover a range of 2π in azimuth and -4.2 to 4.2 in η. The calorimetry consists of three subsystems which are separated into pseudorapidity regions: central ($|\eta| < 1.1$), plug ($1.1 < |\eta| < 2.4$), and forward ($2.4 < |\eta| < 4.2$) calorimeters.

Central Calorimeter

The Central Electromagnetic Calorimeter is the most important device in the measurement of prompt photon characteristics. The central electromagnetic (CEM) and hadronic (CHA) calorimeters are divided into towers covering 15° in azimuth and 0.1 units in η the central calorimeter has 48 wedges each containing 10 towers. The electromagnetic section is made of alternating layers of lead and polystyrene scintillator. The hadronic section is made of alternating layers of iron and scintillator. Particles traveling through the calorimeter produce light in the scintillator which is collected by acrylic lightguides and transmitted to photomultiplier tubes located at the back of each wedge. A cutaway cross-section view of a central calorimeter wedge is shown in Fig. 2.3.

The CEM has 18 radiation lengths worth of material and an inner radius of 173 cm with a depth of 35 cm. The CHA contains 4.7 absorption lengths of material and extends beyond the CEM. The measured energy resolution for electromagnetic showers is

$$(\sigma/E)^2 = (13.7\%/\sqrt{E_T})^2 + (2\%)^2$$

The CEM was originally calibrated using testbeam electrons and is checked periodically using ^{137}Cs sources. The energy resolution for hadronic showers was measured from isolated pions to be

$$(\sigma/E)^2 = (50\%/\sqrt{E_T})^2 + (3\%)^2$$

Particles in the region $0.6 < |\eta| < 1.1$ do not pass through all layers of the CHA so an additional hadronic calorimeter, the endwall hadronic calorimeter (WHA), was added. Table 2.2 gives detailed information on the central calorimeters.

Central Electromagnetic Strip Chamber and Central Preradiator Detector

The two most important detector elements in the photon cross section analysis are the Central Electromagnetic Strip chamber (CES) and the Central Preradiator detector (CPR). In this analysis the CES and CPR are used to determine the electromagnetic shower position and to separate direct photons from the neutral meson background. The CES determines the shower position and transverse shower development at shower maximum (~ 6 radiation lengths) by measuring the charge deposition on orthogonal strips and wires. Cathode strips running in the azimuthal direction provide z information, while anode wires running in the z direction provide $r - \phi$ information. The basic orientation of the strips and wires is shown in Fig. 2.4. The CES itself is located 184 cm form the beam line, and has a total thickness of 0.75". There are two strip and wire sections per wedge. The division between the two sections is located 121.2 cm from $\eta = 0$, which corresponds to the division between the fourth and fifth towers. The strips are made of 1/16" copper backed PC boards. In towers 0-4 there are 69 1.67 cm wide strips which fill the region 6.2 to 121.2 cm from the edge $\eta = 0$. In towers 5-9 there are 59 2.01 cm wide strips which fill the region 121.2 to 239.6 cm from the $\eta = 0$ edge. The strips rest on the three piece Al extrusion that forms the base of the wire cells. There are 62 wire cells in a half section where each wire cell is 0.25" deep and 0.239" wide. The cell walls have a thickness of 0.047" (see Fig. 2.5). The wires themselves are made of 0.002" Au-plated W. All the wires but the ones on the edges are ganged in pairs so there are 64 wire readout channels per wedge. The position resolution of the CES is approximately 2 mm in each direction for 50 GeV electrons. Further details of the of the CES are listed in Table 2.3 [10].

The Central Preradiator Chambers are a set of multiwire proportional chambers sampling the early development of electromagnetic showers that begin in the solenoid magnet material. The CPR is positioned at a radius of 168 cm from the beamline between the CEM and the solenoid. The chambers have 2.22 cm cells segmented in $r - \phi$, providing $r - \phi$ view from wire readout. There are 4 chamber divisions spanning ±1 unit of pseudorapidity. The dimensions of each CPR chamber is 1.125" deep by 14.6875" wide by 45.75" long (see Fig. 2.6). The chambers have 33 ground wires alternating with 32 sense wires. The spacing between the wires is 7/32". The sense wires are kept at 1790V and ganged in pairs so there are 16 readout channels per chamber and 32 channels per wedge. The wires are sandwiched between 1/32" Cu-clad FR4 and 1/4" Hexcell in the manner shown in Fig. 2.7. Further details of the CPR are listed in Table 2.4.

Plug and Forward Calorimeters

The plug and forward calorimeters are divided into electromagnetic (PEM, FEM) and hadronic (PHA, FHA) sections. The plug and forward calorimeters use gas instead of scintillating material as their active medium. Table 2.5 gives detailed information about the plug and forward calorimeters. The plug and forward calorimeters consist of layers of proportional tubes which use a $50\% - 50\%$ mixtures of argon and ethane gas as the active medium. Each tube contains a wire, the anode, at high voltage inside a resistive plastic tube. The cathode is made of copper clad G-10 boards. The copper pads form the tower segmentation of the calorimeter. Particles passing through the detector ionize the gas in the tubes. Electrons produced by the ionization of the gas drift to the wire and induce a charge on the cathode pads. The charge is amplified and read out to give a measure of the energy in the shower.

2.1.4 The Muon Detectors

Muons are detected at CDF with arrays of drift tubes that are placed outside of the calorimeters. The lead and steel of the central calorimeters act as a filter for hadrons and prevent most non-muon particles from reaching the muon chambers. CDF has three separate muon detectors: the central muon detector (CMU), the central muon upgrade (CMP), and the central muon extension (CMX). All of the muon chambers are single wire, rectangular drift tubes.

The CMU is located inside the central calorimeter wedges, directly behind the CHA, and covers the pseudorapidity range $|\eta| < 0.6$. The CMU has only 85% coverage in ϕ due to 2.4° gaps between detector modules. Each central calorimeter wedge contains three CMU towers with each tower containing four radial layers of four drift tubes. The layers are offset from one another by half a cell width (~ 2 mm) to remove any ambiguity of which side the particles passed the wires in ϕ.

An additional 0.6 m of steel was added behind the central calorimeter to further reduce the number of hadrons which "punched-through" the CMU. Four more layers of drift tube chambers were also added called the central muon upgrade (CMP). The CMP also has drift tubes with alternate layers staggered by half a cell width to avoid gaps in coverage and left-right ambiguities. For $|\eta| < 0.6$, approximately 85% of the solid angle is covered by the CMU, 63% by the CMP, and 53% by both.

Muon detection was also extended in the $0.6 < |\eta| < 1.0$ region with the addition of four free standing conical arches of drift tubes called the central muon extension (CMX). The CMX is sandwiched between layers of scintillator (CSX) which aid in identifying real muons. The CMX covers 71% of the solid angle in the $0.6 < |\eta| < 1.0$ region. The forward section of the detector also has muon detectors, the forward muon chambers (FMU). The FMU is a toroidal muon spectrometer and is located behind the forward calorimeter.

2.1.5 Luminosity Monitors

The total integrated luminosity delivered to CDF is calculated by counting the soft interaction between two partons, called minimum bias events. Minimum bias events are the most frequent type of $p\bar{p}$ interaction at the Tevatron and account for almost all of the interactions. These events generate a spray of particles which leave the interaction point at small angles relative to the beam axis. CDF counts the minimum bias events by using small angle scintillating counters called Beam Beam Counters (BBC). The BBC covers an angular region of $0.32°$ to $4.47°$ in both the forward and backward directions. The BBC looks for at least one track on opposite sides of the detector which are at small angles to the beampipe. Coincident hits in the forward and backward BBC counters are used are used to calculate the instantaneous luminosity at CDF. The instantaneous luminosity is then integrated over time to obtain the total delivered luminosity to the CDF detector. Run 1B, which lasted from 1994-1995, had an integrated luminosity of $86.34 \pm 3.52\ pb^{-1}$. At the end of Run 1B, the Tevatron's center of mass energy was reduced to 630 GeV and data was taken for just a few months. The 630 GeV run had an integrated luminosity of $0.576\pm\ 0.025\ pb^{-1}$.

2.1.6 The Trigger System

At CDF beam beam crossings occur roughly once every 3.5 μs with an average of three interactions per crossing during Run 1B. With an event rate of 280 kHz, it is impossible to record every interaction. CDF employs a three level trigger system to reduce the event rate down to a manageable level. The goal of the trigger is to maximize the number of interesting events written to tape but minimize the amount of "dead-time", time during which the the detector does not acknowledge new interactions. The photon cross section is one of many physical processes that is a falling function of E_T. Therefore, most low energy triggers are *prescaled*, i.e.

only a fraction of the events is accepted. Each level of the trigger is a logical OR of many separate triggers which select events that have photons, muons, or jets. Each successive trigger processes fewer events than the preceeding level but with greater sophistication and more processing time. CDF's Level 1 and Level 2 triggers are implemented in hardware, while Level 3 is implemented in software.

The Level 1 trigger is deadtimeless, taking less than 3.5 μs to make its decision. The trigger is based on identification of energy clusters in the calorimeters or muon tracks in the muon chambers. Level 1 reduces the event rate from 280 kHz to 1 kHz. Photons and jets are selected at Level 1 with a calorimetry trigger which requires a single trigger tower (defined as $\Delta\eta \times \Delta\phi = 0.2 \times 15^\circ$ sections of the calorimeter) to have energy over a given threshold. The Level 1 muon triggers require a pair of hits in 2 parallel muon drift tubes. No tracking information is available at this level.

The Level 2 trigger makes use of tracking information and more sophisticated calorimeter information. The central fast tracker (CFT) is a hardware processor that uses CTC hits to reconstruct high momentum tracks in $r - \phi$. The CFT has a momentum resolution of $\delta P_T/P_T^2 = 3.5\%$. Calorimeter clusters are formed by searching for a seed tower above a certain threshold and adding in neighboring towers which are over a lower threshold. The E_T, η, and ϕ are calculated for each energy cluster. Track segment information from the CMP, CMU, and CMX detectors is also available. Tracks found by the CFT are matched to clusters from the CEM to form electron candidates or to tracks in the muon chambers to form muon candidates. Level 2 takes $\sim 20\mu s$ to make a decision during which time the detector ignores subsequent crossings. Therefore Level 2 incurs a dead-time of a few percent. The event rate out of Level 2 is approximately 20 to 35 Hz.

The Level 3 trigger is a software reconstruction trigger which is run on a farm of Silicon Graphics processors. The trigger software reconstructs events using a simplified version of the "offline" code. Level 3 implements two dimensional tracking instead of the three dimensional tracking which is used offline. All events which pass the Level 3 triggers are written to 8 mm tape with a typical output rate being 8 Hz for Run 1B.

2.1.7 Offline Reconstruction

After the events are written to tape, they are processed offline with full CDF reconstruction code. This code performs full three dimensional tracking in the CTC and identifies jet, photon, and muon candidates.

Jets are formed by finding clusters of energy in the calorimeter. The cluster starts with a seed tower which has transverse energy (E_T) of at least 3 GeV. Neighboring towers which have $E_T > 1$ GeV are added to the cluster. The adding of nearby towers continues until either there are no more towers with more than the minimum amount of energy or a maximum cluster size is reached. An energy weighted centroid is calculated for the cluster. A jet's energy is defined to be the sum of energy within a cone of radius $\Delta R = 0.4$ about the centroid. The "raw" jet energy has not been corrected for various detector effects.

Photon identification begins with a calorimeter based clustering algorithm similar to the one described for jets. A photon cluster also starts with a seed tower of at least 3 GeV of transverse electromagnetic energy (E_T^{EM}). Adjacent towers with (E_T^{EM}) > 0.1 GeV are added until a maximum cluster size is reached. A photon candidate is required to have (E_T^{EM}) > 10 GeV and a ratio of hadronic to electromagnetic energy in the cluster less than 0.125.

A muon candidate consists of a CTC track which is matched to a track segment in a muon detector. Hits in the CMU, CMP, and CMX are first fir to form track segments called stubs. The muon stubs are then extrapolated back to tracks in the CTC. Each muon stub is linked with the nearest CTC track in $r - \phi$ to form a muon candidate.

2.2 Example of a Photon Event

Figure 2.8 shows an example of a photon event display. The event display shows the energy deposited in the calorimeter as a function of η, the pseudo-rapidity, and ϕ, the azimuthal angle. A 14.3 GeV photon is located at $\eta \approx 0.5$ and $\phi \approx 300^\circ$. A jet is located 180° away from the photon.

	Central Tracking Chamber (CTC)	Vertex Tracking Chamber (VTX)	Silicon Vertex Detector (SVX)
Polar Angle Coverage	$\|\eta\| < 1.5$	$\|\eta\| < 3.25$	$\|\eta\| < 1.2$
Inner, Outer Radii	30.9,132.0	8, 22	2.7, 7.9
Length (cm)	320	280	26
Layers	60 axial, 24 stereo	24	4
Strip/Wire Spacing	10 mm	6.3 mm	$60\mu m$ (inner 3 layers) $55\mu m$ (outer layer)
Spatial Resolution	$200\mu m(r-\phi)$ $4\ mm(r-z)$	$200\mu m(r-z)$	$15\mu m(r-\phi)$
Momentum Resolution	$\delta P_T/P_T = 0.002 \times P_T$		$\delta P_T/P_T = 0.001 \times P_T$
Thickness	$\approx 0.015X_0$	$\approx 0.0045X_0$	$\approx 0.035X_0$

Table 2.1: Description of the charged particle tracking chambers.

	Central		Endwall
	EM (CEM)	Hadron (CHA)	Hadron (WHA)
Coverage ($|\eta|$)	0 - 1.1	0 - 0.9	0.7 - 1.3
Tower Size ($\delta\eta \times \delta\phi$)	$0.1 \times 15^\circ$	$0.1 \times 15^\circ$	$0.1 \times 15^\circ$
Module Length	250 cm	250 cm	100 cm
Module Width	15°	15°	80 cm
Number of Modules	48	48	48
Number of Layers	31	32	15
Active Medium	polystyrene scintillator	acrylic scintillator	acrylic scintillator
Thickness	0.5 cm	1.0 cm	1.0 cm
Absorber	Pb	Fe	Fe
Thickness	0.32 cm	2.5 cm	5.1 cm

Table 2.2: Characteristics of the central and endwall calorimeters.

Perpendicular distance to beamline	184 cm
Wire Channels (64)	
Extrusion	3 piece aluminum
Cell Dimensions	0.250 in. deep by 0.239 in.
Wall Thickness	0.047 in.
Wire Dimensions	0.002 in. Au-plated W
Readout	RABBIT
Split	121.2 cm from $\eta = 0$
Ganging	pairs except edges (1.453 cm)
Blocking Capacitor	200 pF
Strip Channels (128)	
Section 1	6.2-121.2 cm from $\eta = 0$
Strips	69 × 1.67 cm
Section 2	121.2-239.6 cm from $\eta = 0$
Strips	59 × 2.01 cm
Total Thickness	0.75 in.
	0.069 X_0
	0.022 λ
High Voltage	1420 V
Feedin	separate by logical channel
Cable	stripped RG-174
Protection	1 MΩ
Gas	95%/5% Ar/CO_2
Flow	parallel

Table 2.3: Central Electromagnetic Strip chamber characteristics. 121.2 cm from the edge ($\eta = 0$) of the module corresponds to the boundary between the fourth and fifth scintillator towers [10].

Material Seen by Transversing Particle	1/32 in. Cu-clad FR4
	1/4 in. Hexcell
	1/32 in. Cu-clad FR4
	7/16 in. 95%/5% Ar/CO_2
	1/32 in. Cu-clad FR4
	1/4 in. Hexcell
	1/32 in. Cu-clad FR4
Total Depth	1.125 in.
Total Width	14.6875 in.
Total Length	45.75 in.
Number of Grounded Field Wires/Chamber	33
Number of Sense Wires/Chamber	32
Wire Spacing	7/32 in.
Cell Size with Ganging	28/32 in.
Number of Readout Channels/Wedge	32
Chamber Gain from Fe55	32K
Source Capacitance	960 pF

Table 2.4: Description of the Central Preradiator Chambers [11].

	Plug		Forward	
	EM (PEM)	Hadron (PHA)	EM (FEM)	Hadron (FHA)
Coverage ($\|\eta\|$)	1.1 - 2.4	1.3 - 2.4	2.2 - 4.2	2.4 - 4.2
Tower Size ($\delta\eta \times \delta\phi$)	$0.09 \times 5^{\circ}$	$0.09 \times 5^{\circ}$	$0.1 \times 15^{\circ}$	$0.1 \times 15^{\circ}$
Active Medium	Proportional tube chambers with cathode pad readout			
Tube Size	$0.7 \times 0.7 cm^2$	$1.4 \times 0.8 cm^2$	$1.0 \times 0.7 cm^2$	$1.5 \times 1.0 cm^2$
# Layers	34	20	30	27
Absorber	Pb	Fe	94% PB, 4% Sb	Fe
Thickness	0.27 cm	5.1 cm	0.48 cm	5.1 cm

Table 2.5: Characteristics of the plug and forward calorimeters.

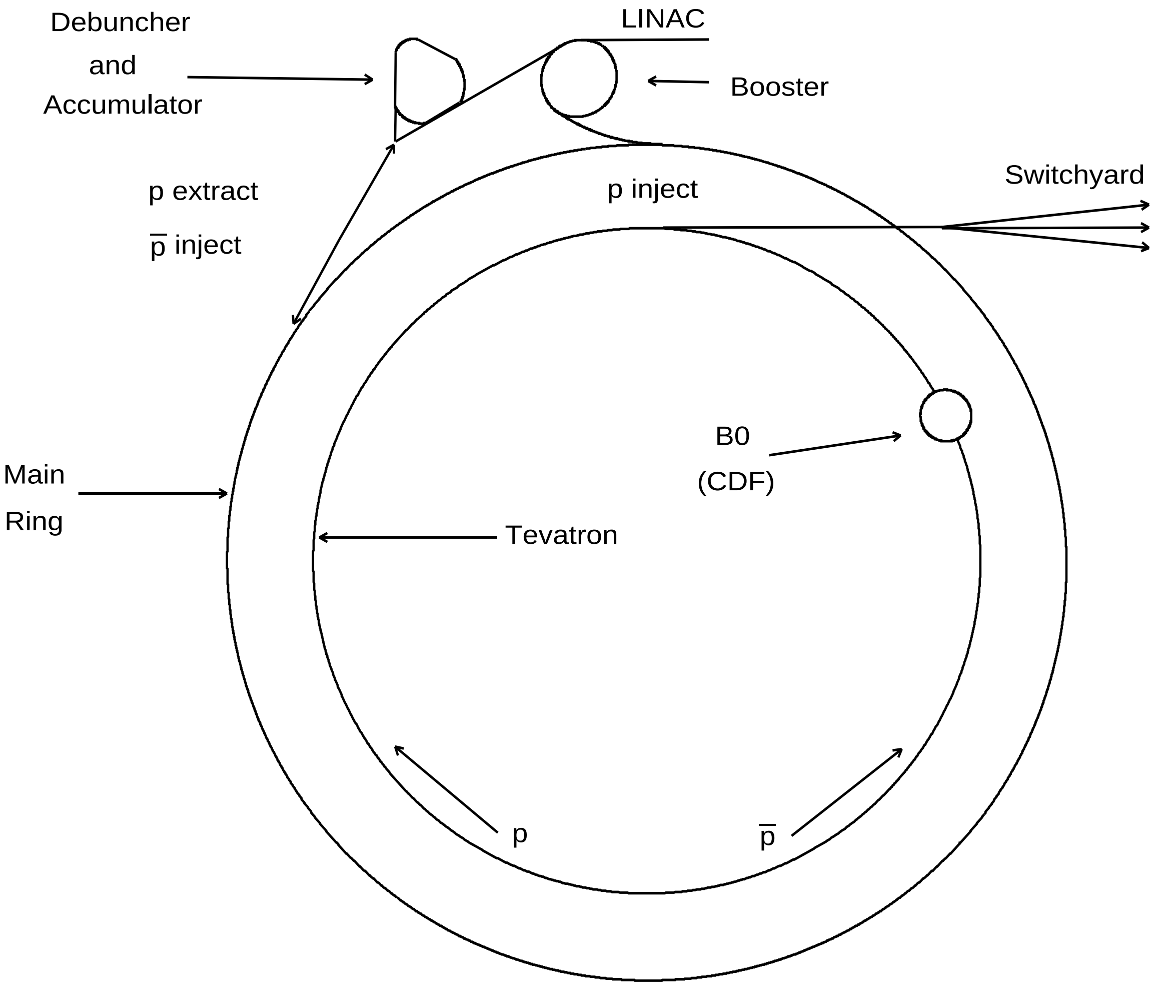

Figure 2.1: Diagram of the Tevatron accelerator complex.

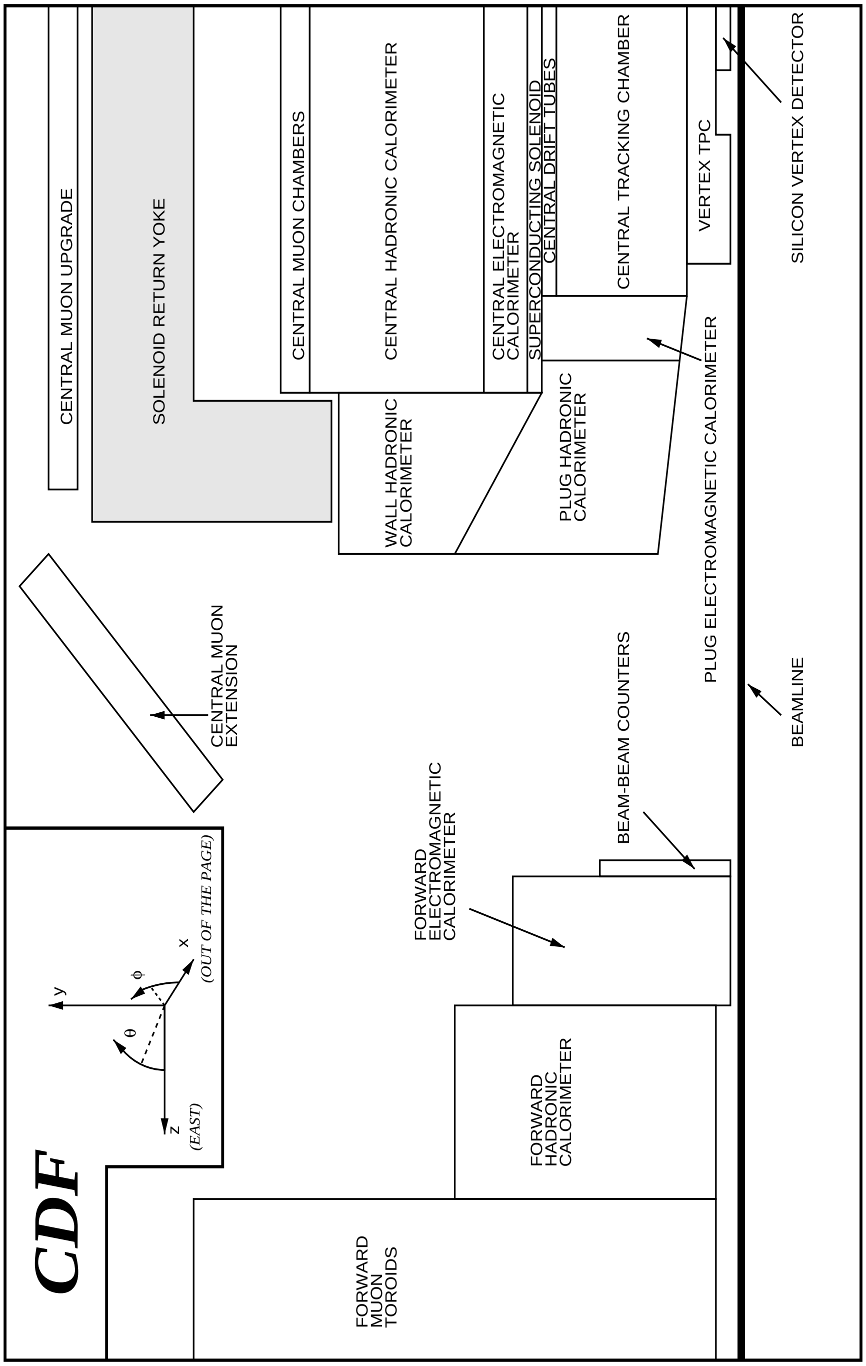

Figure 2.2: A side-view cross section of the CDF detector. The detector is forward-backward symmetric about the interaction region. The detector components are described in the text.

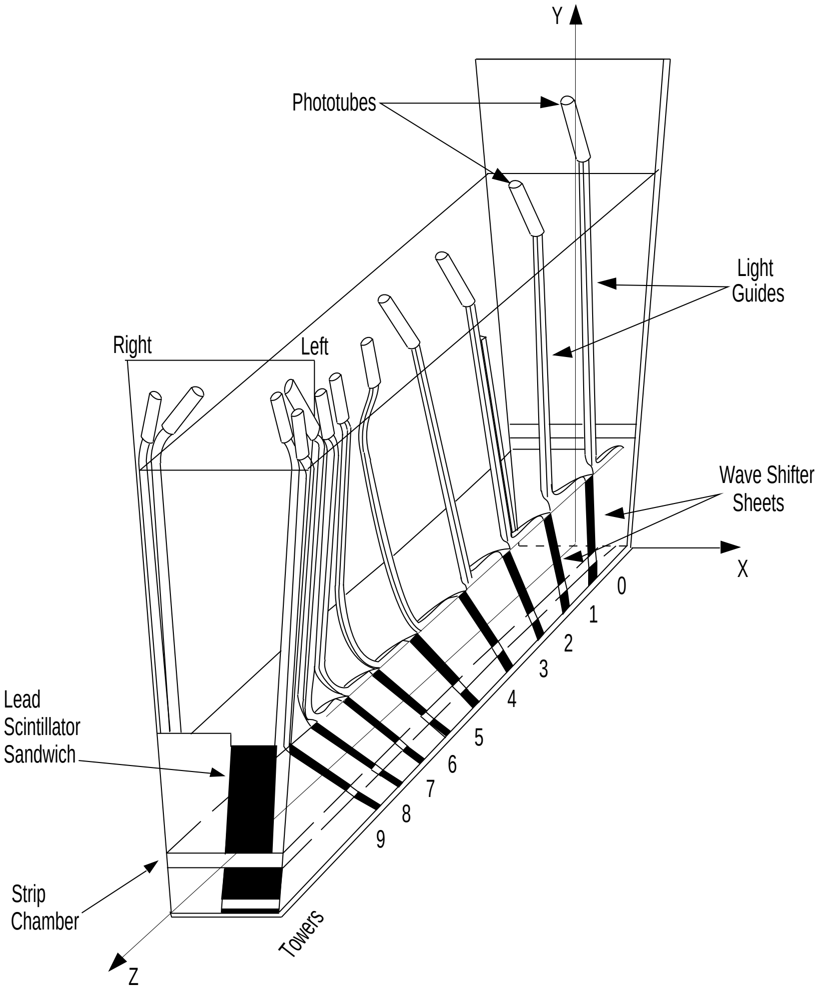

Figure 2.3: Diagram of a single calorimeter wedge.

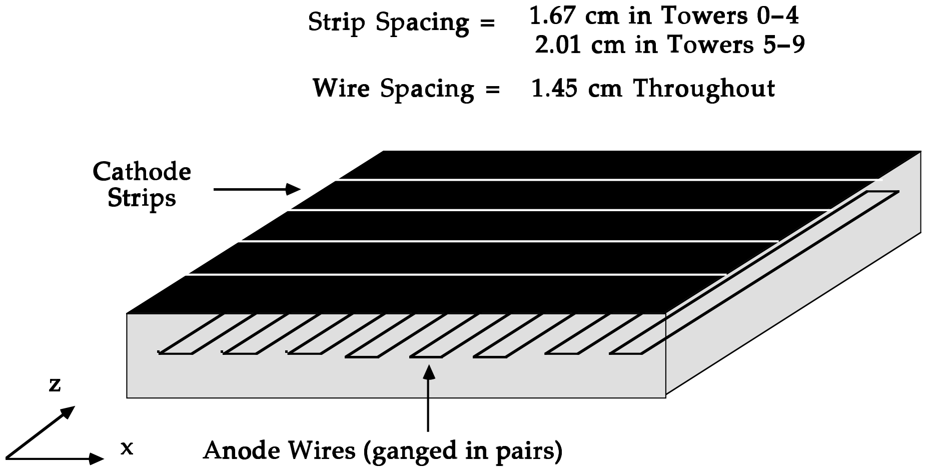

Figure 2.4: Diagram of the CES.

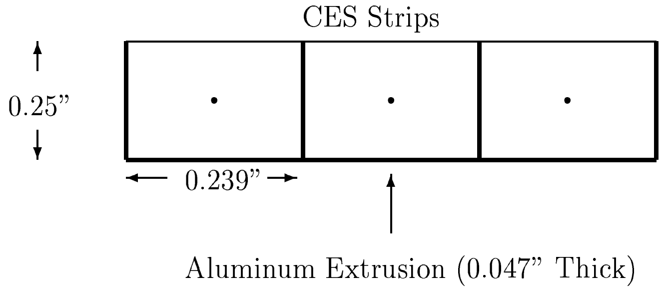

Figure 2.5: Head on view of 3 CES wire cells. The walls of the cells are made of a 0.0047" three piece aluminum extrusion. The 60 sense wires (shown in the center of the cells) in the center of the CES are ganged in pairs. The two outermost sense wires are not. This gives a total of 32 readout channels for every half wedge.

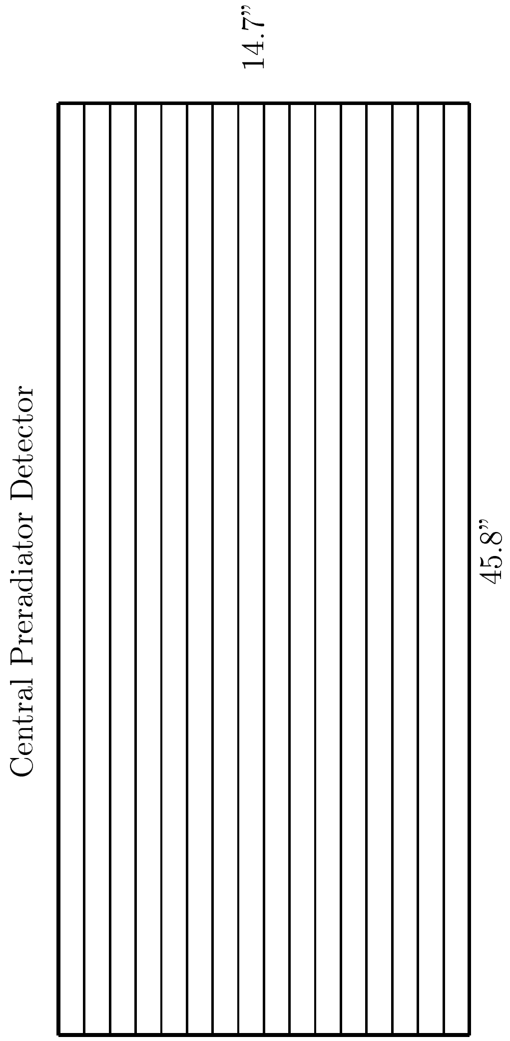

Figure 2.6: General diagram of the CPR dimensions.

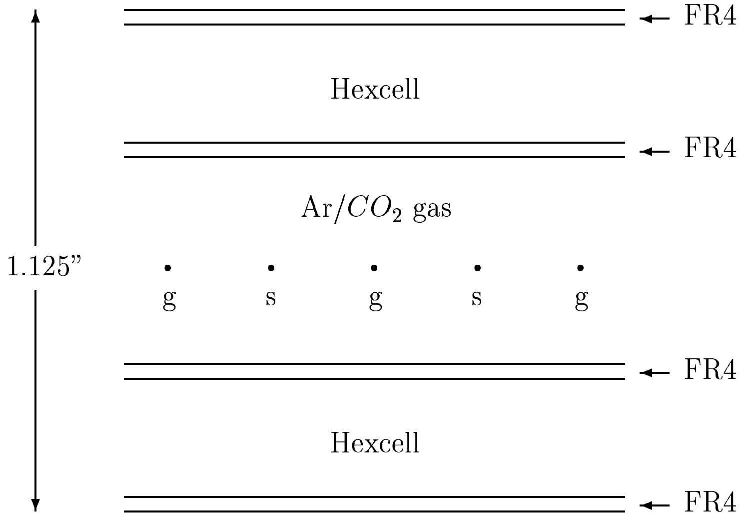

Figure 2.7: Head on view of a CPR cell drawn to scale. The circles represent the ground (g) and signal (s) wires. The two signal wires are ganged together to make one readout channel. There are 16 readout channels per CPR chamber. The full dimensions are listed in Table 2.4.

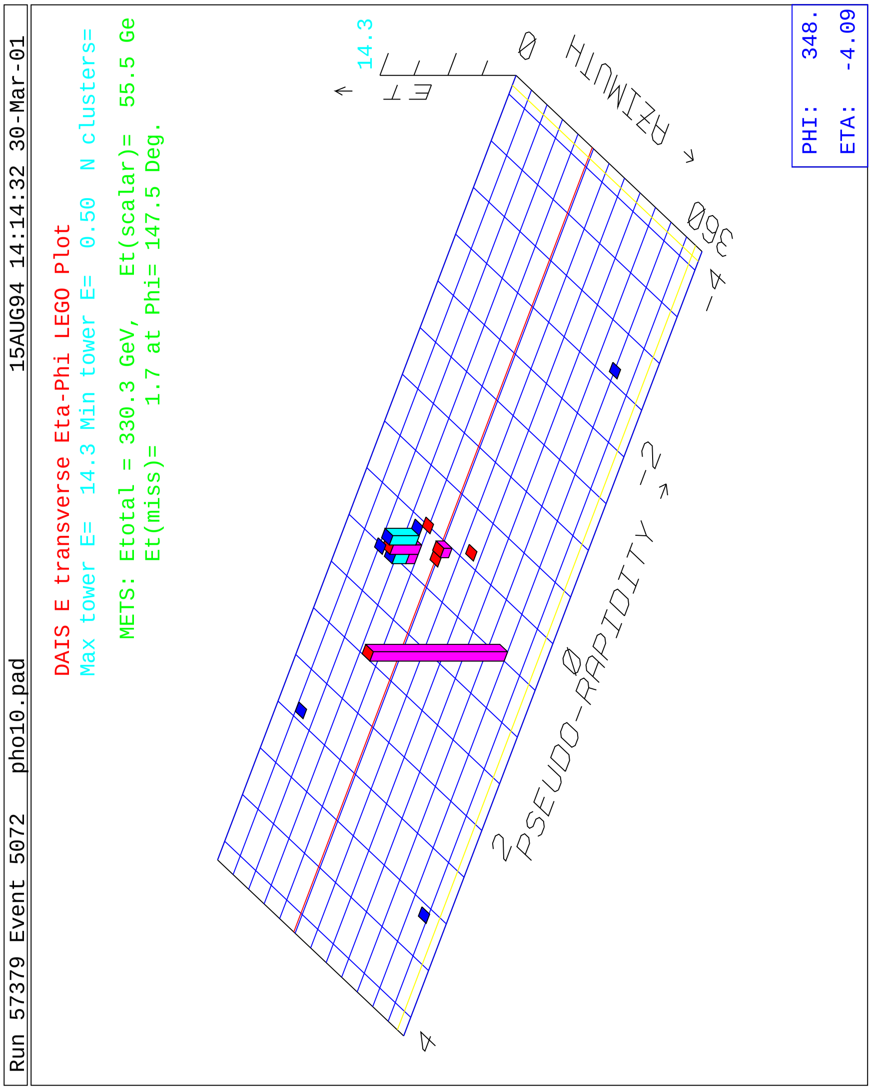

Figure 2.8: The amount of energy deposited in the calorimeter as a function of η and ϕ. A 14.3 GeV photon is located at $\eta \approx 0.5$ and $\phi \approx 300°$. A jet is located on the opposite side of the detector.

Chapter 3

Data Sample

Specific triggers were implemented to collect a sample of photons used to measure the photon cross section. As briefly mentioned previously, the photon cross section is one of the physical processes that is a falling function of E_T. Therefore, the photon trigger E_T thresholds need to be low enough to get a large sample, but high enough that the data can be reasonably stored on 8 mm tapes. To address this problem several trigger thresholds were implemented. During Run 1b the three trigger thresholds were 10, 23, and 50 GeV, and during the 630 GeV run the trigger thresholds were 6, 10, and 16 GeV. All the photon triggers had two requirements in common; the photon candidate's location is limited to the active region of the CES and the energy is primarily deposited in the EM section of the calorimeter (ratio of hadronic to electromagnetic energy less than 0.125). Above 50 GeV the rate is low enough that no further requirements are necessary, but at the lower E_T thresholds the rate is still too high and further requirements must be implemented.

As mentioned in Chapter 1, prompt photons are expected to be isolated. Therefore, the main way to reduce the rate is with the introduction of an isolation requirement. The triggers make use of two neural networks to measure the isolation energy. Two neural networks were installed so that the isolation energy of two photon candidates can be measured at the same time [12]. The neural nets work by summing energy in the nine towers surrounding the photon candidate (corresponding approximately to a cone of radius $R = \sqrt{\Delta\eta^2 + \Delta\phi^2}$ less than 0.4). If the neural net sum is less than 1552 (corresponding to an energy of approximately 4 GeV), the photon candidate is considered to be isolated and passes the trigger. As well as removing background events, the isolation cut has a dramatic effect on the rate. The 6 GeV non-isolated trigger has a prescale of 250 (only one out of every 250 events that pass the trigger are written to tape). The isolation requirement reduces the rate so that no prescale is necessary for the 6 GeV isolated trigger. The isolation cut was not quite as effective for the 10 and 23 GeV triggers. The 10 GeV prescale was reduced from 500 to 80, and the need for a prescale was eliminated for the 23 GeV isolated trigger only after a CES threshold energy requirement was added.

It is possible for real photon events to fail any of the main trigger requirements: the E_T threshold, the isolation cut, the CES energy threshold, the hadronic to electromagnetic energy ratio, and the cut on the photon candidate's location. The fraction of events that fail each one of these requirements is measured separately. The measurements of the first three failure modes for each trigger are described in detail in this chapter. The efficiency of hadronic to electromagnetic energy ratio requirement was measured in a previous analysis to be 0.992 ± 0.008 for all the triggers [13]. The requirement that the photon candidate be located in the active region of the CES will be discussed in Chapter 4.

3.1 10 GeV Isolated Photon Trigger

Data from the 10 GeV isolated photon trigger (PHOB_CEM4_10_ISOL) was used for photons in the range 11 GeV $< E_T <$ 26 GeV. It had a total integrated luminosity of 82.13 pb^{-1}. The efficiencies of two components that need to be measured are the

E_T threshold and the isolation.

3.1.1 E_T Threshold

In general the turn on efficiency is measured by finding the fraction of events from a sample with a lower E_T threshold that pass the trigger of interest. Since there are no photon samples with a lower threshold energy, we used events that passed an 8 GeV electron trigger (CEM_*8) for our test. Therefore, the E_T threshold (turn on) efficiency was defined as the fraction of 8 GeV electron events that pass the photon cuts (described in detail in the next chapter and with the exception of the no track cut) and the 10 GeV isolated photon trigger. This measurement was made difficult because the 10 GeV photon trigger was dynamically prescaled. It was 40 at the beginning of Run 1b (1 out of every 40 events that passed the trigger was written to tape) and 80 at the end of Run 1b. Therefore, the E_T turn on efficiency must be multiplied by the average prescale factor for the entire run in order to get the true efficiency. An accurate measurement of the average prescale was imperative.

The prescale was calculated using two independent methods. The first method involved using the prescale from the luminosity measurements. The prescale was stored in a file along with the luminosity for each "run", where a run is defined as the time when the the protons and antiprotons collide after being injected into the Tevatron. CDF keeps track of the the different runs by giving each run a number. We looped through a list of run numbers for all the electron events that passed the photon cuts. The prescale and luminosity was found for all the runs that were actually used in the analysis [14]. The average prescale for the 10 GeV isolated photon trigger from this method was 77.8.

The second method consisted of measuring the fraction of 23 GeV isolated photon events that also passed the 10 GeV trigger. This method has the advantage of being insensitive to any errors in the luminosity measurement. The prescale from this method is 77.2 ± 3.5 (Fig. 3.1). The two numbers are consistent within 1%. We decided to use the results of the luminosity method for two reasons; the error on the luminosity is smaller than the statistical errors on the individual points and the luminosity method used the electron data itself.

The fraction of events of 8 GeV electron events that passed the 10 GeV isolated trigger is shown in Fig. 3.2. The effects of the prescaling can be seen in the bins with efficiencies larger than one. The efficiency does essentially flatten out around one as expected. Due to the low statistics of the sample, it is not clear if the 13-14 GeV bin should be included in the plateau region. We decided to err on the conservative side and remove it from the plateau region. A flat line was fit through the bins above 14 GeV. It has a value of 1.012 ± 0.039. The efficiency above 14 GeV is therefore taken as 1.000 ± 0.039. The efficiencies for the lowest three bins have been taken as their actual value divided by the isolation efficiency (as described in the next section) with the statistical error as the error. Those values can be found in Table 3.1.

3.1.2 Isolation Efficiency

The isolation efficiency was found by looking at the neural net isolation values for the events that passed the 10 GeV non-isolated (11 GeV $< E_T <$ 26 GeV) or the 23 GeV non-isolated (26 GeV $< E_T <$ 55 GeV) photon trigger. As well as summing the isolation energy around the photon, the neural nets also store the η and ϕ of the photon candidates. The neural net ϕ values were then compared to the photon ϕ to ensure proper matching between the photon being analyzed and the one the neural net picked out. The neural net ϕ values matched the photon ϕ values 99.4% of the time for the 10 GeV non-isolated trigger and 98.5% of the time for the 23 GeV non-isolated trigger. The results of the match up and the neural net isolation energy distributions can be seen in Fig. 3.3.

After the matching was done, we measured the fraction of events that passed the neural net isolation cut (the matched neural net had an isolation value less than 1552). Because the photons and the neutral mesons which make up their background have very different isolation properties, we performed a background subtraction (described in detail in Chapter 5) to ensure we were seeing the isolation efficiencies for real photons. The events were divided into the same P_T bins as were used in the photon cross section. The fraction of events that passed the neural net isolation cut was then calculated for each bin. The efficiencies were not corrected for the events where there was a mismatch because their overall effect on the efficiencies was less than 1%. Those fractions were fit with a line (see Fig. 3.4). The fit was used to get an isolation efficiency value for each of the photon bins. The error for each bin was taken as the fractional change in the fit when the two fit parameters were both shifted by one sigma so the whole line was moved up or down.

These results were checked in two different ways. The first was to calculate the fraction of non-isolated 10 GeV events that also passed the isolated 10 GeV trigger (see Fig. 3.5). Again, the fraction had to be scaled up by the prescale. The results are consistent with the previous method. There is little P_T dependence and the values fluctuate around one. The second method is to compare the neural net isolation values with the turn on curve. Since the electron trigger did not have an isolation requirement, the turn on curve should really measure the turn on efficiency multiplied by the isolation efficiency. Figure 3.6 shows the neural net isolation results superimposed on the turn on curve. The isolation values are consistent with the statistical fluctuations of the turn on curve. The results of the isolation efficiency measurement are shown in Table 3.1. The listed turn on efficiencies in the region 11 GeV $< E_T <$ 26 GeV are the measured turn on efficiency divided by the isolation efficiency so the isolation efficiency was not double counted.

3.2 23 GeV Isolated Photon Trigger

Data from the 23 GeV isolated photon trigger (PHOB_CEM3_23_ISOL) was used for photons in the range 26 GeV $< E_T <$ 55 GeV. It had a total integrated luminosity of 83.72 pb^{-1}. The three efficiencies measured for this trigger were the E_T turn on, the isolation, and the CES energy threshold efficiency.

3.2.1 E_T and CES Energy Thresholds

The same methods used to measure the 10 GeV turn on efficiency were used to measure the 23 GeV turn on efficiency. This measurement was slightly easier because the 23 GeV isolated photon trigger was not prescaled. The turn on efficiencies were measured by finding the fraction of 10 GeV isolated photon events that passed the 23 GeV isolated photon trigger. The efficiency is shown in Fig. 3.7. The 23 GeV trigger turn on efficiency did not plateau at 1.0 as would be expected from the 10 GeV measurement. This can be explained by the fact that the 23 GeV isolated photons trigger had a CES energy threshold (XCES) requirement which the 10 GeV isolated trigger did not have. The actual plateau value 0.976 ± 0.006 is taken as the XCES efficiency and the turn on part is taken as fully efficient.

Two major issues had to be resolved about the 26-30 GeV bin. The first issue was which trigger the data should come from. Initially data from the 10 GeV trigger was used in that bin because the 23 GeV trigger was not fully efficient in that P_T region. However, we soon realized that the 23's had significantly better statistics in that bin so the overall statistical errors were reduced.

We then had to figure out if the turn on efficiency was different for photons and mesons. A combination of photons and mesons had an efficiency 0.759 ± 0.017 while photons by themselves had an efficiency of 0.811 ± 0.027. The difference was larger than expected so naturally we chose the photon only efficiency. The error was taken as half the difference between the photon and photon plus meson values so the "true" efficiency is within 2 sigma of our stated value.

The turn on and XCES efficiencies for this trigger are listed in Table 3.1. To ensure that we do not double count the statistical errors in the plateau region, we set the turn on errors equal to zero. All the statistical errors are accounted for in the XCES error.

3.2.2 Isolation

The isolation efficiency was determined in each bin by the same fit that was used for the 10 GeV trigger isolation efficiency. As can be seen in Fig. 3.4, the efficiency decreases as a function of photon energy in this energy region. This is most likely due to a mismatch between the online and offline isolation clustering. These results were also cross checked by comparing the neural net isolation values with the fraction of non-isolated 23 GeV trigger trigger events that passed the isolated 23 GeV trigger and corrected for the XCES requirement. The results of the comparison (Fig. 3.8) show that the two methods are consistent with each other.

3.3 50 GeV Non-isolated Photon Trigger

Data from the 50 GeV non-isolated trigger (PHOB_CEM5_50_NOISOL) was used above 55 GeV. It had a total integrated luminosity of 83.79 pb^{-1}. Because this trigger had no isolation or XCES requirements, the only efficiency that needs to be measured is the turn on efficiency. This was measured by taking the fraction of 23 GeV isolated photon events that also passed the 50 GeV non-isolated photon trigger. The results are shown in Fig. 3.9. The trigger is fully efficient in the region of interest.

3.4 6 GeV Isolated Photon Trigger

All of the 630 GeV data came from a 6 GeV isolated photon trigger. It had a total integrated luminosity of 0.538 pb^{-1}. Like the 10 GeV isolated photon trigger, we only had to measure the E_T threshold and isolation efficiencies. Because the basic trigger requirements are so similar to the 10 GeV trigger, it seemed reasonable to assume that the two triggers had the same efficiencies. Some simple checks of the trigger turn on and isolation efficiencies were done test this theory.

The trigger turn on efficiency was tested using a sample of events that passed a 5 GeV electron trigger (ELEB_CEM_5*). It was the only trigger with a lower P_T threshold than the photon trigger. Unfortunately, the statistics were not sufficient to accurately measure the turn on efficiency (Fig. 3.10), but they were good enough to show that the results were similar to the 10 GeV results. Therefore, we decided to use the 10 GeV trigger efficiencies. The 630 GeV photon cross section starts 3 GeV above the trigger threshold so the turn on efficiency was taken from the 13-14 GeV bin. The 10 GeV trigger was fully efficient 4 GeV above threshold so all the other 630 GeV bins were taken to be fully efficient.

The isolation efficiency measurement had the same problem of a lack of statistics. A sample of events that passed the 6 GeV non-isolated photon trigger was created and the fraction of those events that passed the neural net isolation cut was calculated. The data sample was not large enough to perform a bin by bin analysis as was done for the Run 1b data. Instead, all the events were put in one P_T bin. When the data was a combination of photons and mesons, 98% passed the neural net isolation cuts. When the data was photons only, 96% passed the isolation cut. These numbers are consistent with the Run 1b low P_T isolation efficiency of 0.98 ± 0.02. Therefore we matched up the 630 GeV P_T bins to the Run 1b P_T bins as best we could and took the the isolation efficiency from the 1b bin. If the 630 GeV bin included more than one of the Run 1b bins, the 6 GeV trigger isolation efficiency was taken to be the average of the isolation efficiencies for the two bins.

The full trigger efficiencies are listed in Table 3.2.

P_T bin (GeV/c)	P_T Turn On	Isolation	HAD/EM	XCES	Total
11-12	0.628±0.033	0.98±0.02	0.992±0.008		0.611±0.057
12-13	0.818±0.049	0.98±0.02	0.992±0.008		0.795±0.064
13-14	1.000±0.071	0.98±0.02	0.992±0.008		0.972±0.074
14-15	1.000±0.039	0.98±0.02	0.992±0.008		0.972±0.045
15-16	1.000±0.039	0.98±0.02	0.992±0.008		0.972±0.045
16-18	1.000±0.039	0.98±0.03	0.992±0.008		0.972±0.050
18-22	1.000±0.039	0.97±0.03	0.992±0.008		0.962±0.050
22-26	1.000±0.039	0.97±0.03	0.992±0.008		0.962±0.050
26-30	0.836±0.026	0.97±0.03	0.992±0.008	0.970±0.006	0.780±0.045
30-32	1.000±0.000	0.96±0.03	0.992±0.008	0.970±0.006	0.924±0.033
32-36	1.000±0.000	0.96±0.04	0.992±0.008	0.970±0.006	0.924±0.043
36-40	1.000±0.000	0.95±0.04	0.992±0.008	0.970±0.006	0.914±0.043
40-44	1.000±0.000	0.95±0.04	0.992±0.008	0.970±0.006	0.914±0.043
44-55	1.000±0.000	0.94±0.05	0.992±0.008	0.970±0.006	0.904±0.054
55-72	0.995±0.001		0.992±0.008		0.987±0.008
72-92	1.000±0.000		0.992±0.008		0.992±0.008
92-15	1.000±0.000		0.992±0.008		0.992±0.008

Table 3.1: The Run 1b trigger efficiencies as a function of photon P_T. The 10 GeV isolated trigger was used in the range 11 GeV $< P_T <$ 26 GeV. The 23 GeV isolated trigger was used in the range 26 GeV $< P_T <$ 55 GeV. The 50 GeV non-isolated trigger was used above 55 GeV.

P_T bin (GeV/c)	P_T Turn On	Isolation	HAD/EM	Total
9-11	1.000±0.071	0.98±0.02	0.992±0.008	0.972±0.074
11-13	1.000±0.039	0.98±0.02	0.992±0.008	0.972±0.045
13-16	1.000±0.039	0.98±0.02	0.992±0.008	0.972±0.045
16-19	1.000±0.039	0.98±0.03	0.992±0.008	0.972±0.050
19-23	1.000±0.039	0.97±0.03	0.992±0.008	0.962±0.050
23-29	1.000±0.039	0.97±0.03	0.992±0.008	0.962±0.050
29-40	1.000±0.039	0.96±0.04	0.992±0.008	0.952±0.058

Table 3.2: The 6 GeV isolated photon trigger efficiencies from the 630 GeV data as a function of photon P_T. The efficiencies were taken from the 1b data.

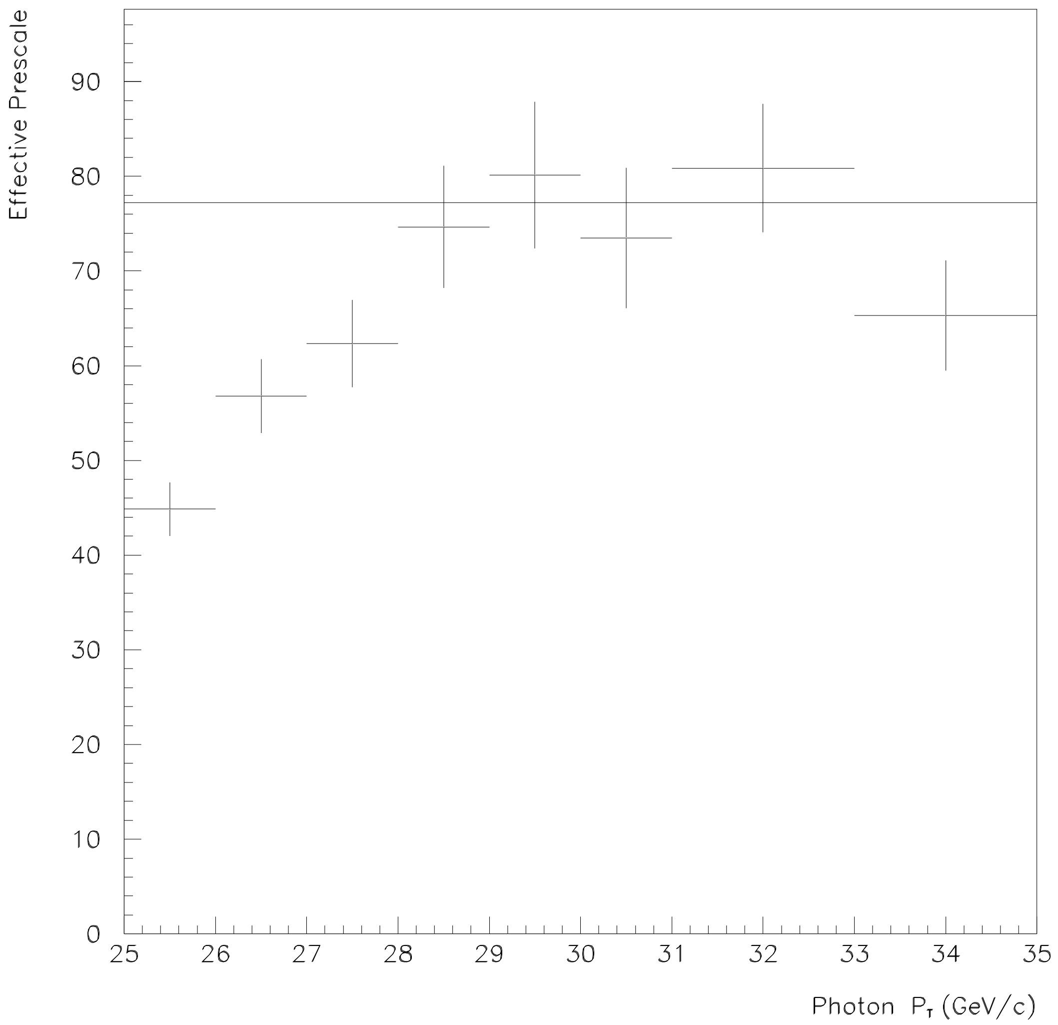

Figure 3.1: The effective prescale for the 10 GeV isolated trigger. The plot shows the number of events from the 23 GeV isolated trigger that pass all the cuts divided by the number of 10 GeV trigger events that also pass all the photon cuts. The prescale value quoted comes from the 4 bins between 29 and 33 GeV where the 23 GeV trigger is fully efficient and the statistics from both triggers are large.

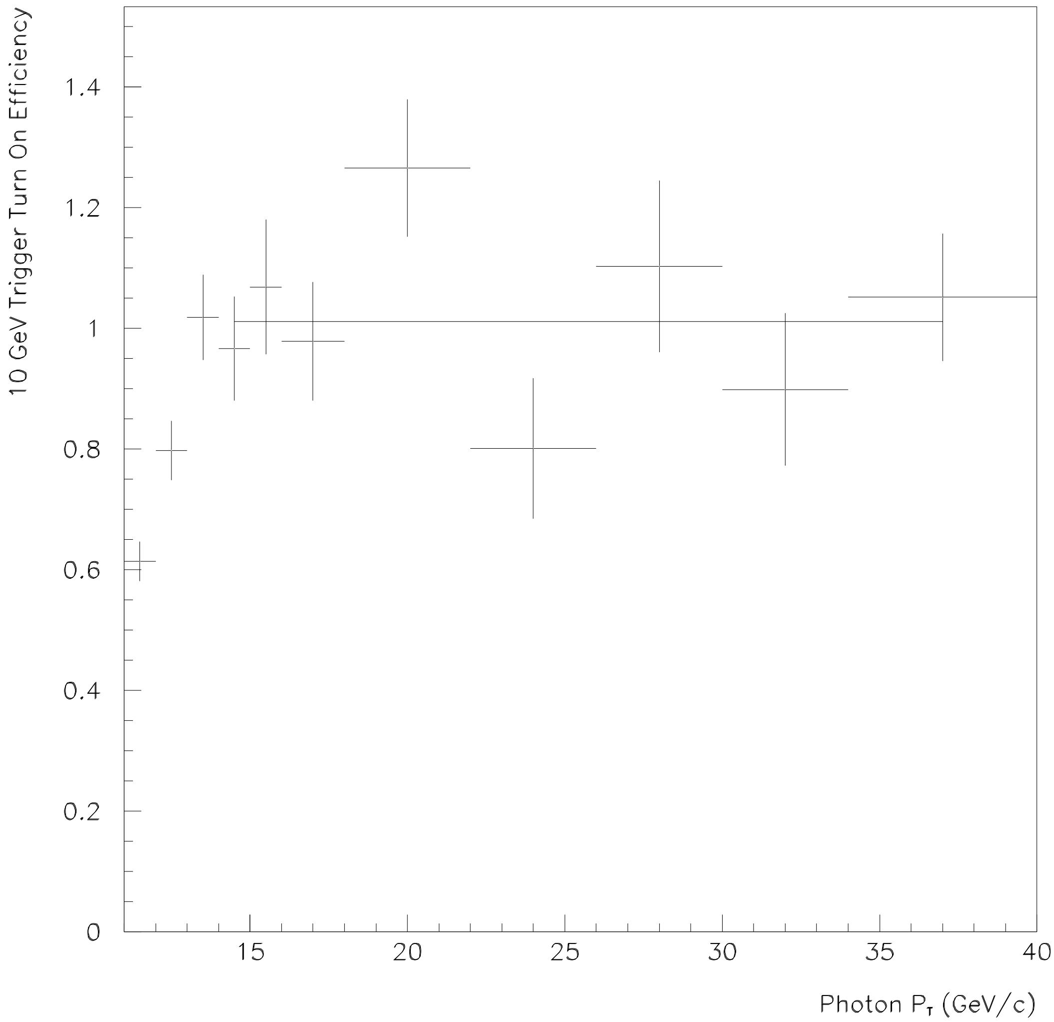

Figure 3.2: The number of 8 GeV trigger events that also pass the 10 GeV isolated photon trigger divided by the total number of 8 GeV electron events. That fraction was then multiplied by the photon prescale value of 77.8. The efficiency plateaus at 1.012 ± 0.039. The efficiency is therefore taken as 1.000 ± 0.039.

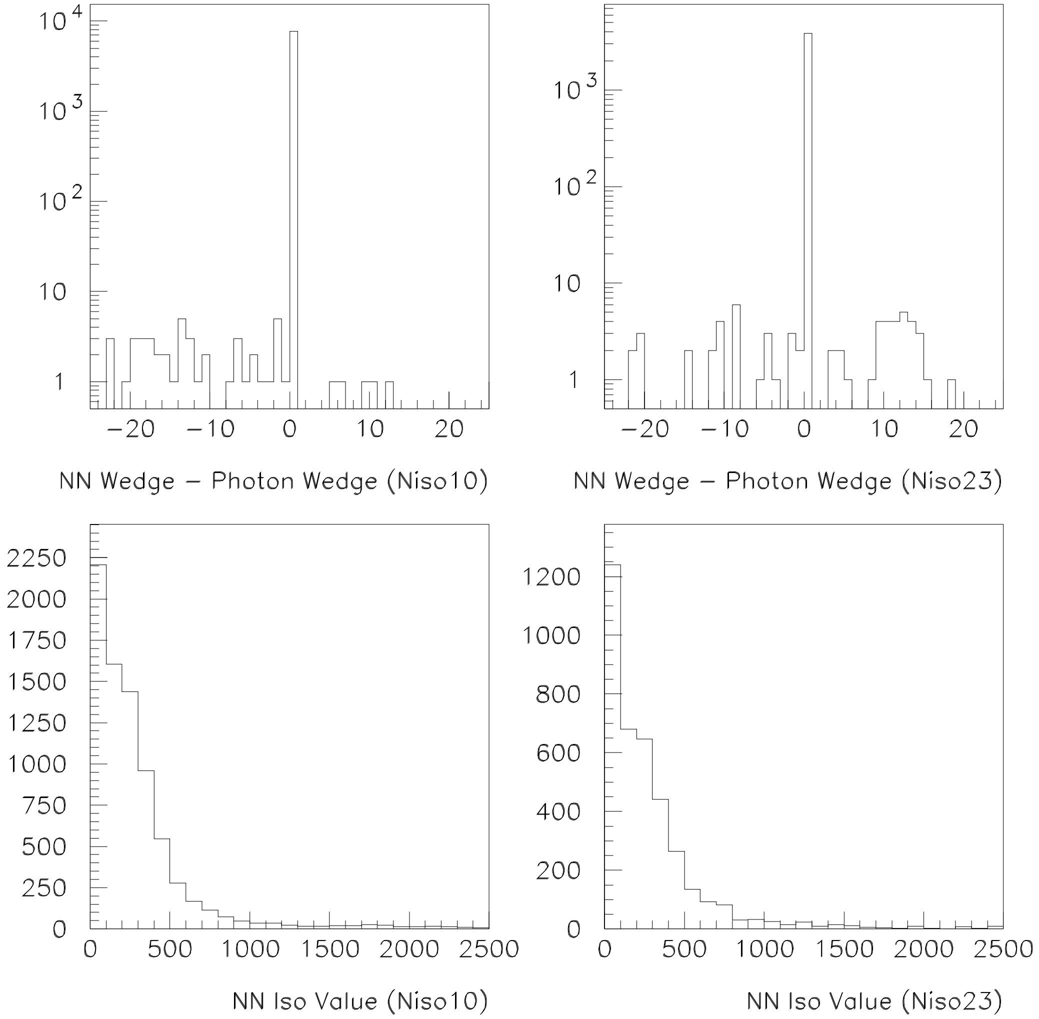

Figure 3.3: The top two plots show how often the neural net picked out the photons used for the analysis for the 10 GeV non-isolated (left) and the 23 GeV non-isolated (right) photon triggers. The bottom plots show the neural net isolation energy distributions for the same two triggers.

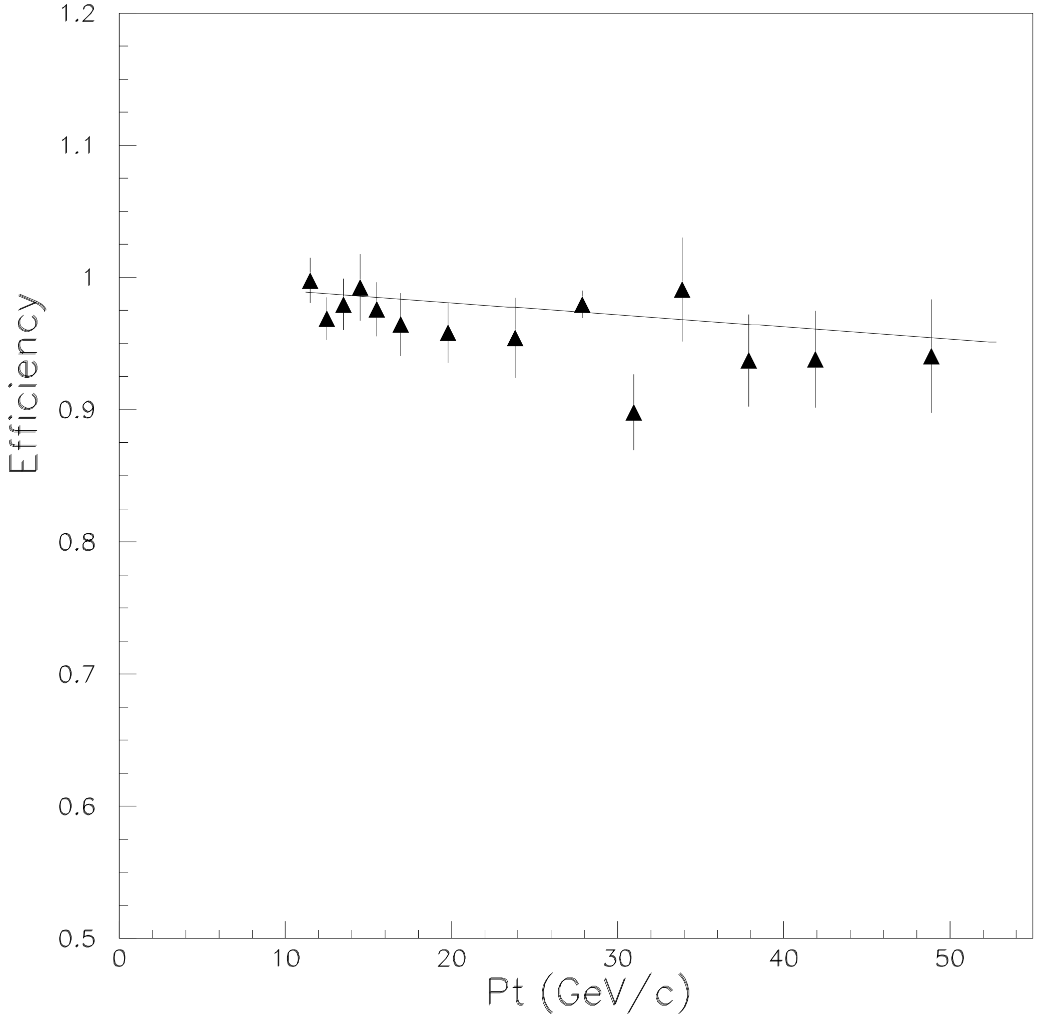

Figure 3.4: The fraction of photon events from the 10 GeV non-isolated and 23 GeV non-isolated photon triggers that had a neural net isolation value less than 1552. The points were fit with a line (0.996 - (0.0011 * P_T)), which was used to determine the isolation efficiencies for the bins used in the photon cross section.

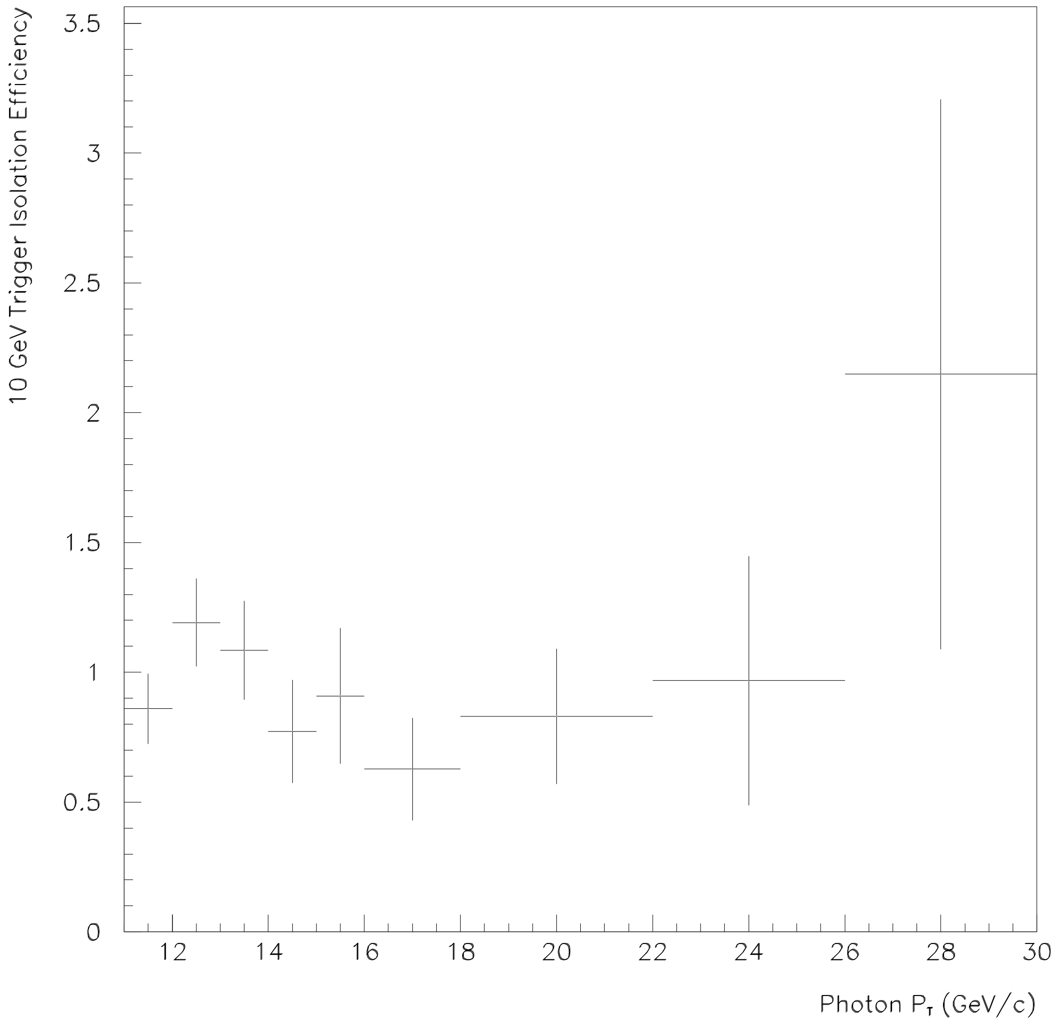

Figure 3.5: The number of 10 GeV non-isolated events that also pass the 10 GeV isolated trigger divided by the total number of 10 GeV non-isolated events. That fraction is multiplied by the photon prescale value of 77.8. The plot shows that the isolation efficiency is flat as a function of P_T in this P_T range.

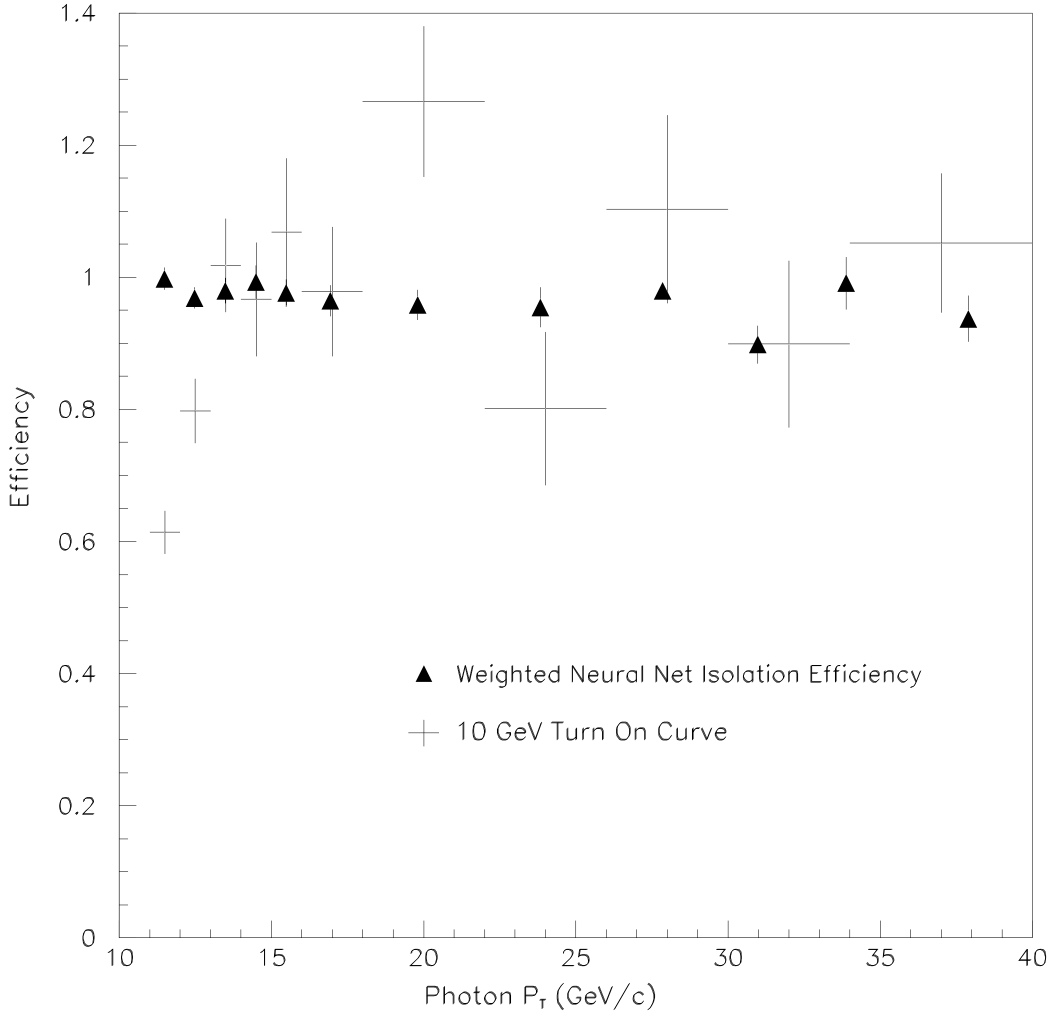

Figure 3.6: The neural net isolation efficiencies from Fig. 3.4 superimposed on the 10 GeV turn on curve as shown in Fig. 3.2. The two measurements are consistent with each other.

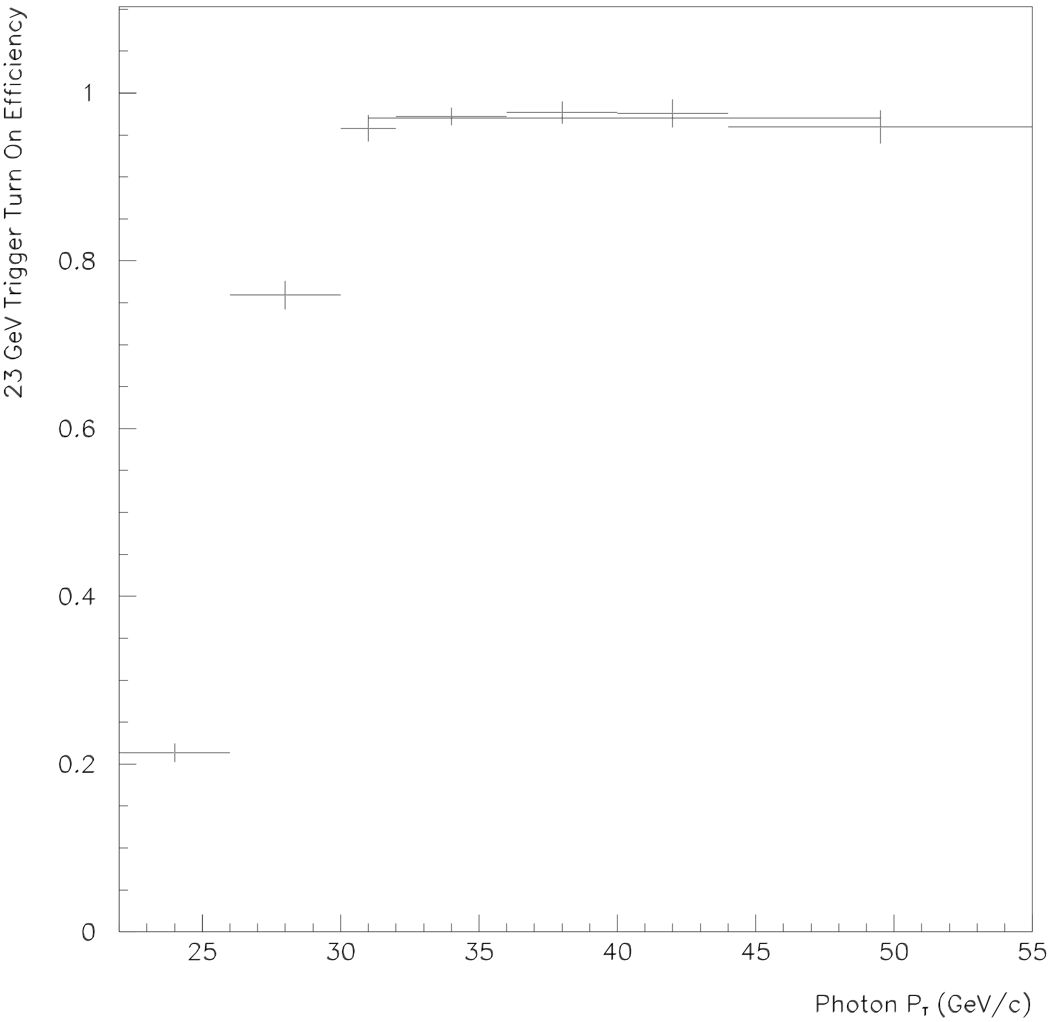

Figure 3.7: The number of 10 GeV isolated photon events that also pass the 23 GeV isolated photon trigger divided by all the events that pass the 10 GeV isolated photon trigger. The efficiency plateaus at 0.970 ± 0.006. The turn on efficiency between 30 GeV and 55 GeV is therefore taken as 1.000 ± 0.000 and the XCES efficiency is taken as 0.970 ± 0.006.

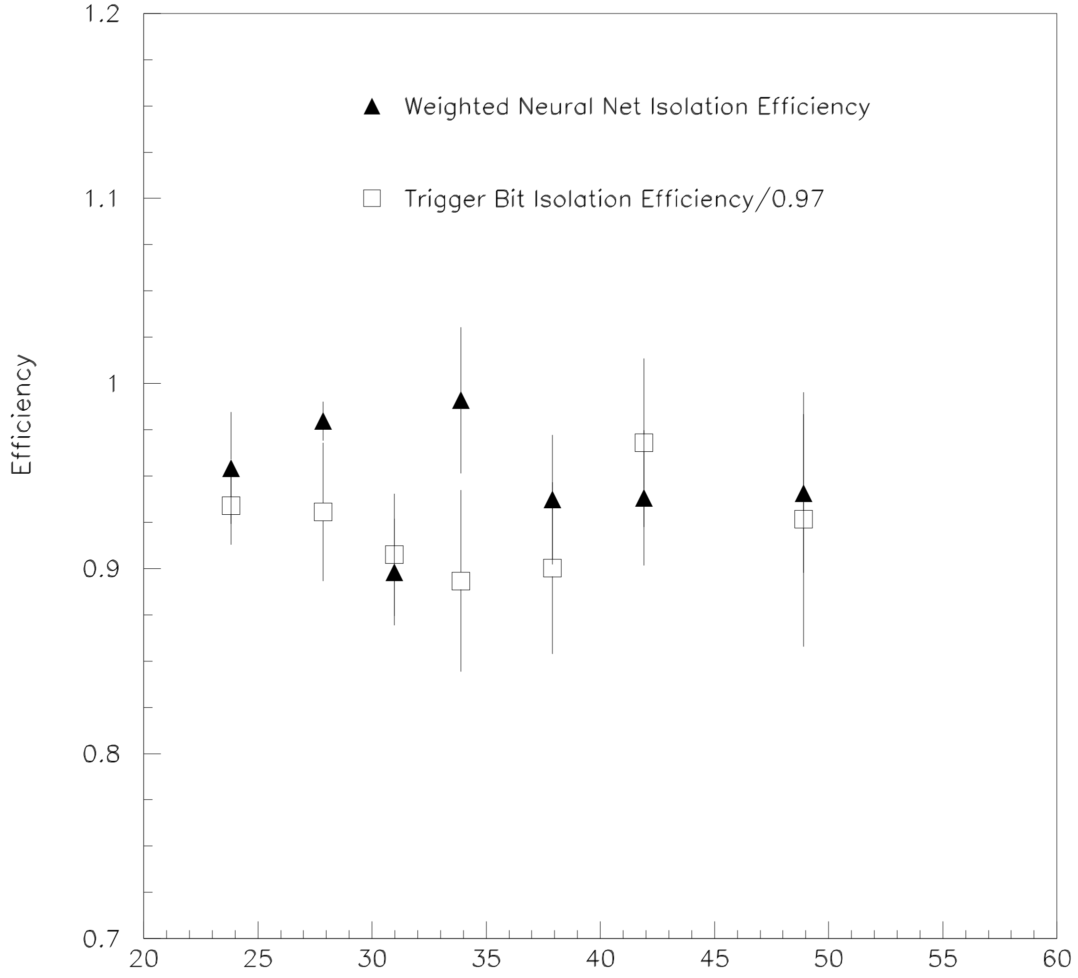

Figure 3.8: The number of events that pass the 23 GeV non-isolated trigger and the 23 GeV isolated trigger divided by all the events that pass the non-isolated trigger. That fraction is then divided by 0.97 to account for the events that are lost due to the XCES requirement in the Level 2 isolated trigger. The result is superimposed on the neural net isolation efficiencies as shown Fig 3.4. The two methods of measuring the isolation efficiency are consistent with each other.

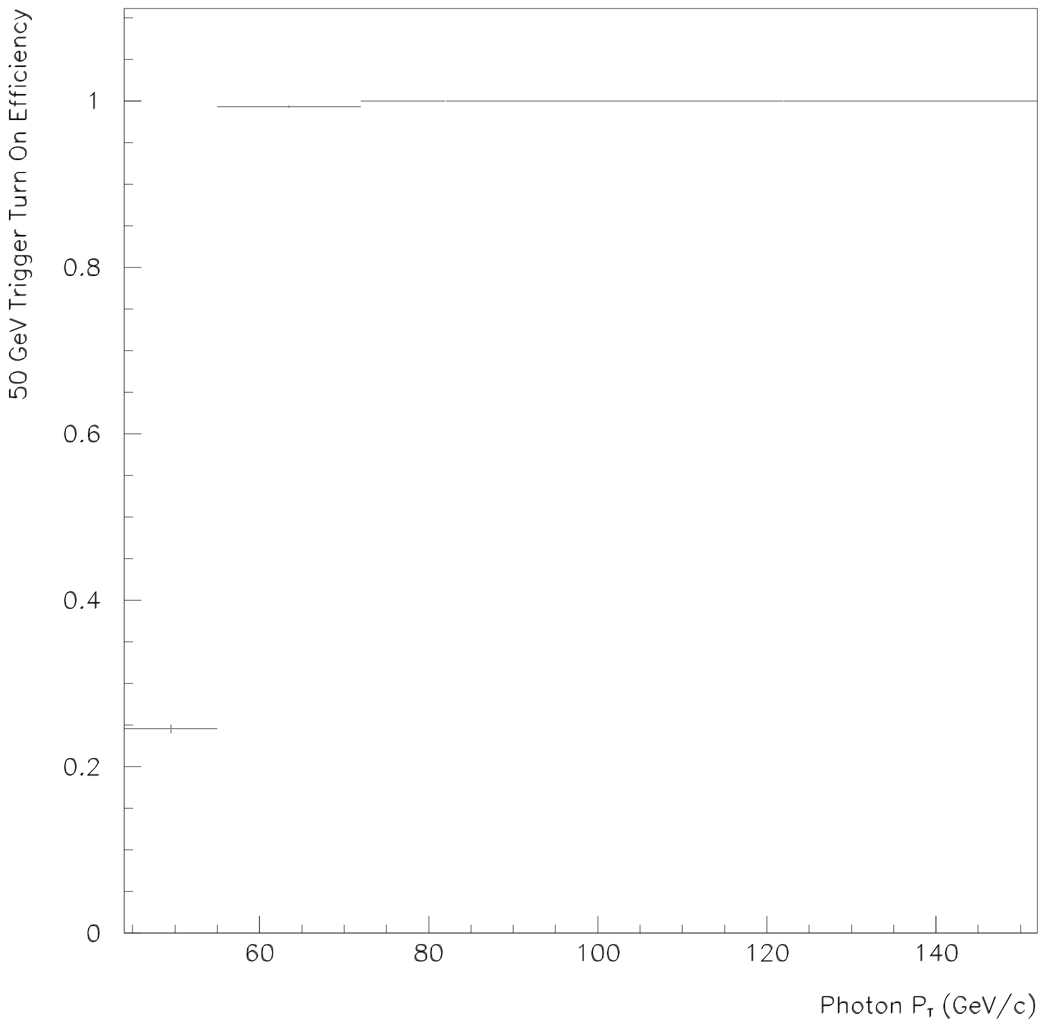

Figure 3.9: The number of 23 GeV isolated photon events that also pass the 50 GeV non-isolated photon trigger divided by all the events that pass the 23 GeV isolated trigger. The trigger is fully efficient with 0.000 statistical error above 72 GeV.

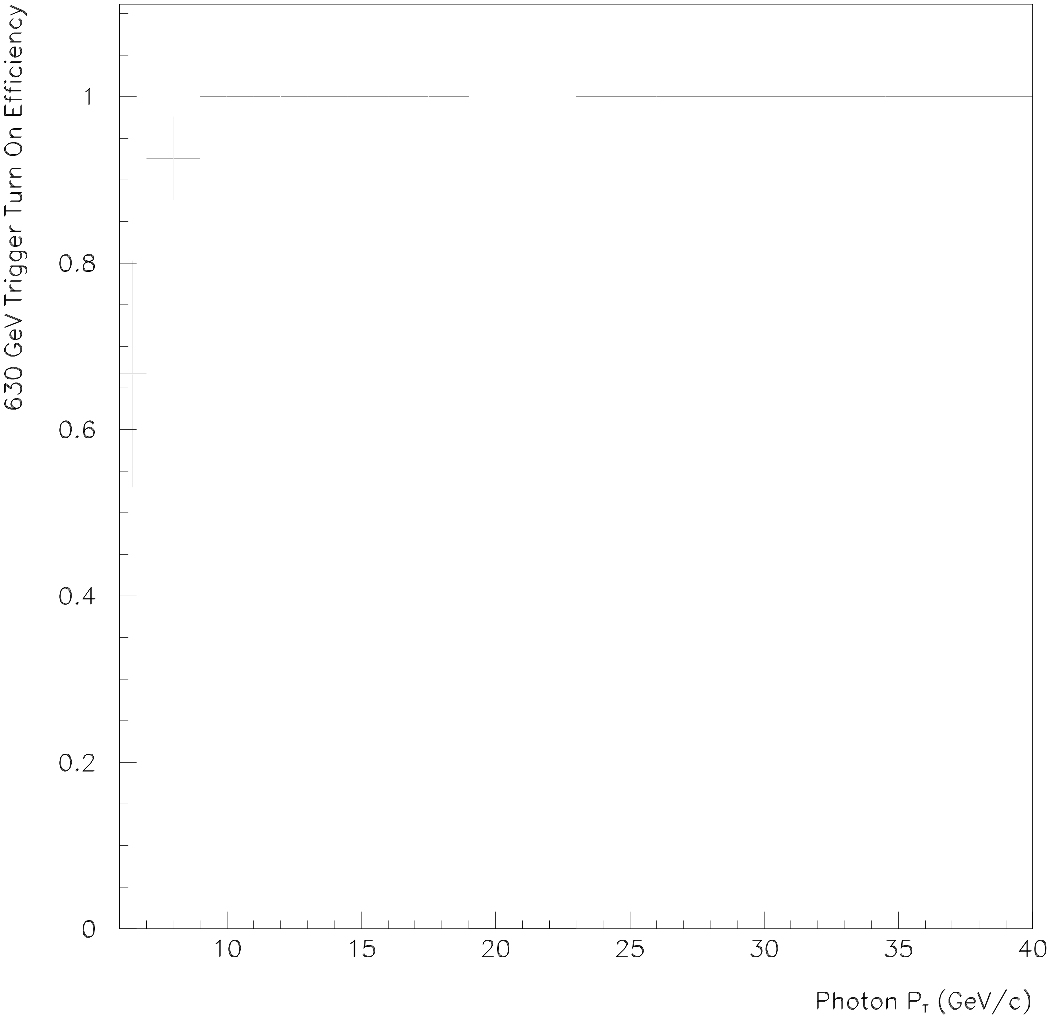

Figure 3.10: The fraction of 5 GeV electron trigger events that also pass the 6 GeV isolated photon trigger. There are not enough events to accurately measure the efficiency.

Chapter 4

Event Selection

There are many particles, such as electrons, that produce a signal similar enough the that of a photon that they are able to pass the photon triggers. Therefore, once we had our data sample, we had to impose further restrictions to reduce the number of background events that make it into our cross section measurement. The main backgrounds to prompt photons are real photons from jets, meson decays, and cosmic ray muons. The most basic type of restriction is a fiducial cut. The photon candidates must be located in the center of the detector where both the CES and CPR are active so that all of the photon's properties we are interested in can be measured.

The rest of the restrictions were designed to remove the background from specific sources. The isolation requirement imposed by the trigger is further tightened to reduce the number of photons coming from jets. Electrons and other charged particles can be eliminated by restricting the data to candidates that are not associated with a track. Photons, unlike electrons, are electrically neutral so they should not leave a track in the Central Tracking Chamber. Therefore, any particle that produces a track cannot be a photon.

There are two ways that photons from meson decays can differ from prompt photons. Depending on the spatial separation of the photons, the showers from multiple photons can either overlap so that the shower profile is inconsistent with the shower profile of a single photon or they can be separated enough to produce a second cluster in the CES. Therefore, cuts on the shower shape and CES clusters reduce the number of photons from meson decays.

Occasionally cosmic ray muons will radiate a photon in the calorimeter. These muons do not have to originate in the center of the detector, so they may not leave a track in the CTC. They have to be eliminated with something other than a cut on particles with tracks. Cosmic ray radiation is, therefore, eliminated with a cut on the variable known as missing E_T. As mentioned previously, the total energy in the event is not conserved because some of the energy is lost down the beampipe, but the energy in the transverse direction is conserved. Cosmic rays add E_T to the event which cannot be balanced by the rest of the event. Missing E_T, therefore, is a measure of the transverse energy imbalance, and a cut on the amount of missing E_T can reduce the amount cosmic ray contamination in the photon cross section.

Unfortunately, as was the case for the trigger, there is always the possibility that real prompt photons can fail these requirements, and the fraction of events that fail must be measured.

4.1 Fiducial Cut

The fiducial cut was imposed to avoid uninstrumented regions at the edges of the CES. It requires the position of the shower with the highest E_T to be within 17.5 cm of the chamber center in the azimuthal direction (perpendicular to the wires) and to have 14 cm $< |Z| <$ 217 cm (i.e. to be within the active region of the strip chamber). The region remaining after this cut is 64% of the solid angle for $|\eta| < 0.9$. In addition, the region $0.77 < \eta < 1.0, 75^\circ < \phi < 90^\circ$ is uninstrumented because it is the area of penetration for the cryogenic magnets connections to the solenoidal magnet.

In order to avoid events with complex projective geometry, events with a Z_{vertex} more than 60 cm away from the nominal vertex position were rejected. The efficiency of the Z_{vertex} efficiency 93.7% for the Run 1B data [15] and 85±5% for the 630 GeV data [16].

4.2 The Isolation Cut

As mentioned in Chapter 1, at collider energies experiments detect *isolated* photons in order to avoid photons from fragmentation processes at high energies and small x_T. The isolation cut requires that the extra transverse energy inside a cone of radius $R = \sqrt{\Delta\eta^2 + \Delta\phi^2}$ centered on the photon has to be lower than some threshold. The isolation cut was applied at the hardware level, selecting only events with extra energy below 4 GeV in a cone of radius 0.4. Then, the isolation cut of both the Run 1b and 630 GeV data sets were tightened to 1 GeV in a cone of radius 0.4, which improved the signal to background ratio.

To estimate the isolation cut efficiency, the following approximation was used. We measured the transverse energy sum E_T within randomly placed cones of radius 0.4 in minimum bias events and assumed that it represents the approximate underlying sum E_T in direct photon events.

The distribution of extra energy in the cone does not depend on the photon P_T, but it does depend strongly on the number of interactions in the underlying event. Figure 4.1 shows how steeply the isolation efficiency decreases with the number of vertices. In previous measurements, the number of interactions was predicted by the instantaneous luminosity [17]. The actual number of vertices in each event was not studied. To determine how well the luminosity predicted the number of vertices, we plotted the isolation efficiency versus the number of vertices for three luminosity ranges (Fig. 4.2). The efficiency for the three ranges are consistent with each other showing that the number of vertices is the more important variable. High luminosity increases the likelihood of an event having a large number of vertices, but the majority of the events still have only a few vertices.

We then compared the vertex distribution from the photon data to that of the minimum bias data. As can be seen from Fig. 4.3, the minimum bias data sample has significantly more events with no vertices than the photon sample has. Therefore, we had to use a weighted average to get the correct isolation efficiency for the photon sample. First we calculated the average number of vertices from the photon data (1.6) and found that point on the minimum bias efficiency plot. As a cross check we multiplied the total number of photon events in each vertex bin by the minimum bias isolation efficiency for that bin. The products were then summed and divided by the total number of photon events. The two methods gave the same results. The isolation efficiency is 0.832 [18].

Because each minimum bias event was used multiple times to calculate the efficiency, the error bars do not provide an accurate picture of the size of the fluctuations. To measure the fluctuation, we divided the full data set into 3 time ordered groups and plotted the isolation efficiency for each group (Fig. 4.4). We then recalculated the isolation efficiency twice. The first time we used the highest points in each bin, and the second time we used the lowest point in each bin. The difference between the average efficiency and the high/low efficiency was taken as the statistical error, 0.004.

The same methods were used to calculate the isolation efficiency for the 630 GeV photon sample. The isolation efficiency from the minimum bias data is shown in Fig. 4.5. The vertex distribution from the two data samples is shown in Fig. 4.6. As can be seen in that figure, a larger fraction of the events are in the first bin than in the 1b data. The average number of vertices is 0.9 and the isolation efficiency, therefore is 0.919 ± 0.013.

One problem with the isolation cut is that at higher energies the size of the photon clusters increases to the point where some of the energy can fall outside the isolation cone. The cluster energy should be corrected for this lateral shower leakage before the isolation cut is applied [19]. In the Run 1b analysis, however, many of the cross section efficiencies were measured using the uncorrected cone energy less than 1 GeV. In order to be consistent, the overall cross section is calculated using the uncorrected cone energy and then corrected for the shower leakage. Figure 4.7 shows the ratio of the cross sections with and without the shower leakage corrections. The leakage corrections are expected to increase roughly linearly with increasing shower energy. As can be seen in the plot, the correction to the second to last point seems too large. Therefore, the ratio of cross sections was fit with a line and the fitted value was taken as the leakage correction. The fractional difference between the real and fitted values was taken as the error on the correction and that number was added in quadrature with the cross section's statistical errors.

Because the 630 GeV data involved lower energy photons, the shower leakage corrections were not applied. On average it affected the cross section by less than 0.3%.

4.3 The No Track Cut

The no track cut requires that there be no track pointing at the CPR chamber or the tower where the photon candidate is located. Direct photons can fail the no track cut in two ways. First, they may convert in the material in front of the CPR. Using a calibration by the CDF W mass group, this material amounts to $7.51\% X_0$ with a 7% uncertainty leading to a 5.7% correction to the cross section with a 0.4%

uncertainty.

The second way direct photons can fail the no track cut is when they combine with a track from the underlying event. Using minimum bias data we measured the efficiency of this cut (we used the same assumptions as in the isolation cut case) to be 0.845 ± 0.003 for the Run 1B data [18] and 0.905 ± 0.006 for the 630 GeV data (Figs. 4.8 and 4.9).

4.4 The Extra Strip/Wire Cut

The single and multiple meson backgrounds are all reduced by requiring that there be no other photon candidates above 1 GeV in the CES. The efficiency of this cut depends on the energy of the photon candidate. The efficiency of the cut for electrons measured in the 1985 test beam and for electrons from W boson decay (both simulated and measured). The efficiency of electrons from W decay is lower than the extrapolation from the test beam electrons due to the radiation of an extra photon in this physics process. The efficiency of the extra strip/wire cut changes from 97% to 87% as the photon P_T increases from 10 GeV/c to 40 GeV/c [20]. This efficiency is the same for both the Run 1B and 630 GeV data.

4.5 $\chi^2 < 20$ Cut

Events were also eliminated if the single shower fit to the standard test beam electron profile had a χ^2 larger than 20. The details of this fit, which is the main tool of the *profile method*, are described in Chapter 5. The $\chi^2 < 20$ cut provides significant rejection against multiple photon backgrounds (particularly photons from η decay) and is almost 100% efficient for direct photons in both our data samples [21].

4.6 The Missing E_T Cut

Cosmic ray muons can radiate a photon in the CEM and fake a photon signal. The characteristic signature for this process is that there is no jet on the other side of the event. The cosmic ray background was eliminated by cutting on the amount of missing E_T divided the cluster E_T (or photon E_T) [22]. Figure 4.10 shows this variable for photons above 55 GeV where there is a clean separation with a cut at 0.8. The separation gets steadily worse for lower P_T photons, since the jet fluctuations increase. It can clearly be seen in Fig. 4.12 there is a tail of real photon events being lost above 0.8 for photons in the 18-26 GeV range. Below 18 GeV there is no longer clear separation between signal and background (Fig. 4.11), but the fraction of of cosmic ray events is getting very small, since the spectrum for cosmic rays is not as steep as that of direct photons (Fig. 4.13).

The efficiency was then measured for events in the range 18 GeV $< E_T <$55 GeV by plotting the missing E_T divided by the cluster E_T in a few photon E_T bins and fitting the slope of the curve around the 0.8 cut. The number of photons lost was determined by the area under the extrapolated line and then the fraction of total photons lost was calculated. This was done for 4 different E_T bins which were then fit with a quadratic polynomial to determine the efficiency for the remaining bins. Below 18 GeV the cut was not applied as too many real photons would be lost. In this range the fraction of cosmic ray events contaminating the sample was measured by fitting the slope in the high E_T region in Fig. 4.11 and extrapolating the line back to the lower energy region. We estimated that there is a 2.4% contamination of cosmic rays in the bins from 10-18 GeV, for which we correct the photon cross section downward. We take as a systematic uncertainty 1/2 of the corrections mentioned above, which ranges from 0 at high P_T to 1.2% at 10-18 GeV.

4.7 Total Acceptance

Finally the total acceptance of the Run 1b prompt photons, including efficiencies for all applied cuts is approximately 34% with a small P_T dependence (Table 4.1). This is slightly lower than the acceptance of prompt photons in the Run 1a measurement due to the effect of multiple collisions at the higher luminosities. The total acceptance for the 630 GeV data is 37.2% (Table 4.2).

Cut	Efficiency	Uncertainty
Fiducial	0.64	
Dead CES/CEM	0.977	
$\|Z_{vertex}\| < 60$ cm	0.937	0.011
Isolation	0.832	0.004
No track (conversions)	0.943	0.004
No track (min bias)	0.845	0.003
Extra CES cluster	0.893	0.031
Missing E_T	0.976	0.014
Total	0.339	0.036

Table 4.1: A list of the photon selection efficiencies and their uncertainties for the Run 1B data.

Cut	Efficiency	Uncertainty
Fiducial	0.64	
Dead CES/CEM	0.977	
$\|Z_{vertex}\| < 60$ cm	0.85	0.05
Isolation	0.919	0.013
No track (conversions)	0.943	0.004
No track (min bias)	0.905	0.006
Extra CES cluster	0.893	0.031
Missing E_T	0.976	0.014
Total	0.372	0.062

Table 4.2: A list of the photon selection efficiencies and their uncertainties for the 630 GeV data.

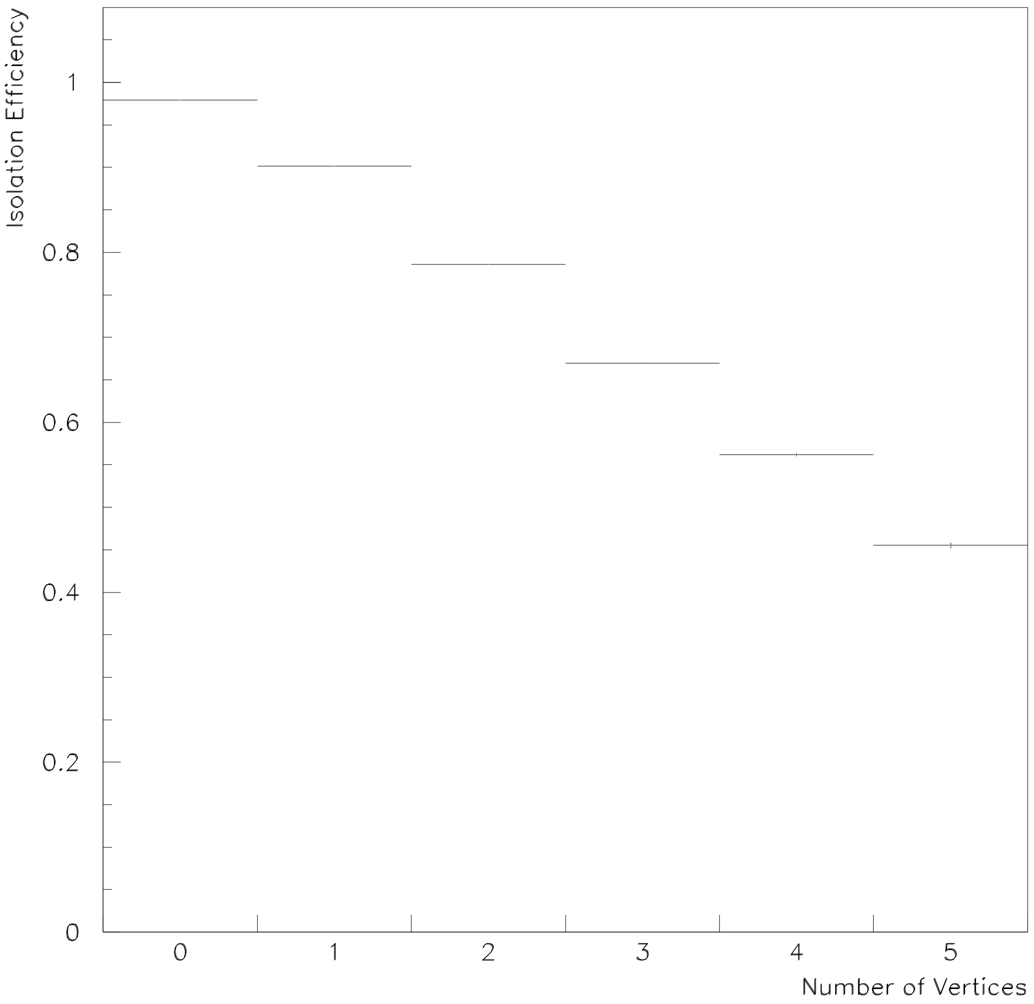

Figure 4.1: The isolation efficiency (fraction of minimum bias events, with and without tracks, that have an energy in a cone of radius 0.4 < 1 GeV out of all events) as a function of the number of vertices in the event.

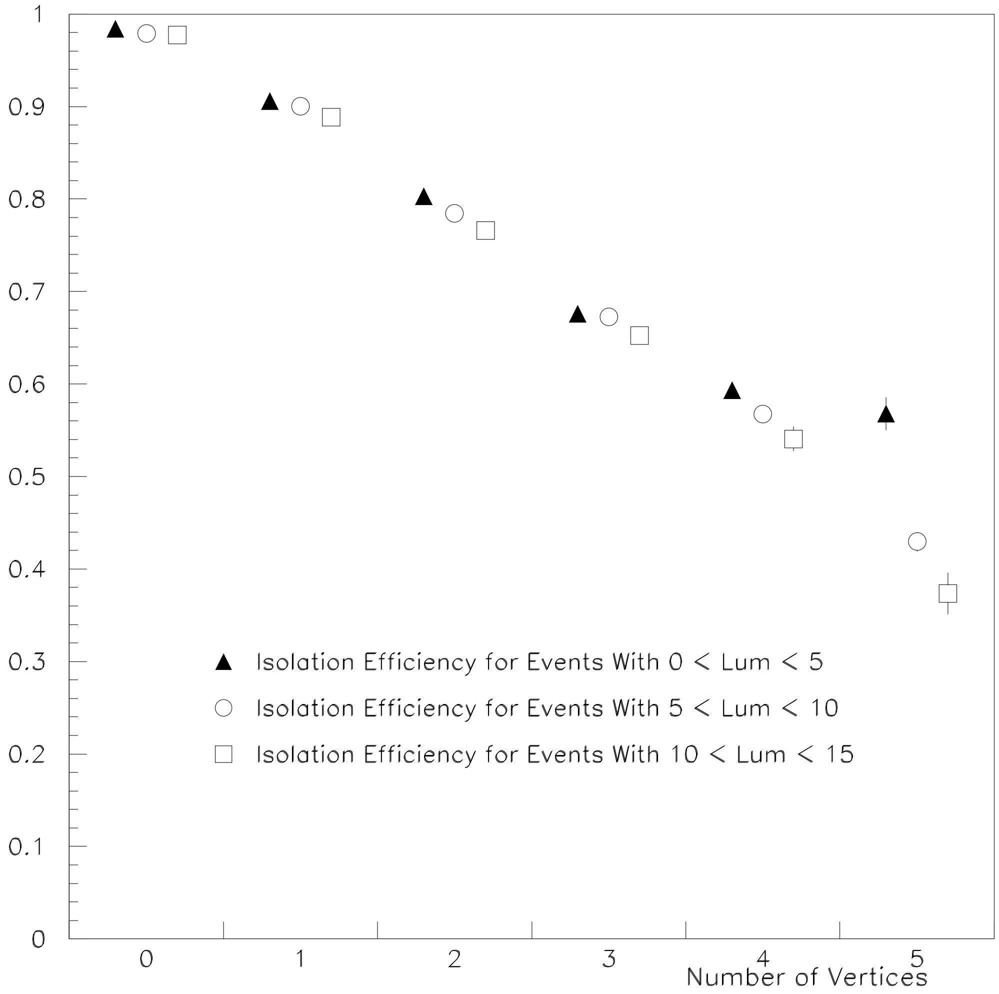

Figure 4.2: The isolation efficiency (fraction of minimum bias events, with and without tracks, that have an energy in a cone of radius 0.4 < 1 GeV out of all events) as a function of the number of vertices in the event for different luminosity ranges. The isolation efficiency depends more on the number of vertices in the event than the luminosity.

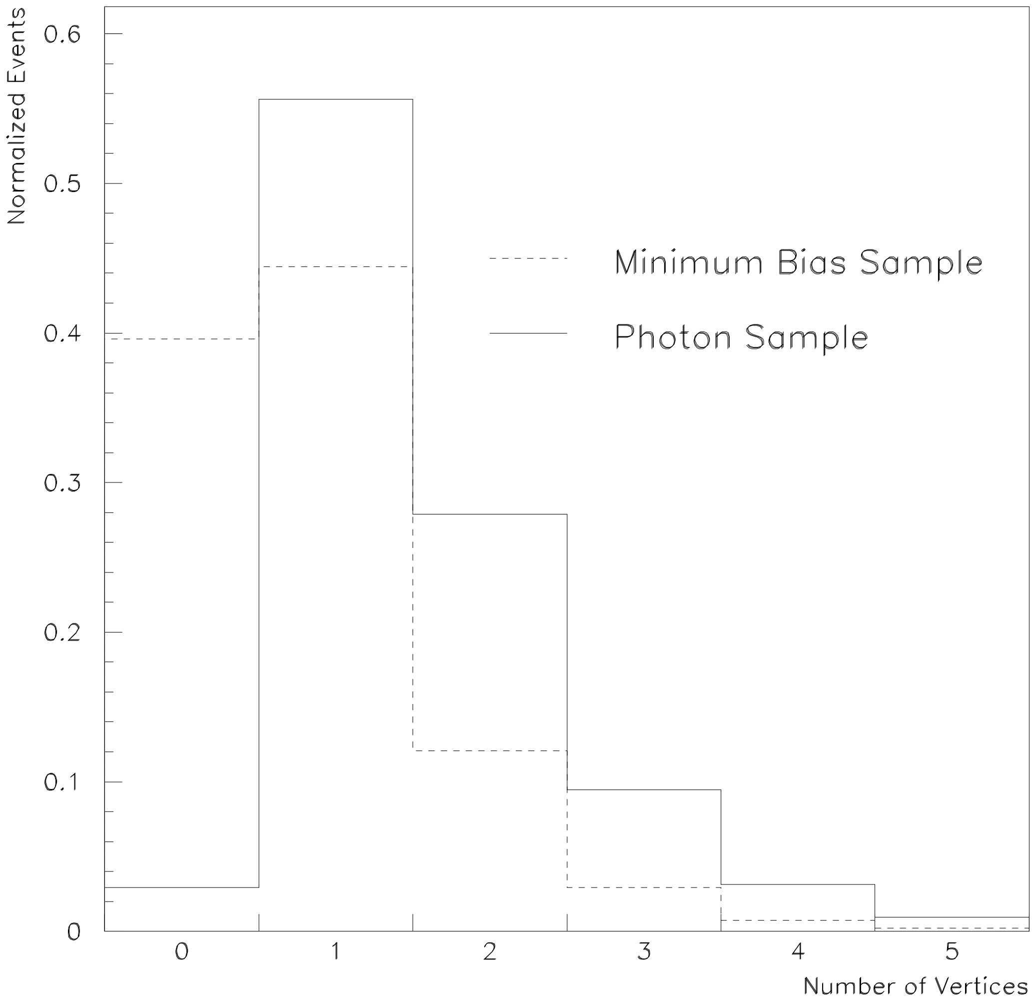

Figure 4.3: Vertex distribution for events that passed the 23 GeV isolated photon trigger and events that passed the minimum bias trigger. The distributions have been normalized to 1.

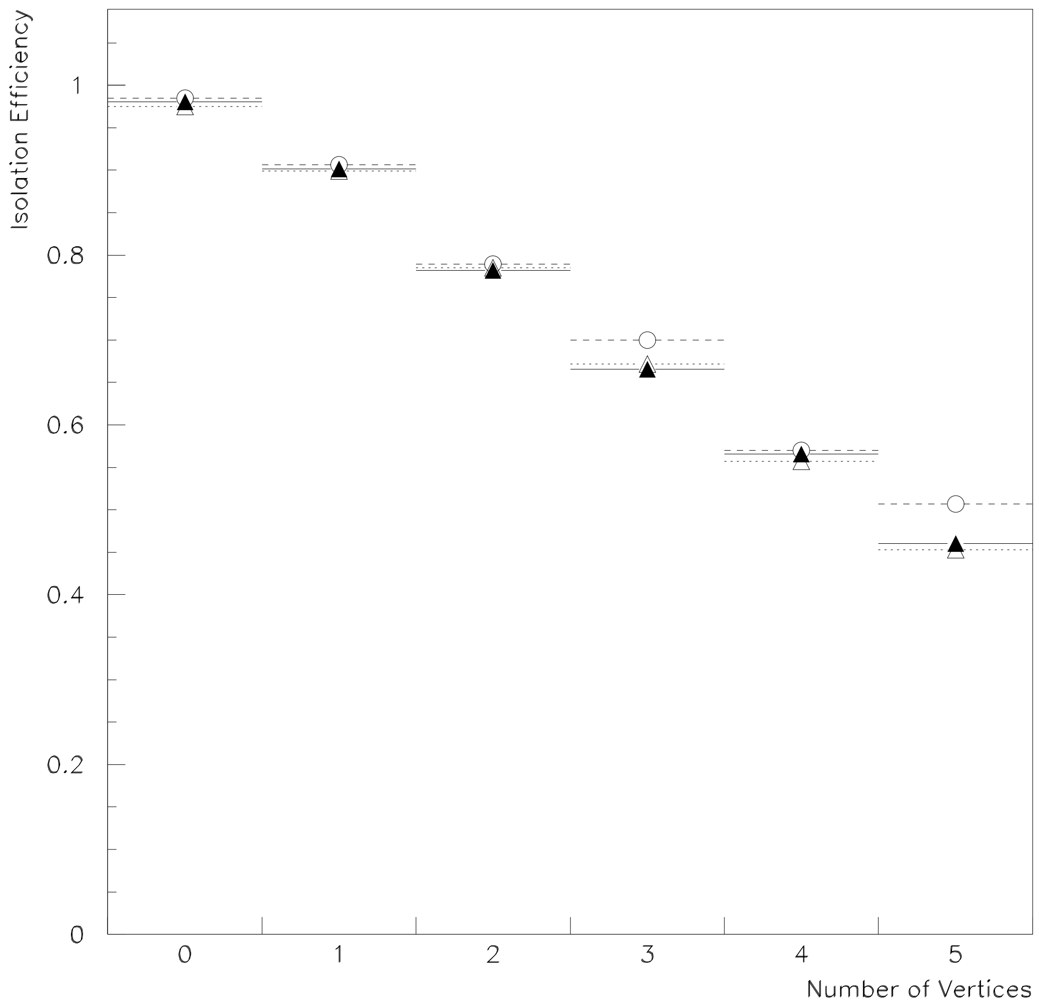

Figure 4.4: The isolation efficiency (fraction of minimum bias events, with and without tracks, that have an energy in a cone of radius 0.4 < 1 GeV out of all events) as a function of the number of vertices in the event after the full data sample had been divided into 3 smaller groups. The systematic error on the efficiency was found to be 0.004 by taking the highest and lowest values and recalculating the efficiency.

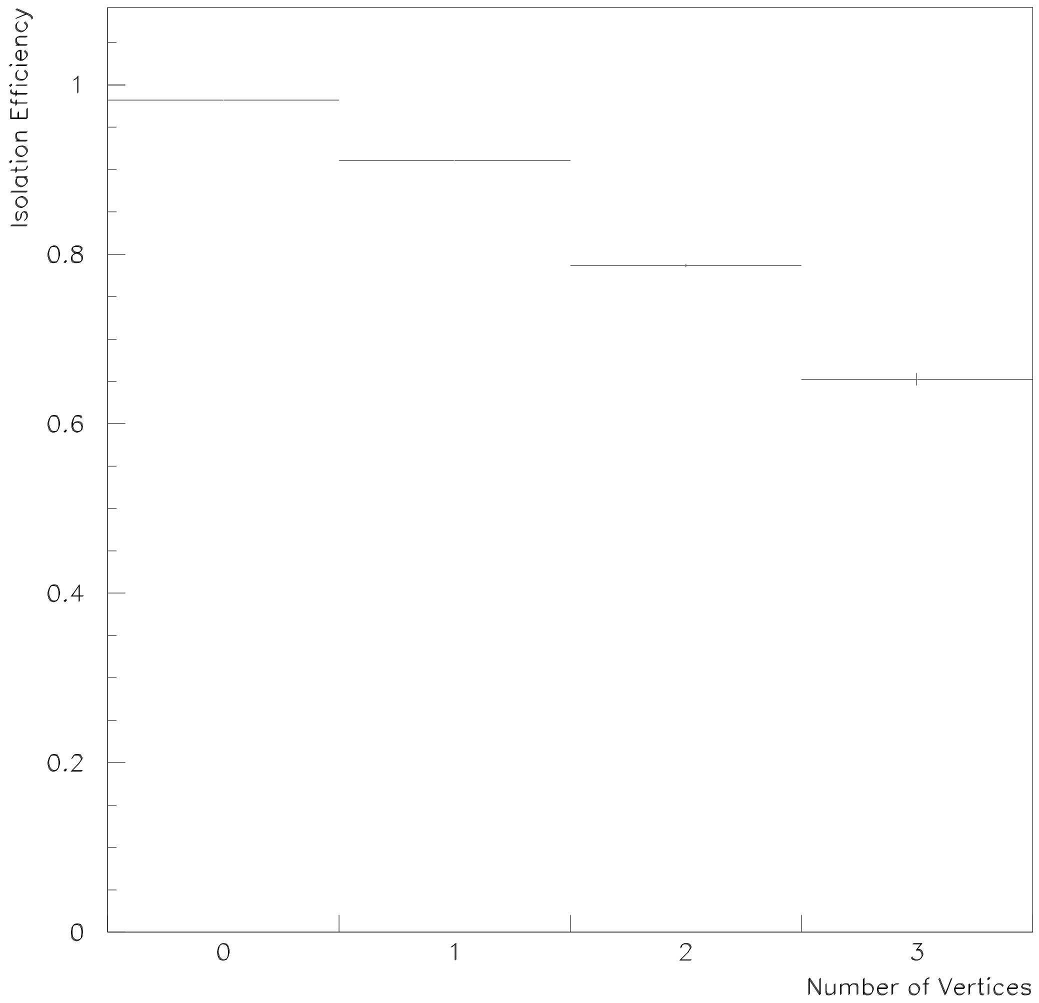

Figure 4.5: The isolation efficiency (fraction of minimum bias events, with and without tracks, that have an energy in a cone of radius 0.4 < 1 GeV out of all events) as a function of the number of vertices in the event for the 630 GeV data.

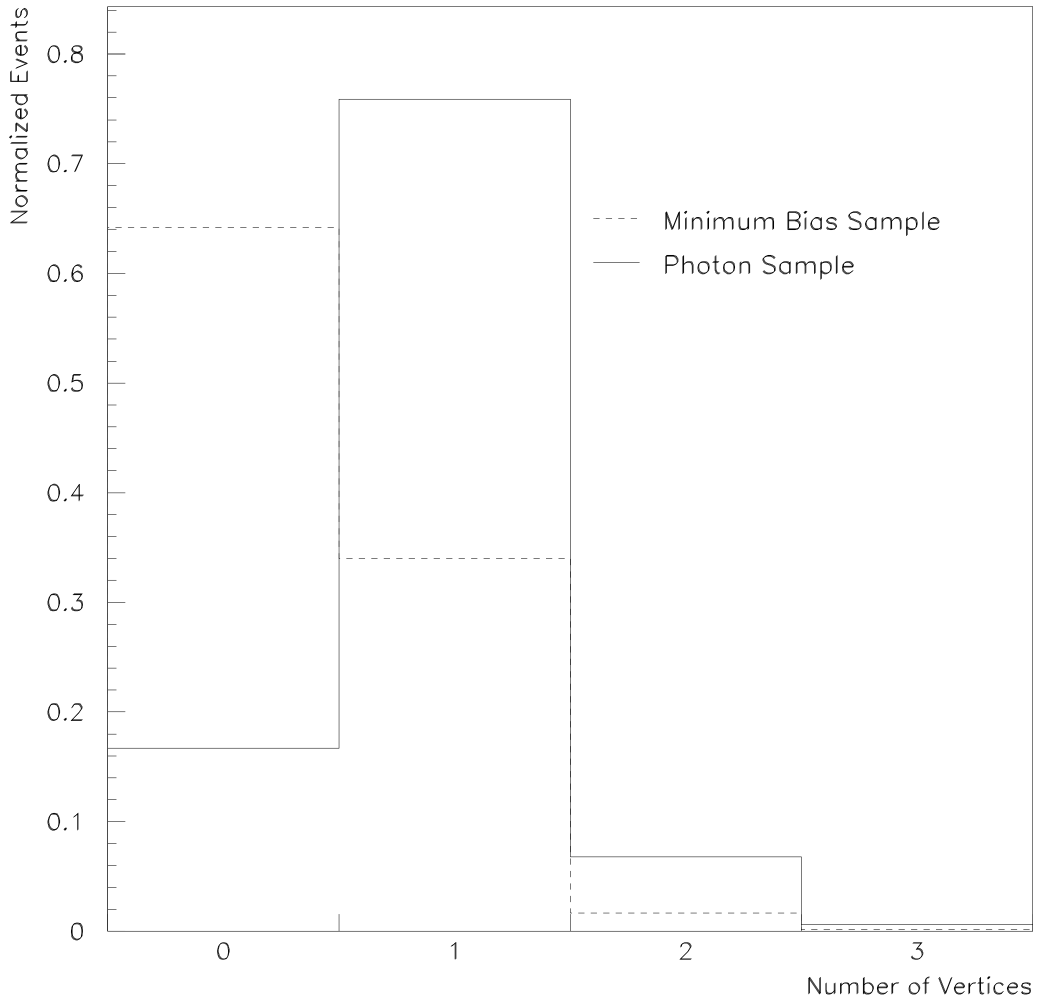

Figure 4.6: Vertex distribution for events that passed the 6 GeV isolated photon trigger and events that passed the 630 GeV minimum bias trigger. The distributions have been normalized to 1.

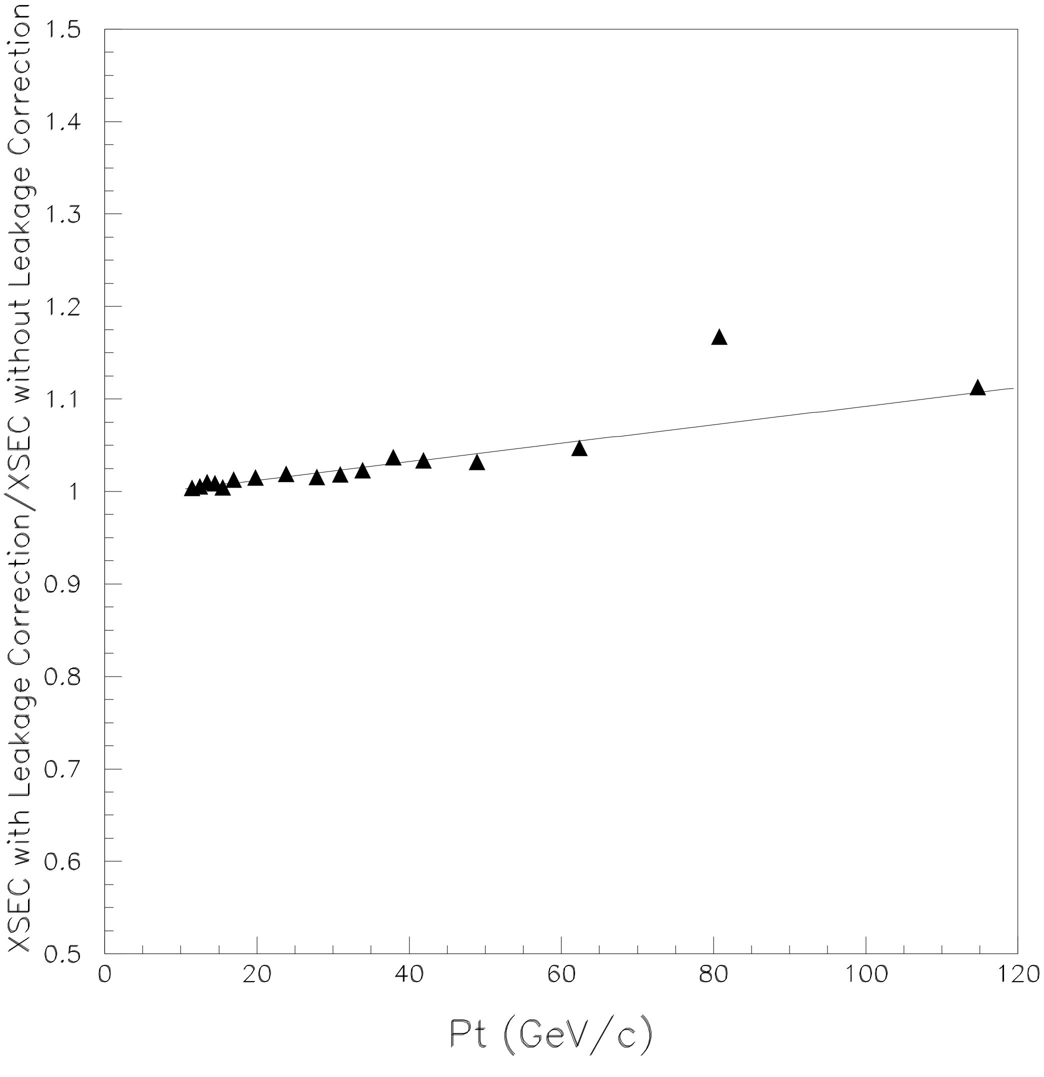

Figure 4.7: The ratio of the photon cross sections with and without the lateral shower leakage corrections fit with a line.

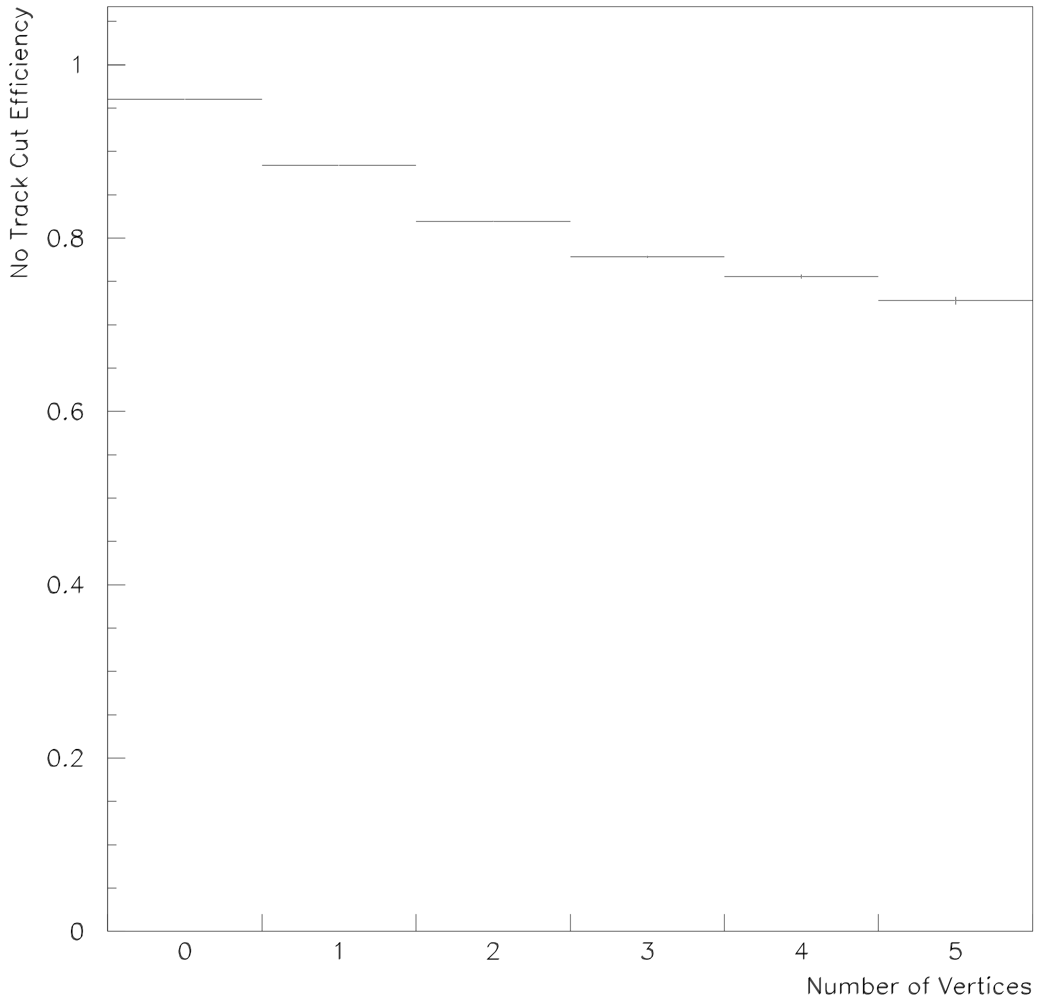

Figure 4.8: The no track cut efficiency (fraction of minimum bias events that have no track pointing at wedge being tested out of all events) as a function of the number of vertices in the event.

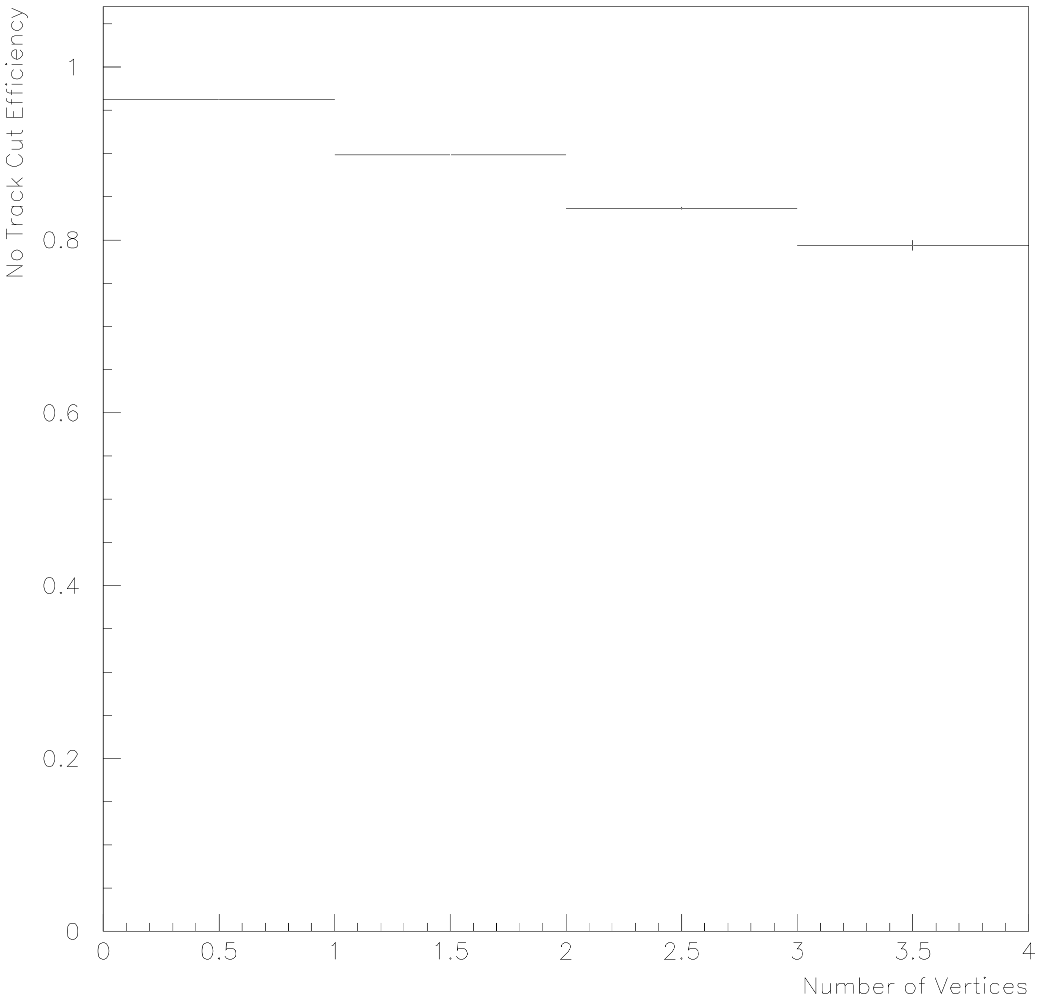

Figure 4.9: The no track cut efficiency (fraction of minimum bias events that have no tracks out of all events) as a function of the number of vertices in the event for the 630 GeV data.

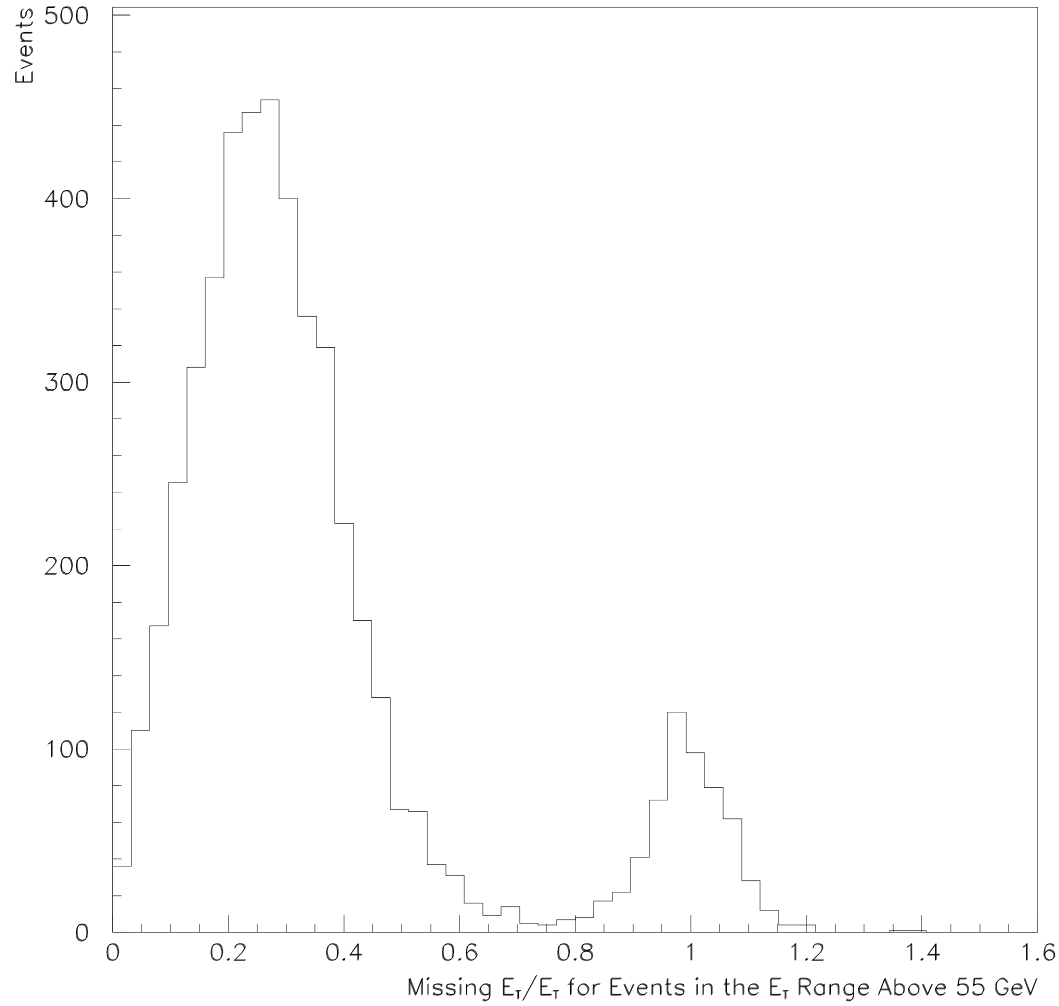

Figure 4.10: The missing E_T divided by photon E_T for photons above 55 GeV.

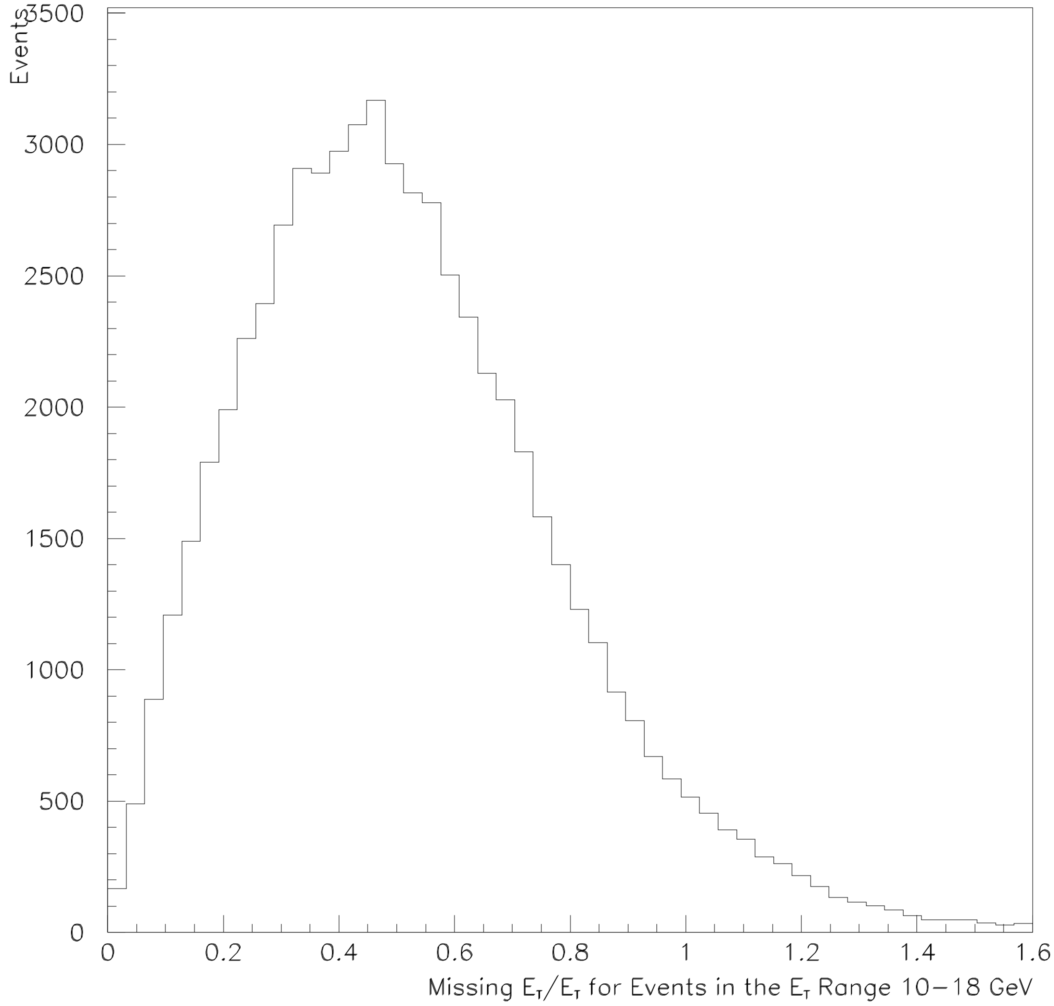

Figure 4.11: The missing E_T divided by photon E_T for photons between 10-18 GeV.

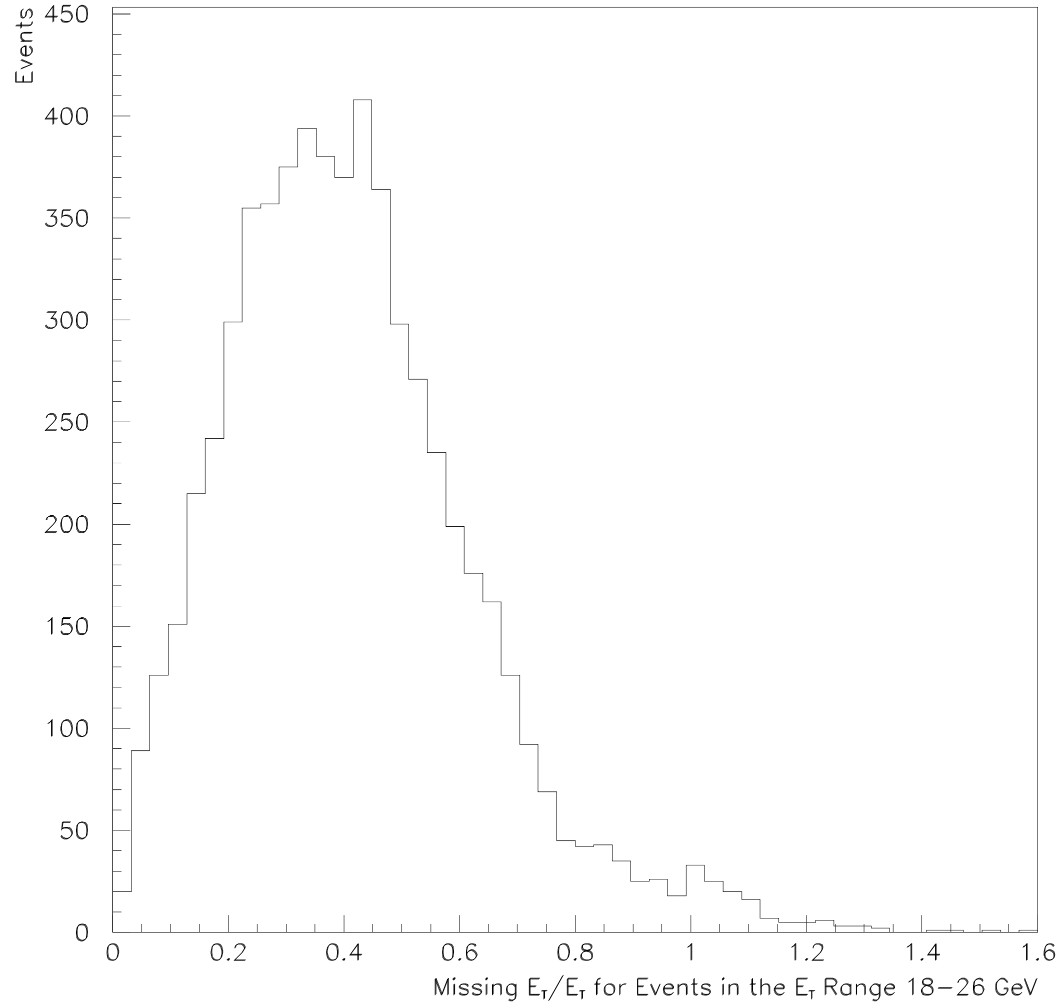

Figure 4.12: The missing E_T divided by photon E_T for photons between 18-26 GeV.

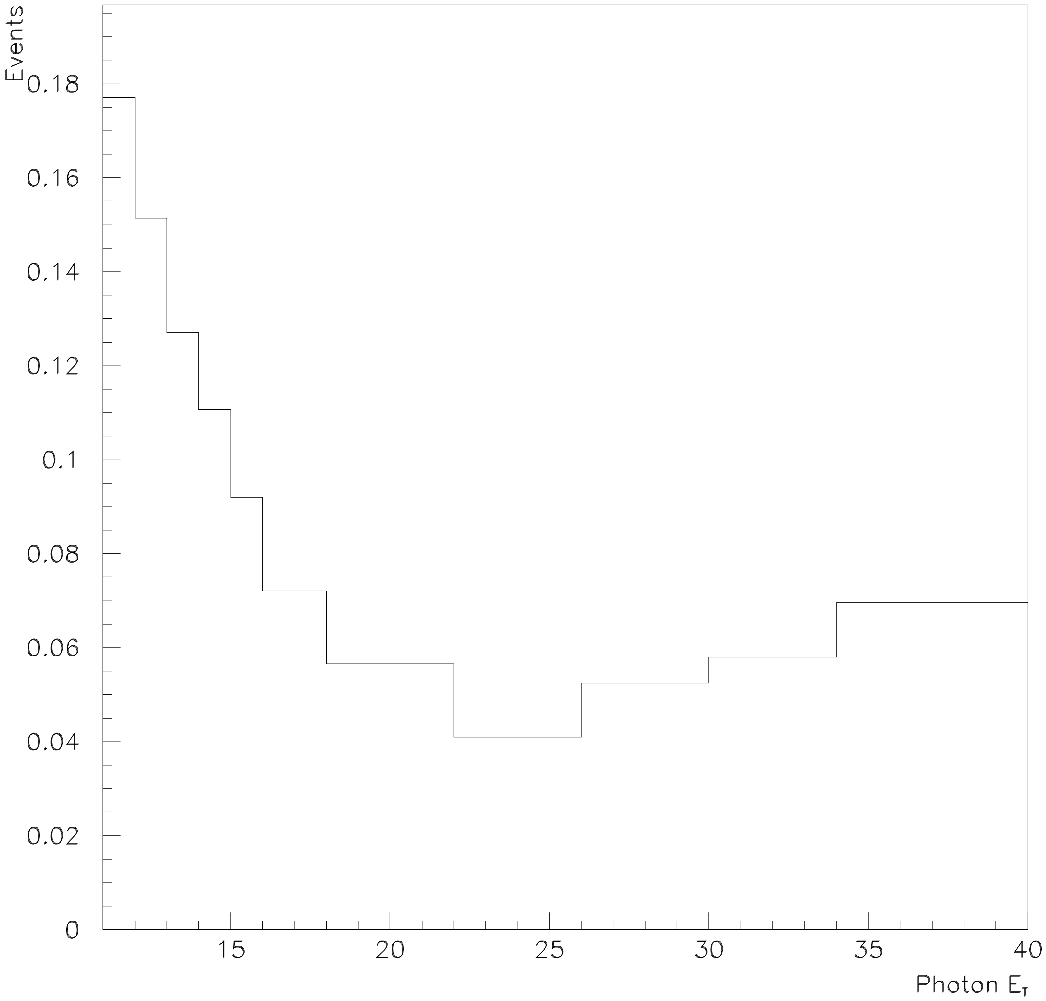

Figure 4.13: The fraction of events failing the missing E_T divided by photon E_T cut versus photon E_T.

Chapter 5

Statistical Background Subtraction

5.1 Background Separation Techniques

The profile (CES) and conversion (CPR) methods are the two ways that photons can be separated from the neutral meson backgrounds. The profile method uses a goodness to fit χ^2 comparison of the photon candidate's CES shower shape to that of test beam electrons with a similar momentum. The showers formed by two nearby photons from meson decays are more likely to be wider (have a larger χ^2) than those formed by a single photon. The CES method is very effective at low P_T as the showers should be widely separated. At high P_T the two photons from a meson decay are not well separated and have a χ^2 similar to single photons so it cannot be used in that region. The conversion method looks at the fraction of photon events that convert in the material before the CPR. The probability of a single photon converting is approximately 60% while the probability of the photons from a meson decay converting is greater than 80%. The CPR method is good for all P_T ranges, but the CES method is slightly better in the low P_T range

The data, which is a combination of signal and background, will have an efficiency somewhere between the two values. The number of single photon events is then determined by a background subtraction. The equation used to do the background subtraction is the same for both the CES and CPR methods.

$$N_\gamma = \left(\frac{\epsilon - \epsilon_b}{\epsilon_\gamma - \epsilon_b}\right) N \tag{5.1}$$

where N_γ is the number of photons, N is the total number of photons candidates per P_T bin, ϵ, ϵ_γ, and ϵ_b are the fraction of the total, photon, and background events that pass a fixed cut. The equation comes from $\epsilon N = \epsilon_\gamma N_\gamma + \epsilon_b N_b$ with $N_b = N - N_\gamma$. The conversion method efficiency is defined as the fraction of events that has a CPR hit rate greater than 500 fc out of all the events, and the profile method efficiency is the fraction of events that has a $\chi^2 < 4$ out of all the events that have a $\chi^2 < 20$. The conversion method will be used for the official photon cross section measurement and the profile method will be used as a check on that measurement.

Further descriptions of these methods and how they were used in previous analyses can be found in [23] [24].

5.2 The Conversion Method

The conversion method uses the fact that one of the two photons from a neutral meson decay will convert in the coil material in front of the calorimeter with a higher probability than a single photon. Direct and secondary photons pass the coil material ($\approx$ 1 radiation length) and some of them are detected in the CPR. Generally, the conversion probability for direct and secondary photons can be obtained from [25]:

$$P_\gamma = 1 - e^{-\frac{7}{9}X_0} \tag{5.2}$$

and

$$P_{\pi^0} = 1 - (1 - P_\gamma)^2 \tag{5.3}$$

where X_0 is the amount of material in radiation lengths. However, there are a number of corrections which need to be made and are discussed below.

For the conversion method ϵ is the fraction of photon candidates which produce a pulse height greater than that of a minimum ionizing particle (500 fc) in the CPR within a 66 mrad "window" (5 CPR channels) around the photon direction. (For reference the minimum separation of the photons from a 25 GeV/c π^0 is 11 mrad.) The expected values of ϵ are derived from the equation:

$$P = 1 - EXP\left(-\frac{7}{9}X_0 N_\gamma(P_T)\mathcal{P}\right) \tag{5.4}$$

where X_0 is the amount of material (in radiation lengths) in the solenoid coil, $\mathcal{P}$ is the photon pair production cross section [26], which has a slight energy dependence and the term $N_\gamma(P_T)$ is the effective number of photons detected within the CPR "window" [22]. Clearly, for a single direct photon $N_\gamma(P_T)$ is equal to 1. For low energy π^0's and η's the separation between the two photons is large enough that only one photon is in the "window." We also consider the other multi-photon decays of the η and K_s. These are all displayed in Fig. 5.1 which shows the number of detected photons in the CPR "window" versus particle P_T. At high P_T virtually all the photons are in the window all the time.

We have done a careful accounting of the material in the solenoid magnet and find that it is 0.9651 radiation lengths thick at 90°, including the outer wall of the CTC [25]. The complete chart of the material available for photon conversion is given in Table 5.1. The material listed does not include the Time of Flight detector. The Time of Flight detector is made of sixteen 4x4x30 cm scintillators covering the range $197° < \phi < 224°$ on the west side of the detector and four 4x4x30 cm scintillators covering the range $217° < \phi < 224°$ on the east side. That amount of scintillator should add approximately 0.1 X_0 in those regions.

The amount of material in front of the CPR chambers is not the only thing that can affect the CPR hit rate. We have to apply the additional corrections for CPR hits coming from the underlying event as well as dead CPR channels. The correction is

$$P_{UE} = \{1 - [(1 - P) \times UE]\} \times WC \tag{5.5}$$

where P is the probability from Equations 1 or 2, UE is the fraction of the time the underlying event does not produce a CPR hit, and WC is the fraction of working CPR channels (96.5%). In order to measure the underlying event CPR hit rate, we used minimum bias data. For each minimum bias event, we looped through all the central calorimeter wedges checking for a charged track pointing toward the wedge. If there was no track, then one tower in the range $0.0 < |\eta| < 0.5$ and one tower in the range $0.5 < |\eta| < 0.9$ was picked (one tower for each of the CPR chambers in front the wedge). To mimic the photon events a random x position was chosen for each CPR chamber in a region where the energy in a cone of radius 0.4 was less than 1 GeV, and a five channel clustering was performed about that position. Like the isolation and no track cuts, the CPR efficiency was found to be dependent on the number of vertices in the event. The results of the measurement are shown in Figs. 5.2 and 5.3. There is a 4.9% chance of a hit in a five channel window in the 1b data and a 3.2% chance of an underlying event hit in the 630 GeV data.

Finally, for low energy photons it is possible for part of the electromagnetic shower to travel at very large angles, almost backwards, with respect to the incoming photon. These photons can convert or Compton scatter and give a hit in the CPR. This effect is not included when considering the normal photon conversion in the solenoid material. Therefore, a detailed detector simulation called GEANT [27] was used to make an additional correction [22]. The correction to the conversion probabilities takes the form

$$P_{final} = ((1. - P_{UE}) \times BP) + P_{UE} \tag{5.6}$$

where the backscattering factor (BP) is

$$BP = 0.00074(P_T / \sin\theta) \tag{5.7}$$

and P_{UE} is the previously corrected probability. The correction is the same for both photons and mesons.

Figure 5.4 shows the measured CPR efficiencies for the Run 1b and 630 GeV data along with the efficiencies for signal and background which are obtained from simulation and data. The efficiency curves include all discussed corrections. The photon curve does not have a P_T dependence. There is only a slight P_T dependence in the background curve at high P_T when all secondary photons are within the CPR and the approximation given by Eq. 5.2 is valid. At high P_T we can calculate the number of photons in each P_T bin using Eq. 5.1.

5.3 The Profile Method

The prompt photon events have a single isolated photon shower in the calorimeter. The background is composed of multiple photon showers with some spatial separation. The essence of the transverse shower profile method is to identify a class of events whose measured profiles are unlikely to be produced by a single shower. For P_T values above 15 GeV/c it is usually not possible to resolve the individual showers from the two photons from a π^0 decay. Therefore we use a statistical subtraction of the neutral meson background. For a large enough sample of events consisting of both single showers and π^0 induced showers, we evaluate the fraction of π^0 events from the number of showers that are "too broad" to be consistent with a single electromagnetic shower. The number of π^0 showers that are indistinguishable from single photons can be inferred from the measured number of the "broad" showers using the characteristics of the π^0 decay and of the detector.

To measure the transverse profile of electromagnetic showers we use the central electromagnetic strip detector, which is positioned in the CEM at the shower maximum (≈ 6 radiation lengths). At first a simple algorithm selects *seed* channels which have energy above 0.5 GeV and sums up the energy of a cluster around them using 11 channels in both strip and wire planes [28]. We use an effective threshold of 40 ADC counts (57.2 MeV) for the inclusion of a channel energy in the cluster. Channels with energy below this threshold are set to zero. The transverse energy distribution in the cluster vs channel number is the transverse profile of the electromagnetic shower.

The expected electron transverse profile which we use as a parent distribution for all fits was obtained from the 1985 test beam data for 50 GeV electrons. The strip and wire views of the standard profile depend differently on the position of the shower. The wire profile is independent of the X position of the shower and is symmetric about the shower center. Unlike the wire-view, the strip view has a Z dependence and therefore is not symmetric. This dependence has a pure geometrical origin and comes from the "widening" of the shower by a factor of $1/\sin\theta$ when the electron is at angle θ. This "widening" can be removed by a change of coordinates

$$Z \rightarrow Z' = Z \sin\theta \tag{5.8}$$

After determining the standard profile, we fit the transverse profile of the electromagnetic shower by the standard profile and calculate the χ^2:

$$\chi^2 = \frac{1}{4}\sum_{i=1}^{11} \frac{[y_i - y(x_i)]}{\sigma_i^2} \tag{5.9}$$

where i is the cluster channel index, y_i is the measured profile (either strip or wire) normalized to unity, $y(x_i)$ is the standard electron profile, and σ_i^2 is the estimated variance of the electron profile. After calculating the χ^2 for each CES plane, the final χ^2 of the fit is defined as the average:

$$\chi^2 = (\chi^2_{wire} + \chi^2_{strip})/2 \tag{5.10}$$

Figure 5.4 shows the χ^2 distributions for simulated signal and background showers.

The efficiency ϵ of the profile method is defined as the fraction of photon candidates with $\chi^2 < 4$. This efficiency can be measured from data and determined from simulation for direct photons and background. The multiple photon background consists primarily of single, isolated π^0 and η mesons with a small fraction of other multipion states. To simulate the background correctly, we need to know its composition. The η/π^0 ratio was measured by selecting two-photon events and reconstructing their invariant mass [29]. The production rate after relative acceptance corrections was estimated to be 1.02 for Run 1b.

The ratio may be different at 630 GeV. There is expected to be a trend toward smaller ratios at smaller energies. Isolation may play an important role as well, since π^0's can come from $\rho^{\pm}$ decays and isolation and no-track cuts will reduce the number of them. The UA2 experiment (a $p\bar{p}$ collider detector located at CERN with a center of mass energy equal to 630 GeV) measured a ratio of 0.6 at lower P_T and no isolation cuts [30]. For the 630 GeV data, we will split the difference and use 0.8 ± 0.2 for the η/π^0 ratio. This should cover all the possibilities.

Figure 5.5 presents the profile method efficiencies vs. photon P_T. The curves are the expected signal and background , and the points show the actual data. The data, which is a mixture of signal and background, has efficiencies lying between the two curves. Using the efficiencies in each bin to for data and the expected signal and background values, we can calculate the number of prompt photon events by doing a background subtraction.

Description	Composition	Thickness (cm)	Radiation Lengths (X_0)	Uncertainty Estimate
CTC Outer Wall	Al	0.793	0.0891	0.009
Cryostat Wall	Al	0.700	0.0787	0.011
Inner Rad. Shield	Al	0.232	0.0261	0.003
Coil	Al	0.456	0.0512	0.005
Superconductor+Cu	NbTi+Cu	0.153	0.1071	0.005
Coil	Al	1.367	0.1536	0.002
Coil FRP	G10	0.280	0.0144	0.001
Coil	Al	1.600	0.1798	0.002
Outer Rad. Shield	Al	0.227	0.0255	0.003
Cryostat Wall	Al	2.000	0.2247	0.011
CPR Cover	G10	0.159	0.0082	0.001
G10 Cu Cladding	Cu	0.015	0.0107	0.001
		Total	0.9651	0.020

Table 5.1: The amount of material available for photon conversions at 90° incidence. There is an additional 0.1 X_0 of material from the Time Of Flight Detector in a limited ϕ range.

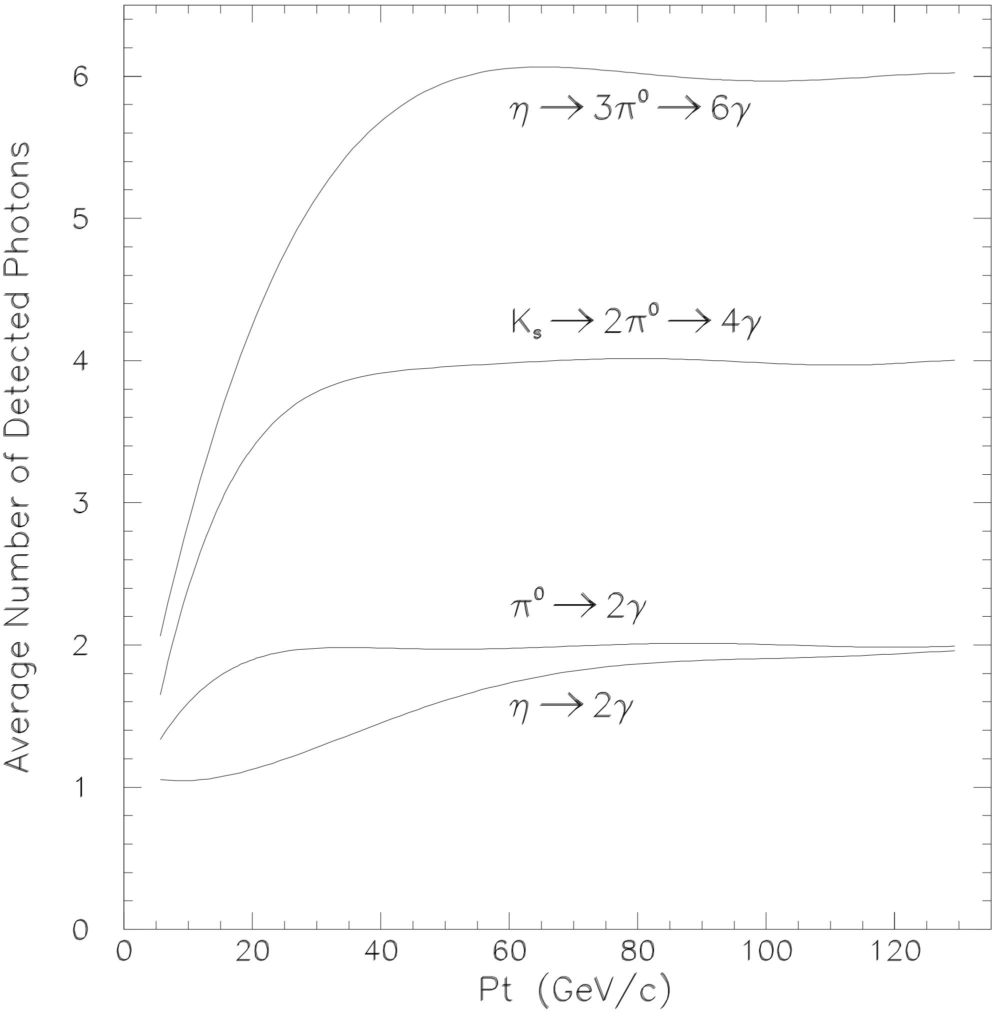

Figure 5.1: The average number of detected photons in the CPR for the different decay modes.

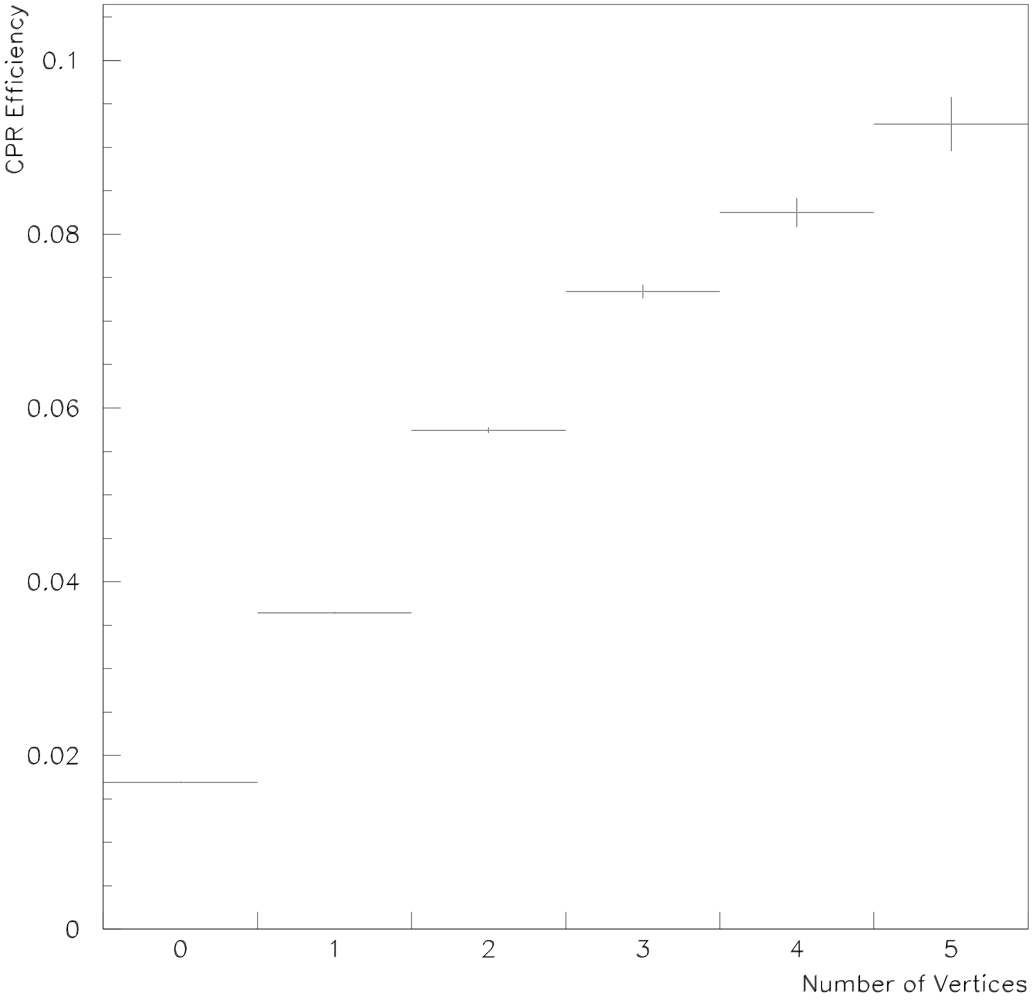

Figure 5.2: The measured CPR hit rate efficiency (fraction of events with a CPR pulse height of 500 fc of all events) as a function of the number of class 12 vertices in the event from the Run 1b minimum bias data sample.

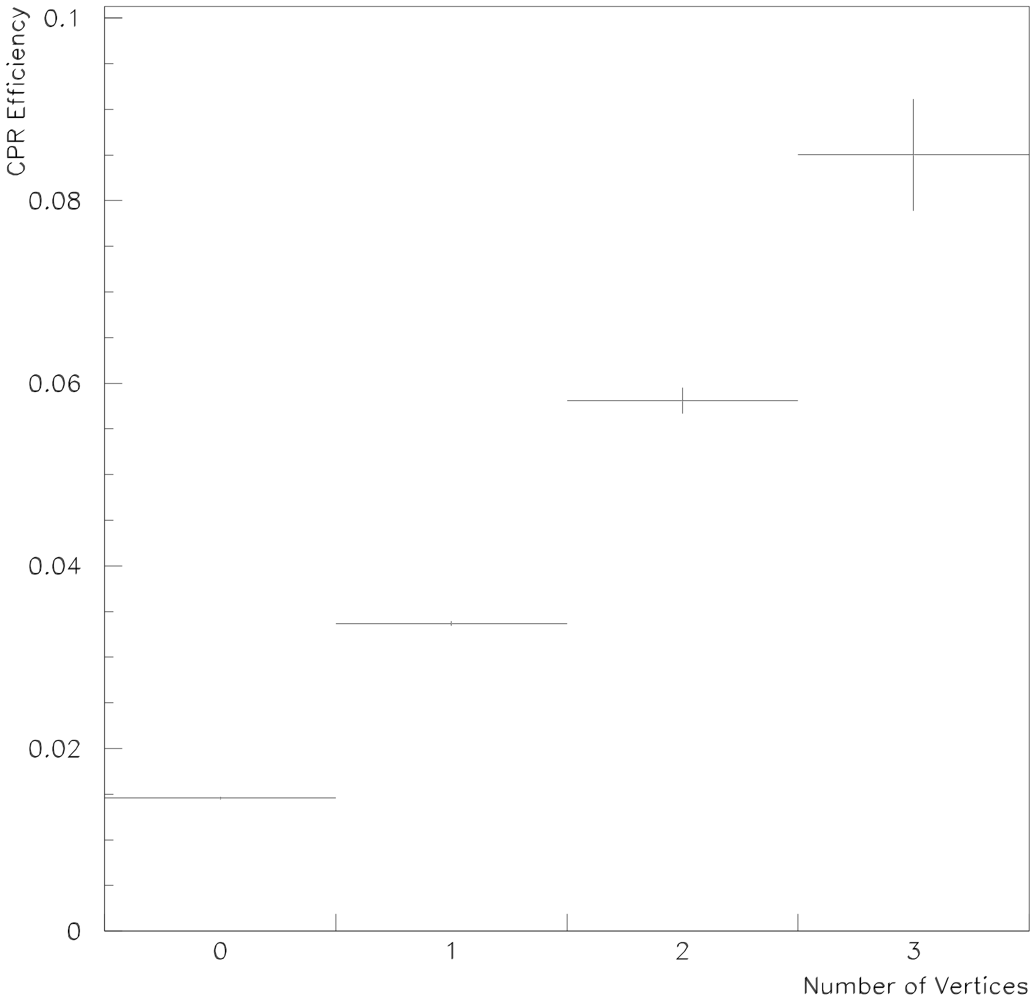

Figure 5.3: The measured CPR hit rate efficiency (fraction of events with a CPR pulse height of 500 fc of all events) as a function of the number of class 12 vertices in the event from the 630 GeV minimum bias data sample.

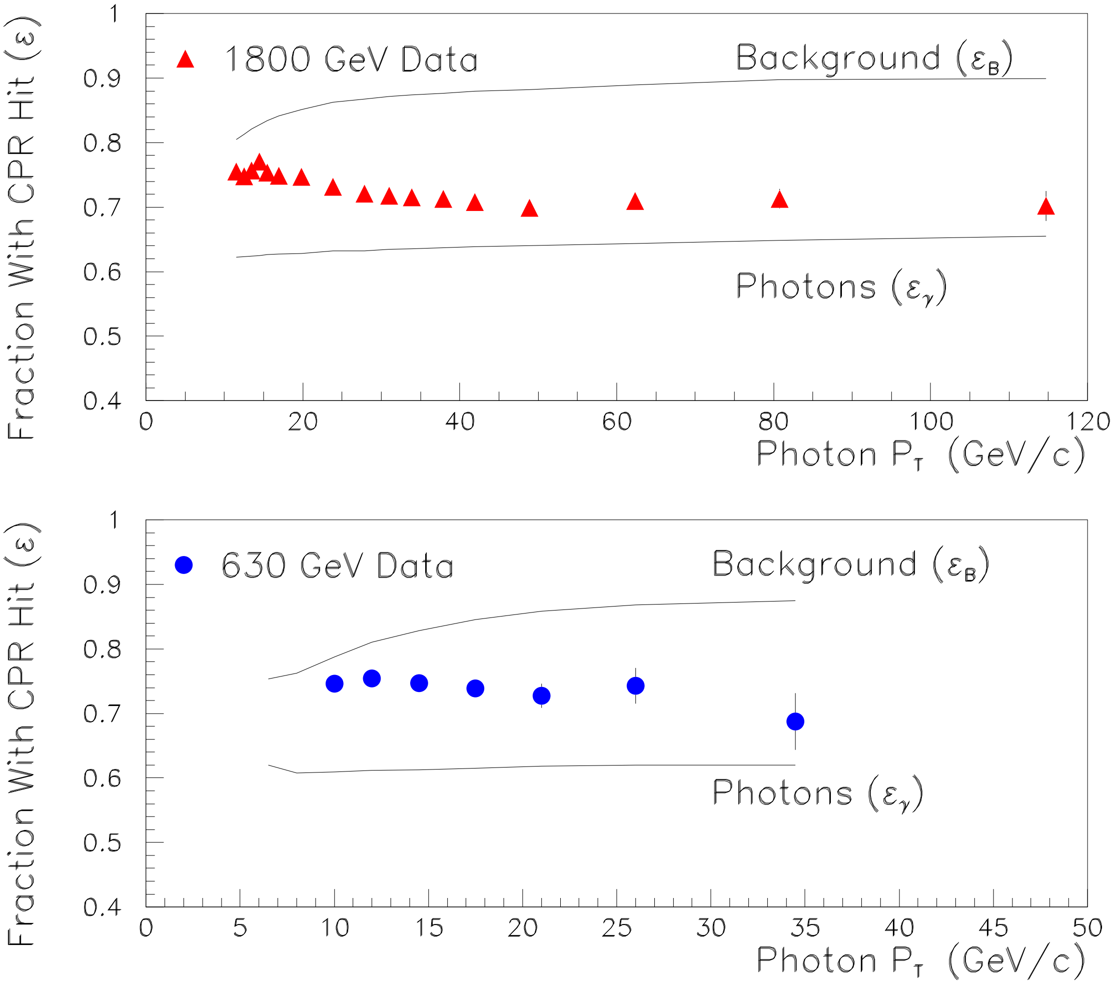

Figure 5.4: CPR efficiencies vs. P_T for the Run 1b and 630 GeV data and for simulated signal and background.

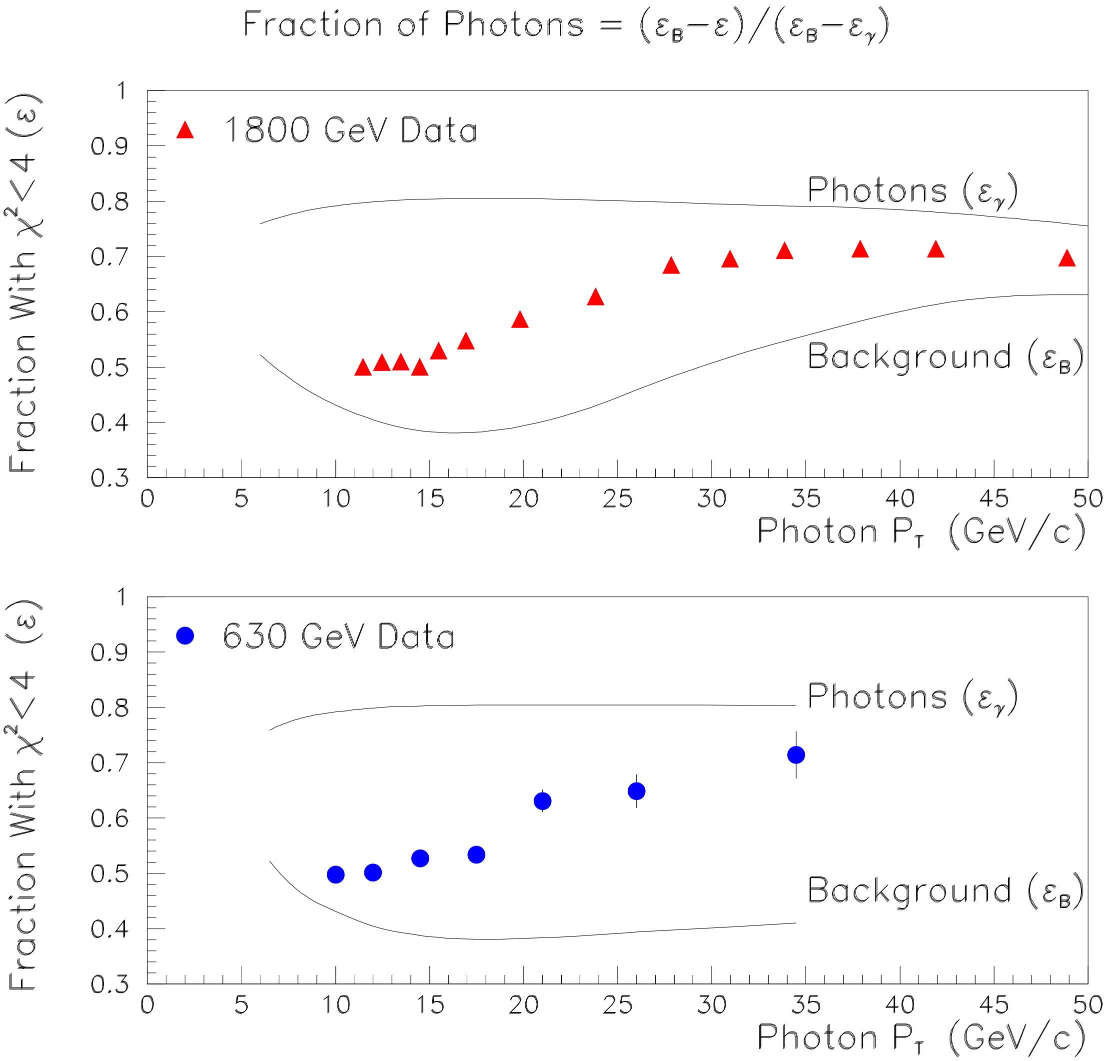

Figure 5.5: CES efficiencies vs. P_T for the Run 1b and 630 GeV data and for simulated signal and background.

Chapter 6

Systematic Uncertainties

6.1 Calibration of Efficiencies

To estimate both the conversion and profile method uncertainty we reconstructed η and $\rho^{\pm}$ mesons decaying to photons and measured the CPR hit rate efficiency and the CES efficiency with that expected from a Monte Carlo simulation. The disagreement between the measurement and simulation was used as a measure of the systematic uncertainty for ε_b. The systematic uncertainty for ε_γ can be easily calculated from the systematic uncertainty of ε_b because of the complete correlation between these uncertainties.

We will start the description of this analysis with the reconstruction of the $\rho^{\pm}$ and η meson peaks.

6.1.1 Rho Event Selection

All the $\rho^{\pm}$ events were taken from the 23 GeV isolated photon trigger. The selected events had a single charged track in association with an electromagnetic shower. The π^0 candidates were electromagnetic clusters that passed the standard single photon cuts as follows [31]:

- $|\eta| < 0.9$
- $\chi^2 < 20$
- |CES x| < 17.5 cm
- 14 cm < |CES z| < 217 cm
- the energy in cone of radius 0.4 < 4 GeV
- the energy in a second CES cluster < 1 GeV
- no 3-D tracks pointing towards the cluster
- $|Z_{vertex}| < 60$ cm

The $\pi^{\pm}$ candidates were charged tracks. The invariant mass for all the possible combinations was then reconstructed. The combination was kept if the invariant mass was less than 2 GeV and rejected if the invariant mass was larger than 2 GeV. A $\rho^{\pm}$ peak was found above the background after the following cuts were used:

- the π^0 candidate was required to have a $P_T > 23$ GeV/c
- the charged track was required to have a $P_T > 1.4$ GeV/c
- cos θ^* < -0.92, where cos θ^* is the angle between the $\pi^{\pm}$ direction in the $\pi^{\pm}\pi^0$ center of mass frame and the $\pi^{\pm}\pi^0$ direction in the lab frame. This cut ensures the $\rho^{\pm}$ decay is asymmetric with a high energy π^0 and a low energy $\pi^{\pm}$. Therefore, the resolution of both charged and neutral pions is optimized.

The distributions for the three variables as well as the $\rho^{\pm}$ invariant mass before the cuts are applied are shown in Fig. 6.1. The final mass distribution is found in Fig.

6.2. It was fit with the function (BW + constant)ε to get a flat background where BW is a Breit-Wigner resonance curve and

$$\varepsilon = 0.5(1 + tanh(6.165(M - 0.566))) \tag{6.1}$$

The constant is equal to 57.50. The signal function is taken to be $BW * \varepsilon$ and the background function is $57.50 * \varepsilon$. The solid curve shows the signal plus background fit. The dashed line shows the signal curve, and the dotted line shows the background curve. The signal region is determined to be in the interval $0.6 < M < 0.95$, and the background region is determined to be in the interval $1.7 < M < 2.0$.

6.1.2 Measured and Expected CPR Efficiencies

Before measuring the efficiencies, we had to further restrict the π^0 P_T to be between 25 and 36 GeV. This ensures that the 23 GeV trigger is efficient and that the P_T remains in the region where the CES is still useful. The CPR efficiency (number of events with a CPR hit rate greater than 500 fc divided by all the events) is shown in Fig. 6.3. The vertical lines indicate the peak region. The CPR hit rate efficiency is 0.866 ± 0.006 in the peak region. The P_T distributions in both the signal and background regions were also looked at to see if a background subtraction should be done to find the π^0 efficiency. As can be seen in Fig. 6.4, the P_T distributions are different. Because the CPR efficiency is expected to have a slight P_T dependence in this P_T region, a background subtraction should not be done as it was in the previous analysis [32]. Therefore, the π^0 efficiency is the efficiency in the signal region.

We originally compared our results to those of a CDF detector simulation called QFL [33] [34]. QFL predicted a CPR efficiency of 0.800 ± 0.002. The huge difference between data and QFL was caused at least in part by the fact that the simulation did not include any underlying event corrections. We thought we could make a better prediction of the true background efficiency by actually calculating the efficiency using Equations 5.2 through 5.6. The predicted efficiency is then based on the actual location and P_T of the pions and corrected for the underlying event and backscattering. The CPR efficiency calculated this way is 0.838 ± 0.006. Therefore, the difference between the data and Monte Carlo is 0.028 ± 0.008, which is still a significant deviation.

6.1.3 Measured and Expected CES Efficiencies

The CES efficiency (number of events with $\chi^2 < 4$ divided by the number of events with $\chi^2 < 20$) is shown in Fig. 6.5. The CES efficiency is expected to have an even greater P_T dependence than the CPR efficiency so again, the sideband subtraction was not done. The pion's efficiency is taken as the measured value of 0.458 ± 0.009 in the $\rho^{\pm}$ peak region.

The measured CES efficiency was then compared to the results of a QFL simulation. The Monte Carlo CES efficiency is 0.472 ± 0.004. The difference between the data and the Monte Carlo predictions is -0.014 ± 0.010. While the discrepancy between the data and Monte Carlo is not a large as it was for the CPR efficiency, it is still larger than it was in the 1a analysis, and, therefore, should be investigated.

6.1.4 Eta Event Selection

The event selection was similar to the 1a event selection and that of older analyses [31] [25]. The basic data set was taken from events that passed the 10 GeV isolated photon trigger We looped over all electromagnetic clusters in each event and passed the event if at least one of the EM clusters met the following requirements. The cluster had to be in the central calorimeter with no 3-D tracks pointing to the cluster. The CES clusters were formed using 11 channels with a seed threshold of 0.5 GeV.

Each EM cluster was then required to contain at least two CES strip clusters and 1 CES wire cluster. The two highest energy CES strip clusters were used to determine the position of the two photons from the η decay and were required to be in different EM towers. Both photons had to be contained in the CES and CPR fiducial volume: $|\text{CES x}| < 17.5$ cm and $|\text{CES z}| < 217$ cm. The CES strip clusters were isolated with the strip isolation defined as the ratio of the energy in extra strip clusters to the energy of the two leading strip clusters:

$$I_s = \sum_{i=3}^{n} \frac{E_{si}}{(E_{s1} + E_{s2})} \tag{6.2}$$

The wire isolation is defined similarly. Both the strip and wire isolation were required to be less than 0.2. These cuts reduce the multi-π^0 background. Lastly, to eliminate background from single photons that fluctuated to produce a second cluster, an asymmetry cut was used. The two photon asymmetry is defined as

$$Asymmetry = \frac{|E_1 - E_2|}{E_1 + E_2} \tag{6.3}$$

where E_1 and E_2 are the photon energies. The asymmetry was required to be less than 0.75.

The invariant mass of the two photons was calculated using the formula

$$M^2 = 2E_1E_2(1 - \cos\theta_{12}) \tag{6.4}$$

where $\cos\theta_{12}$ is the angle between the two photons. It can be written in terms of X and Z as

$$\cos\theta_{12} = \frac{R^2 + Z_1Z_2 + X_1X_2}{\sqrt{(R^2 + Z_1^2 + X_1^2)(R^2 + Z_2^2 + X_2^2)}} \tag{6.5}$$

where $R = 184.15$ cm which is the radial distance to the center of a CES chamber and Z has been corrected for the event vertex. The final mass distribution can be seen in Fig. 6.6. The distribution was fit with a Gaussian plus a quadratic polynomial (solid curve). The dashed curve shows the background. The solid vertical lines show the η signal region which is taken to be in the mass range $0.5 < M < 0.61$.

The dashed vertical lines show the background regions which are in the mass range $0.2 < M < 0.45$ and $0.67 < M < 1.0$.

6.1.5 Measured CPR Efficiency

The CPR efficiency is shown in Fig. 6.7. Again the solid vertical lines indicate the signal region and the dashed vertical lines indicate the background regions. The average efficiency in the peak region is 0.857 ± 0.004. The background efficiency is 0.916 ± 0.003 in the low mass region and 0.879± 0.003 in the high mass region. Both of those values are shown in the plot by the dotted horizontal lines. The average of the two values is indicated by the solid horizontal line. A background subtraction was done using the formulas

$$\epsilon_\eta = \frac{N_{peak}}{N_\eta}\epsilon_{peak} - \frac{N_{back}}{N_\eta}\epsilon_{back} \tag{6.6}$$

and

$$\sigma_\eta^2 = \left(1 + \frac{N_{back}}{N_\eta}\right)^2 \sigma_{peak}^2 + \left(\frac{N_{back}}{N_\eta}\right)^2 \sigma_{back}^2 \tag{6.7}$$

where N_{peak} =8965 is the total number of events in the peak region, N_{back} =7146 is the number of background events in the peak region, N_η = (8965 - 7146) is the number of true η's in the peak region, and the ϵ's are the efficiencies in the peak and background regions. Because the efficiencies are different in the two background regions it is not clear what is the actual background efficiency in the signal region, which makes a background subtraction difficult. A background subtraction using the average background value, gives an efficiency of 0.696 ± 0.025 (stat error only) for the η while the subtraction of the sideband efficiencies gives values of 0.625 ± 0.023 (using 0.916) and 0.771 ± 0.023 (using 0.879). It is impossible to know the efficiency with any precision which makes a comparison to Monte Carlo very difficult. The η measurement, therefore, cannot be used as a check on the photon efficiencies for the photon cross section the way the $\rho^\pm$ measurements were used for the background efficiencies.

6.2 Difference Between Data and MC

Several checks were done to discover the source of the discrepancy between the data and Monte Carlo. Since the measured CES and CPR efficiency agreed with predictions in the Run 1a analysis, we decided to focus on the things that had changed between the two runs, such as luminosity and the underlying event.

6.2.1 Energy Calibrations

The first check was of the CES strip and wire energies. The gas quality in the CES changed in the middle of the run which can affect the energy calibration. The simulations contained the assumption that the strip and wire transverse energies were equal to the cluster transverse energy. The plot of that quantity (Fig. 6.8) shows this assumption was incorrect. The CES strip and wire energies are 25% too low. Therefore, the second cluster cut (second strip and wire energies less than 1 GeV) is not as efficient as expected. Extra background events were let into the sample. Unfortunately, the CES strip and wire energies were not stored in the original rho data sets so they had to be remade. Then $\rho^{\pm}$ CES and CPR efficiencies were recalculated after the energy corrections were applied to the data and a Z_{vertex} cut ($|Z_{vertex}| < 60$ cm) was applied to both the data and the Monte Carlo. The CES discrepancy was eliminated. The CPR discrepancy was slightly decreased, but since the new data sample started off with a larger CPR discrepancy, the overall discrepancy was increased to 0.035 (Figures 6.9 and 6.10).

6.2.2 Detector Studies

Resolving the problem with the CES allowed us to focus on the CPR. We first checked that the CPR was working properly by studying the pulse height distribution from the rho data. Figure 6.12 shows the rho CPR pulse height distribution as well as the CPR pulse height distribution predicted by QFL. It is clear that the fraction of the rho events have a pulse height less than 500 fc is larger than expected. To find out if the large fraction of rho events with a pulse height less than 500 fc came from the underlying event or if it was caused by a problem with the CPR, we looked the CPR pulse height distribution from electrons from W decays. Because electrons are electrically charged, they should always produce a CPR hit. Figure 6.13 shows the results of that study. There are still events with a CPR pulse height less than 500 fc. Further investigations showed that most of those electrons went into gaps in the detector. Therefore, we concluded that the problem with the rho's came from the underlying event rather than a problem with the CPR.

While we the pulse height distribution studies made clear that overall the CPR was working properly, it could not show if there were specific regions where the detector was working improperly. In order get a more detailed look at the detector, we checked the CPR efficiency as a function of wedge number. If the detector is working properly, the efficiency should be flat as a function of wedge number. The plot of this efficiency using the minimum bias sample from the underlying event studies is shown in the top plot of Fig. 6.14. The efficiency is essentially flat as a function of wedge number. The one low point was expected because there is a crack in the detector (see Section 4.1). The few wedges with efficiencies higher than average were not expected. To see if they have any effect on the photon analysis, the CPR efficiency from the $\rho^{\pm}$ and the 23 GeV isolated photon data was also plotted as a function of wedge number. As can be seen in the bottom plot of Fig. 6.14, the efficiency flattens out. Therefore, a problem with the detector does not seem to be the source of the discrepancy.

We also used the 23 GeV isolated photon data (before the background subtraction) to see if the Time of Flight detector component had any effect on the CPR hit rate. The addition of approximately $0.1X_0$ to the amount of material in front of the CPR should increase the π^0 CPR hit rate by 0.02 and the photon hit rate by almost 0.03. Figure 6.15 shows the CPR hit rate for the west side of the detector. It is clear that the CPR hit rate was not affected by the additional material. The east side of the detector had similar results.

6.2.3 Luminosity Studies

One other check was to see if the CPR efficiency changed with time and/or luminosity. The ρ data was divided into 3 groups of runs, and the efficiencies and mean luminosity were calculated for each group.

Runs	ϵ_{CPR}	Mean Lum
55273-60522	0.879 ± 0.016	2.2
60523-65772	0.862 ± 0.010	7.0
65773-71023	0.856 ± 0.010	10.3

As another check the efficiencies were also plotted as a function of luminosity. Figure 6.11 shows the efficiency versus luminosity fitted with a line. Also shown on the plots is the average efficiency versus the mean luminosity for each group of runs. As can be seen on the plots, they are consistent with each other.

While the CPR efficiency does appear to be correlated with the luminosity, it is not clear that the change in luminosity is the source of the changes in the efficiency. The CPR efficiencies seems to be going in the wrong direction. It would be more logical for the CPR efficiency to increase with the luminosity as it should increase the likelihood of something in the underlying event hitting the CPR.

6.2.4 Underlying Event

One possible explanation for the CPR discrepancy is that we did not get the underlying event hit rate correct because the min bias data did not accurately mimic the rho's underlying event. To check this theory, we analyzed a non-isolated photon sample using the same code and methods as in the min bias study. Figure 6.16 shows a comparison of the two data samples. Clearly, the non-isolated photon sample produces a CPR hit more often than the min bias sample. Therefore, we decided to use the CPR efficiency from the non-isolated photon sample. This decreased UE from 0.951 to 0.937 and reduced the rho CPR discrepancy from 0.035 to 0.033.

6.2.5 Background Studies

Our predictions for the background CPR efficiency depends on the background composition. In the rho analysis, we assumed that all the events in the peak were π^0's. We needed to test this assumption. The rho background fit predicts that 5.5% of the events in the rho peak are background events. The rho background should be the same as the photon background which is some combination of pions, etas, and other neutral mesons. Based on the 1989 estimates of the CDF photon background [23], approximately 75% of the photon background in the rho's P_T region should be made of π^0's. Therefore, more than 98% of the events in the rho peak should involve π^0's. The remaining 2% of the background should have very little effect on the CPR efficiency prediction. If we assume that the events in the rho peak only contains 75% pions, the predicted CPR efficiency would only increase by 0.007. Therefore, it seems unlikely that the background mixture is the source of the problem.

6.2.6 630 GeV $\rho^{\pm}$ Analysis

Because we do not know the source of the CPR discrepancy, we have no way of knowing how the 630 GeV CPR efficiency might be affected. We performed the $\rho^{\pm}$ analysis on the 630 GeV data to determine if the 630 GeV data was affected by the same problem with the CPR. The 630 GeV data was filtered through the same code as the Run 1b data. A few of the cuts were modified. The π^0 candidates were required to have an $E_T > 9$ GeV. The track P_T had to be greater than 0.7 GeV/c and cos θ^* had to be less than -0.90. The resulting rho peak is shown in Fig. 6.17 and the measured and expected CPR efficiencies are shown in Fig. 6.18. The measured efficiency is 0.814 ± 0.008 and the expected efficiency is 0.781 ± 0.008. The difference between the data and theory is 0.033, which is the same value found in the Run 1B data.

6.3 CPR Systematic Uncertainties

The source of the changes in the CPR efficiency remains unclear, but it is clear that the background efficiency at least needs to be corrected. We have no way of knowing if the signal efficiency also needs to be corrected or by how much. The size of the photon efficiency corrections depends on the source of the problem. If the source of the problem is the background mixture, then the photon efficiency does not need to be corrected at all. If the underlying event is the source of the error, then the Run 1b photon efficiency would have to be increased by 0.064. Another possibility is that the source will have the same effect on photons as mesons and the photon efficiency should be increased by the same amount as the background efficiency. Since the source is most likely some complicated combination of the sources we studied, we decided to use the photon efficiency correction that best agrees with the CES cross section and to use another correction to estimate the size of the systematic error.

To get some idea of the photon efficiency's correction effect on the cross section we divided the CPR cross section most consistent with the CES cross section (adding 0.010 to the photon efficiency and 0.033 to the background efficiency) by the cross section where 0.033 was added to both the photon and background efficiency. This is the weighting error plot shown in Figs. 6.19 and 6.20. It varies from 15% at low P_T to 10.6% at high P_T for both the Run 1b and 630 GeV data sets.

As mentioned earlier, the background efficiency depends on the ratio of particles it contains. The uncertainty in the knowledge of the background composition is a source of systematic error. The dominant error is the knowledge of the production ratio of η to π^0 mesons. The η/π^0 ratio was measured by selecting events in which the η or π^0 decay into two photons and correcting for the relative acceptance using a Monte Carlo simulation. The change in the ratio of the particles leads to a change in the background efficiency of 0.008. The error varies from 11% at low P_T to 0.4% at high P_T for the Run 1b data and from 12.4% to 0.9% for the 630 GeV data.

For the backscattered photon and electron we use only half of the correction as a systematic uncertainty. This a systematic error in the cross section of 2.4% at low P_T and 6.3% at high P_T for the 1B data and 1.6% at 9 GeV/c and 2.2% at 33 GeV/c for the 630 GeV data.

6.3.1 Other Systematic Uncertainties

The uncertainty in the P_T scale is less that 1%, the same as that in the W boson mass measurement [35]. When this is convoluted with the falling spectrum, it results in a cross section uncertainty of 4.5%.

Finally, there are additional uncertainties due to luminosity (4.1% for Run 1B and 4.4% for the 630 GeV data [14]) as well as the uncertainties from the event selection requirements. The total systematic errors are shown in Figs. 6.21 and

6.22.

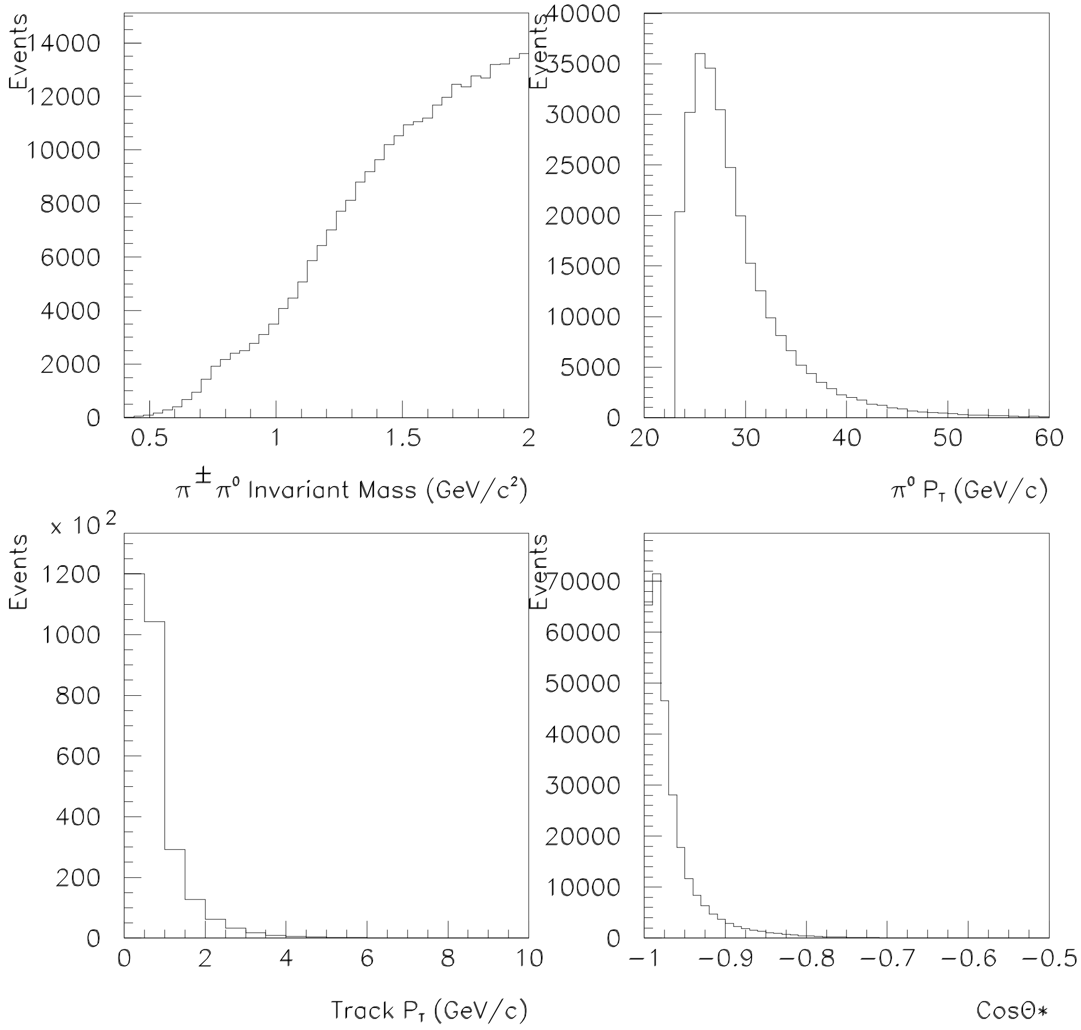

Figure 6.1: The $\pi^{\pm}$ π^0 invariant mass distribution before any cuts have been applied, π^0 P_T distribution, the $\pi^{\pm}$ P_T distribution and the $\cos\theta^*$ angular distribution for the $\rho^{\pm}$ candidates.

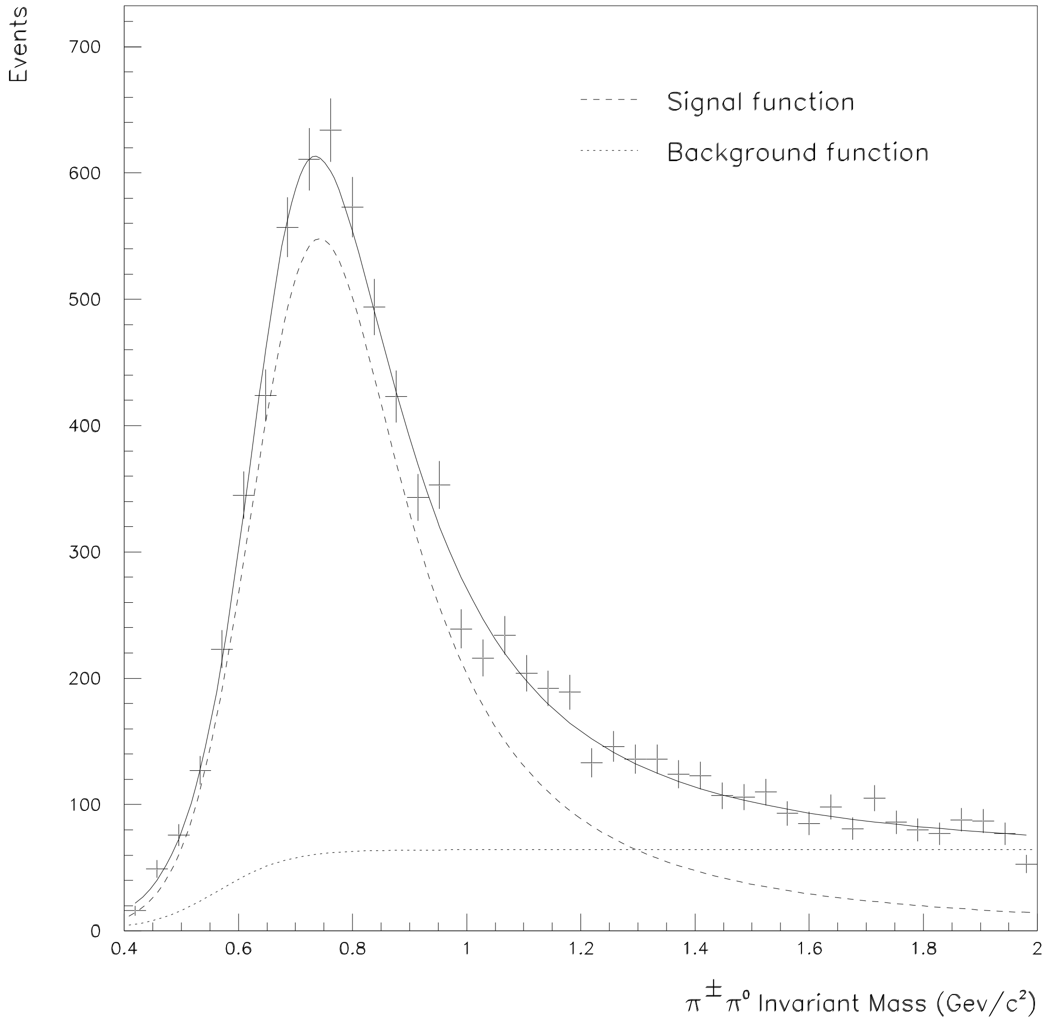

Figure 6.2: The measured $\pi^{\pm}\pi^{0}$ mass distribution. The solid curve shows the signal plus background fit. The dashed line is the signal curve, and the dotted line is the background curve. The PDG $\rho^{\pm}$ mass value is 0.770 GeV/c^2, and the measured value is 0.767 GeV/c^2.

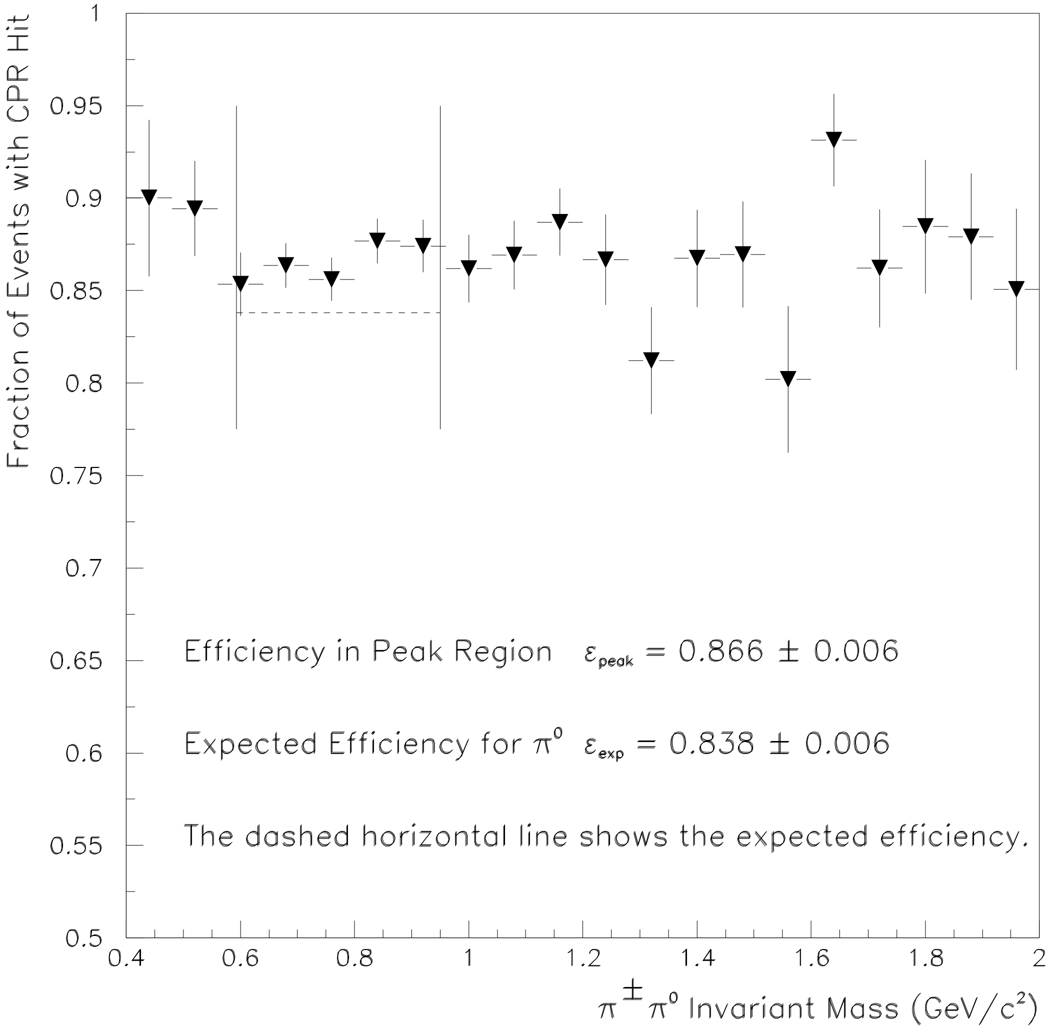

Figure 6.3: The measured CPR hit rate efficiency (fraction of events with CPR hit $>$ 500 fc out of all events). The solid vertical lines on the plot indicate the the signal region. The dashed horizontal line indicates the expected efficiency. The peak efficiency is the average efficiency between the vertical lines.

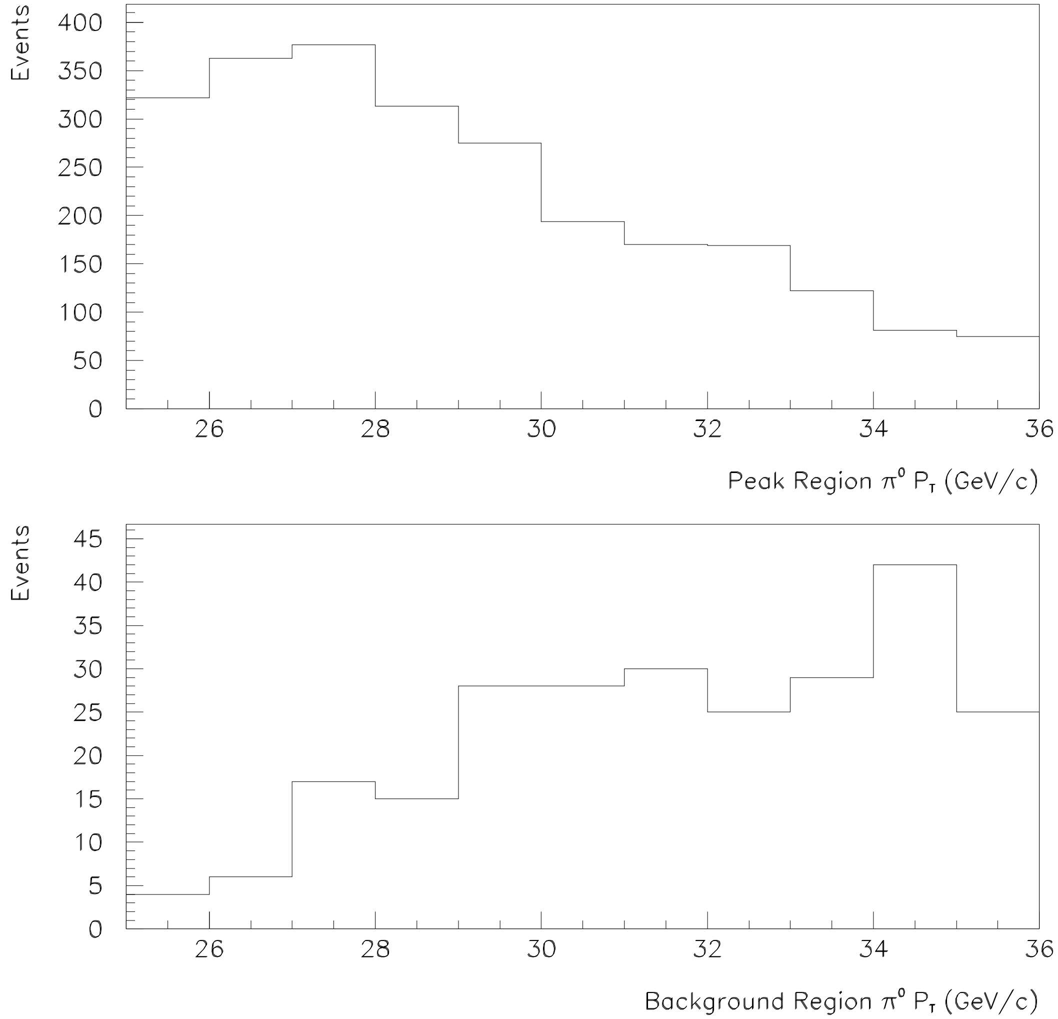

Figure 6.4: The π^0 P_T distributions in the signal and background regions.

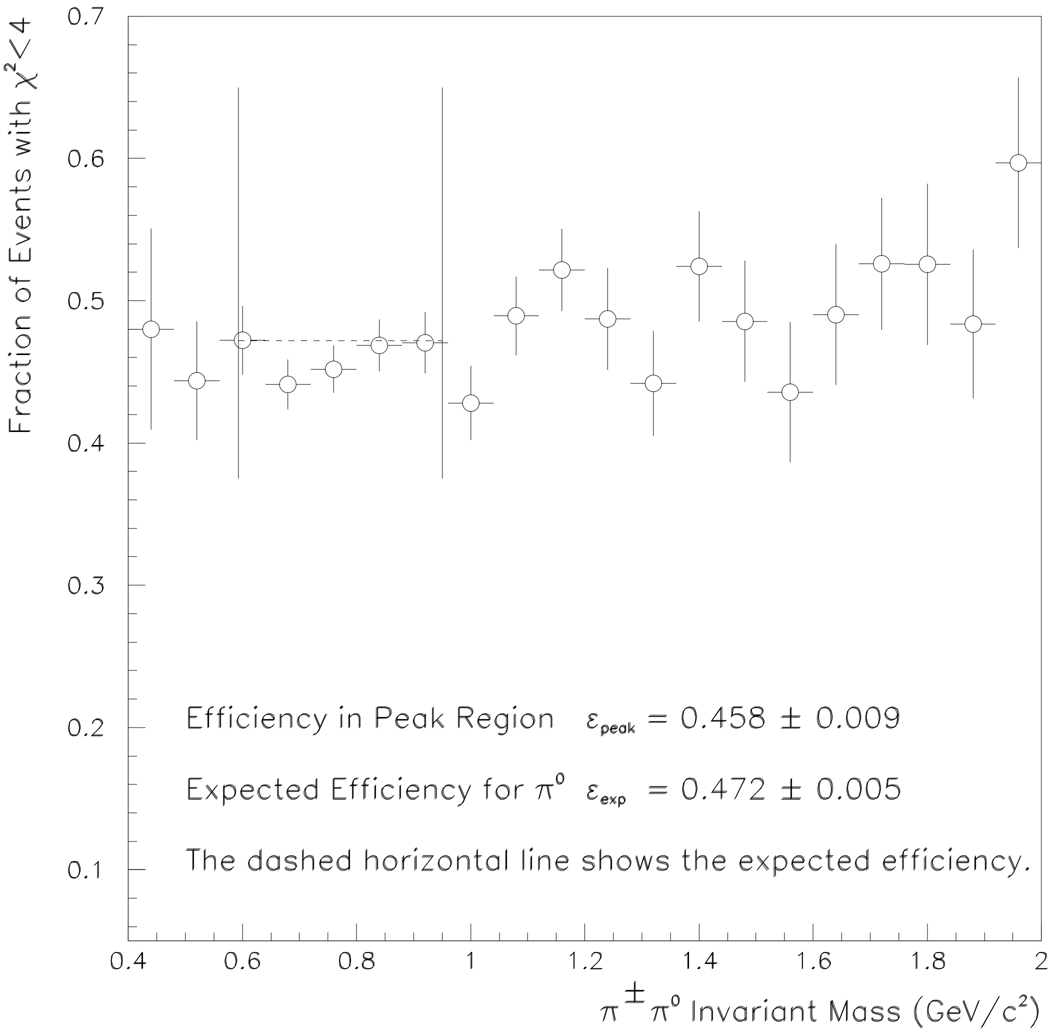

Figure 6.5: The measured CES efficiency (fraction of events with $\chi^2 < 4$ out of all events with $\chi^2 < 20$). The solid vertical lines on the plot indicate the signal region. The dashed horizontal line indicates the expected efficiency from QFL. The peak efficiency is the average efficiency between the vertical lines.

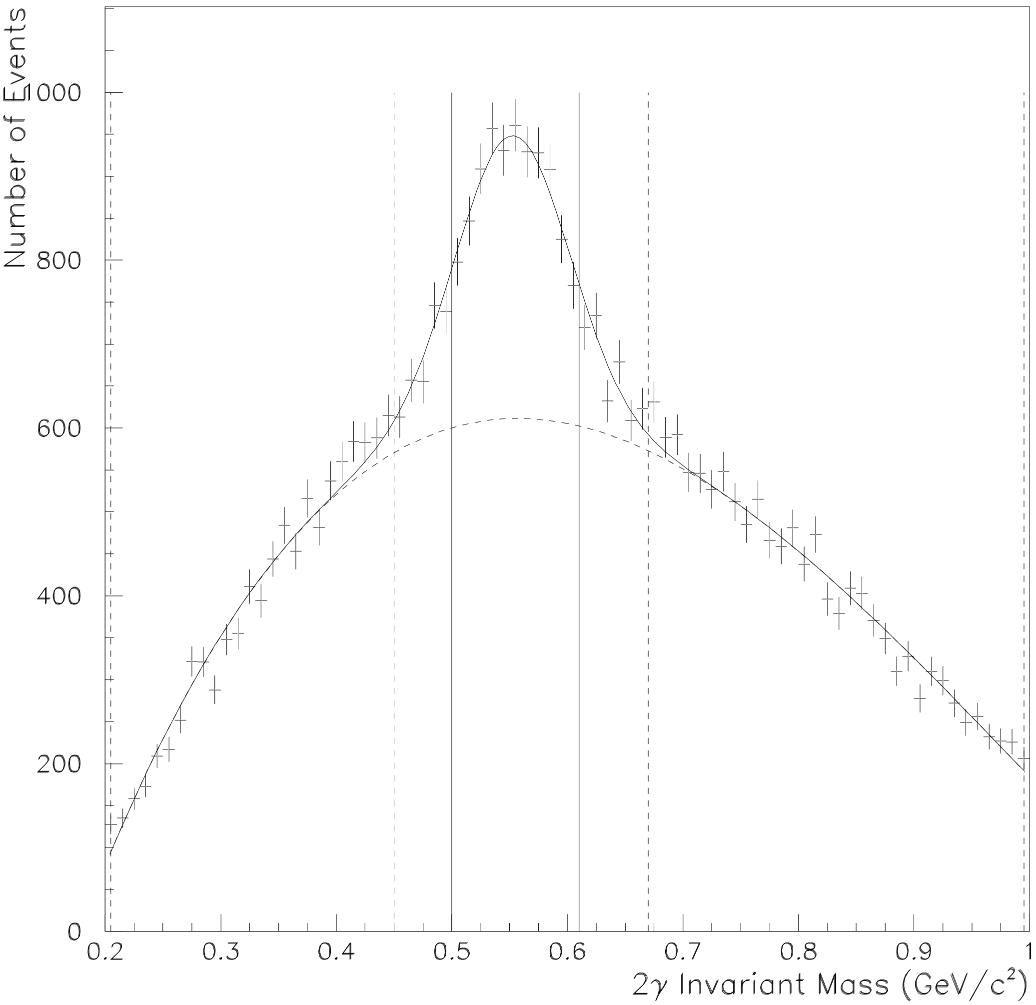

Figure 6.6: The measured 2 γ mass distribution. The solid curve shows the signal plus background fit, and the dashed curve is the background fit. The solid vertical lines indicate the background region and the dashed lines show the two background regions.

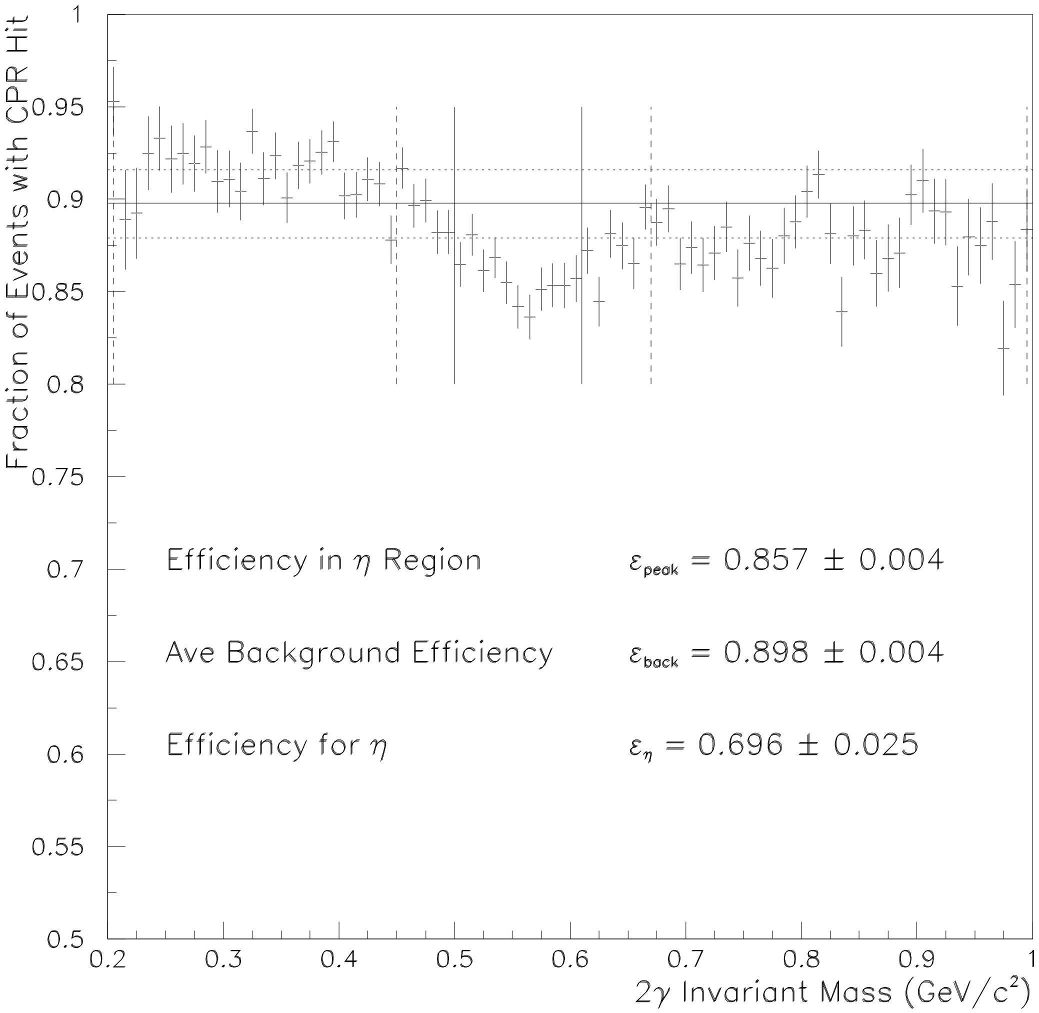

Figure 6.7: The measured CPR hit rate efficiency. The solid vertical lines indicate the signal region and the dashed vertical lines indicate the background regions. The average efficiency in the peak region is 0.857 ± 0.004. The background efficiency is 0.916 ± 0.003 in the low mass region and 0.879± 0.003 in the high mass region, which are shown by the dotted lines. The average of the two values is indicated by the solid horizontal line. A background subtraction using the average background value gives an efficiency of 0.696 ± 0.025.

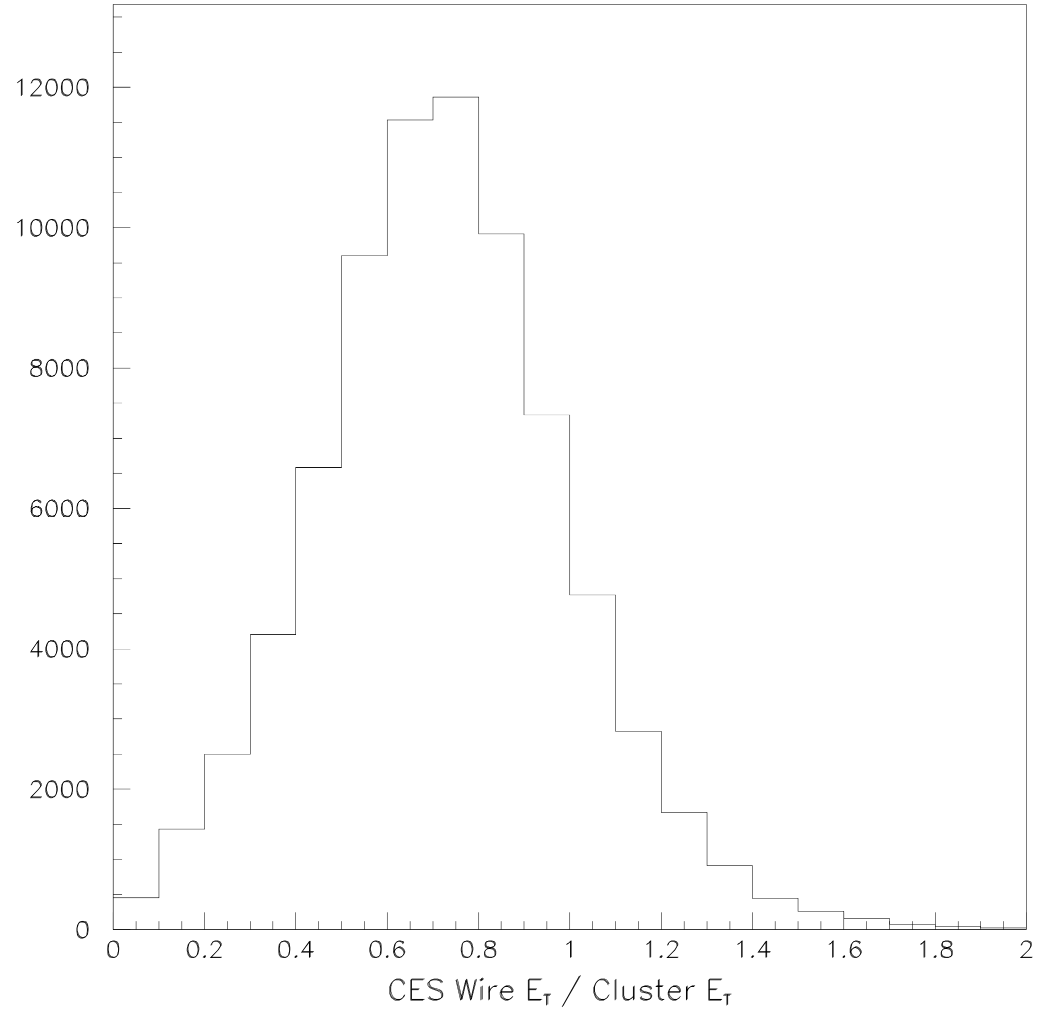

Figure 6.8: The ratio of the CES wire E_T versus the electromagnetic cluster E_T. The ratio peaks at 0.75, which is the amount of the second CES strip and wire energies should be correction.

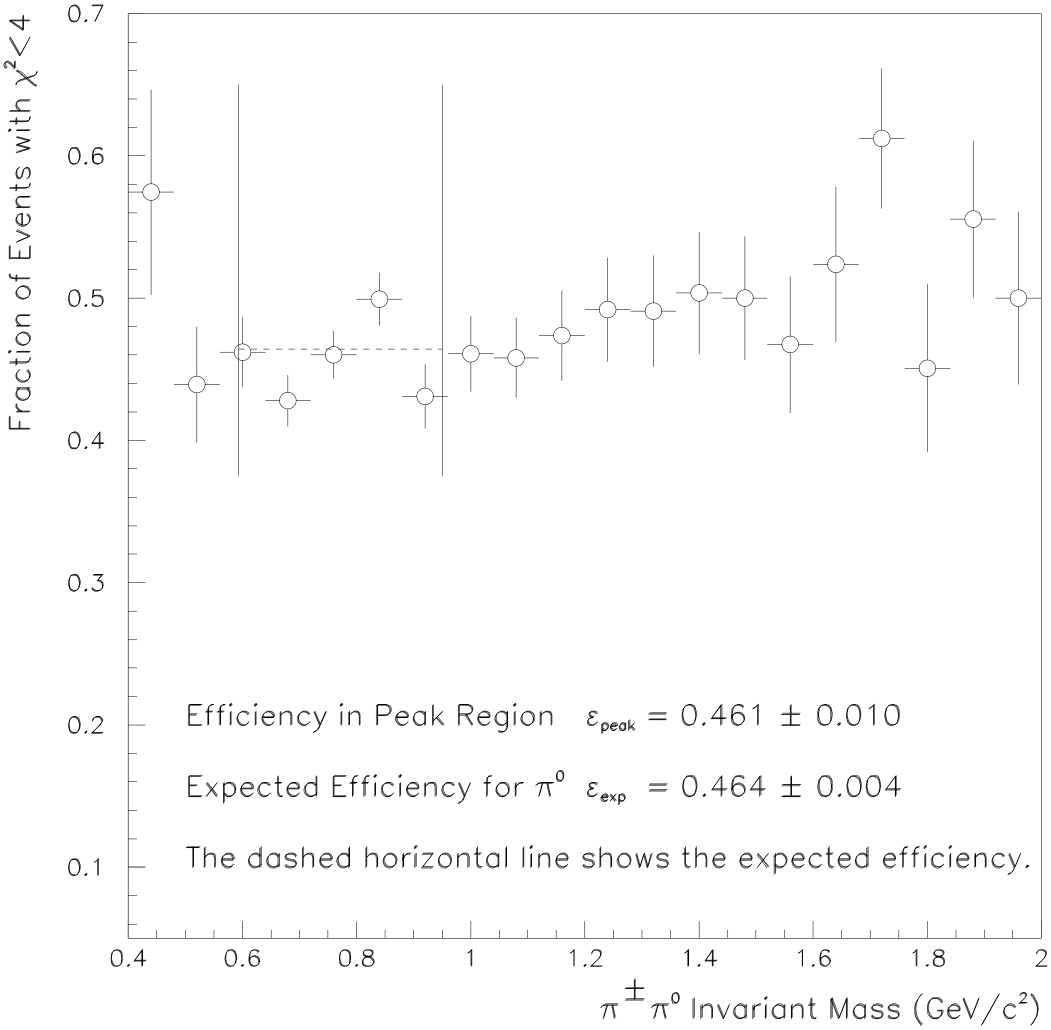

Figure 6.9: The measured CES efficiency (fraction of events with $\chi^2 < 4$ out of all events with $\chi^2 < 20$) after the CES energy corrections and Z_{vertex} cut were applied. The solid vertical lines on the plot indicate the signal region. The dashed horizontal line indicates the expected efficiency from QFL. The peak efficiency is the average efficiency between the vertical lines. The measured and expected efficiencies are consistent with each other.

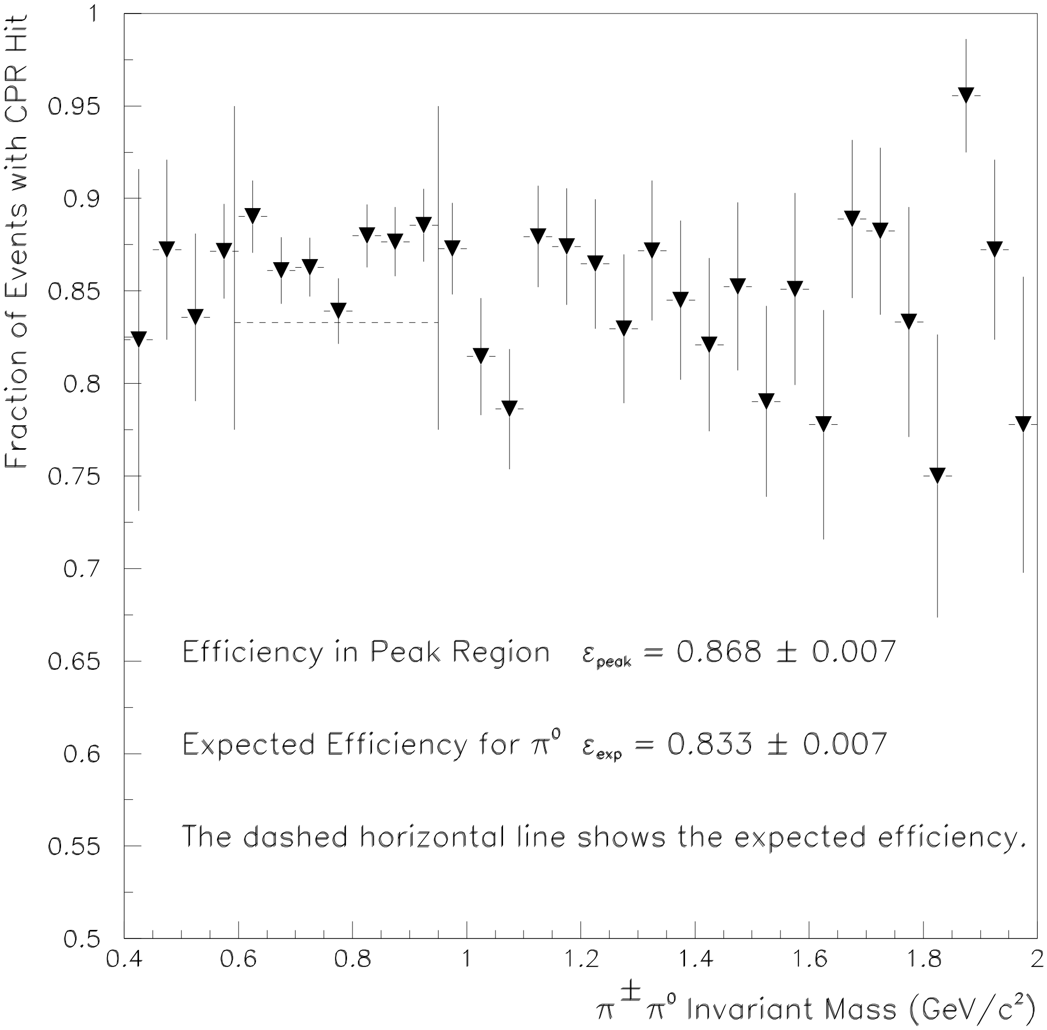

Figure 6.10: The measured CPR hit rate efficiency (fraction of events with CPR hit $>$ 500 fc out of all events) after the CES energy corrections and Z_{vertex} cut were applied. The solid vertical lines on the plot indicate the the signal region. The dashed horizontal line indicates the expected efficiency. The peak efficiency is the average efficiency between the vertical lines. The agreement between the measured and expected efficiencies was not improved.

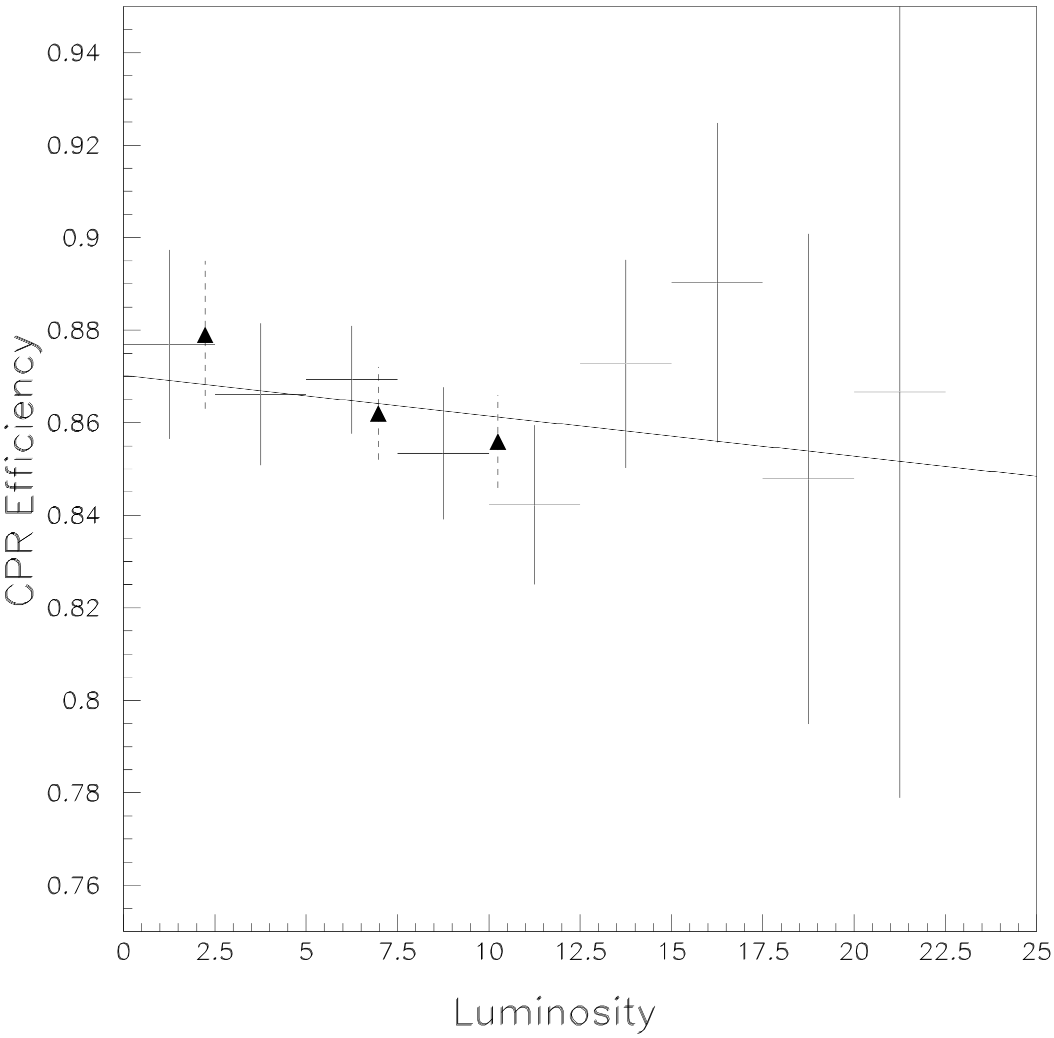

Figure 6.11: CPR efficiencies as a function of luminosity. The triangles show the average efficiency for the three groups of runs plotted at the average luminosity for each group.

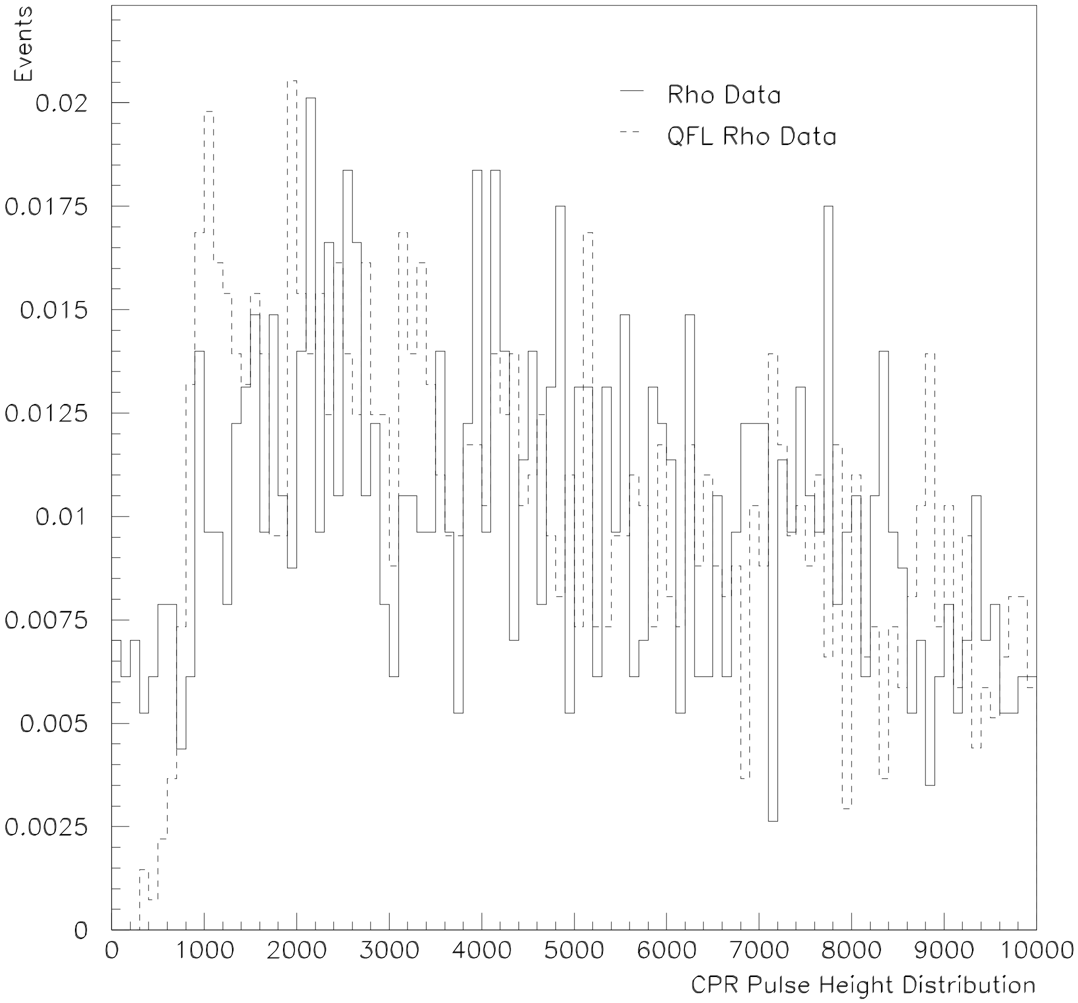

Figure 6.12: CPR pulse height distribution for the rho data and a QFL rho simulation.

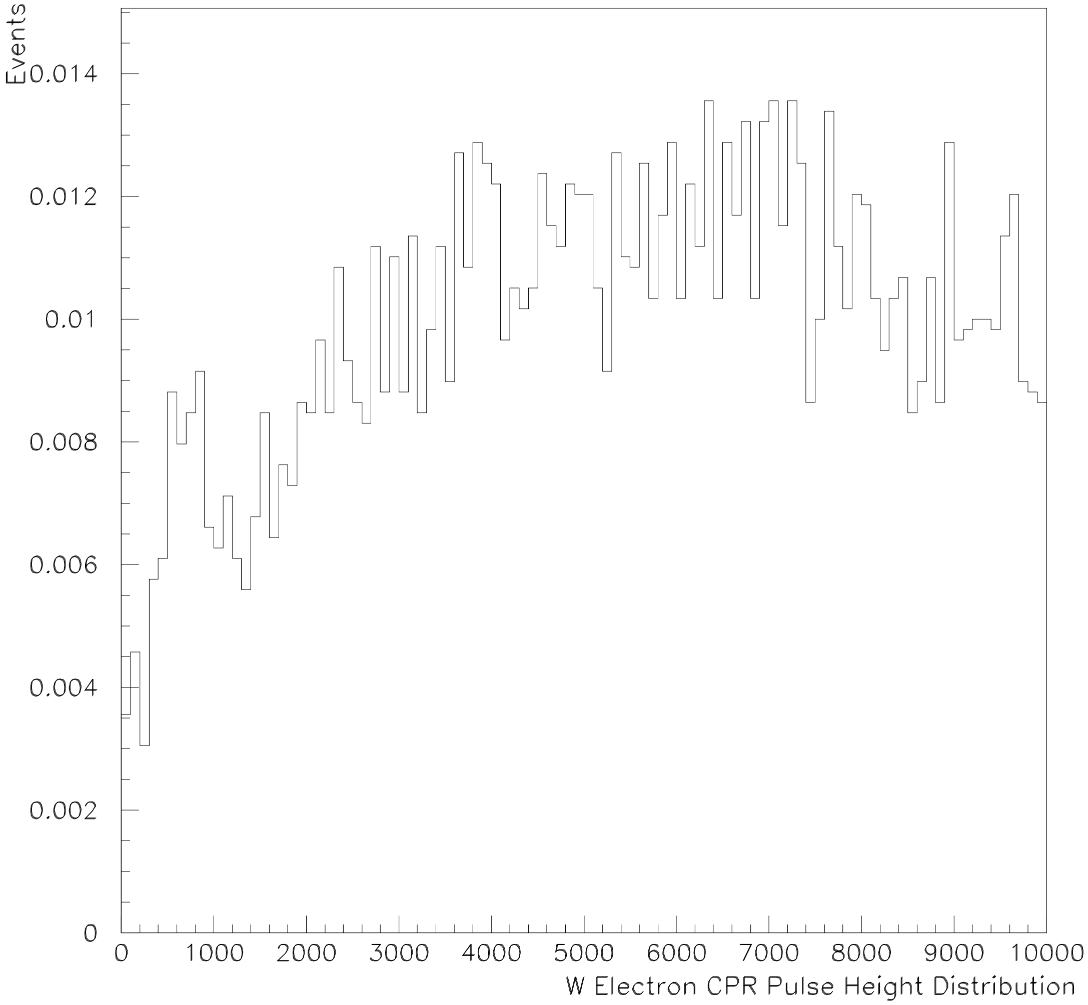

Figure 6.13: CPR pulse height distribution for electrons from W decays.

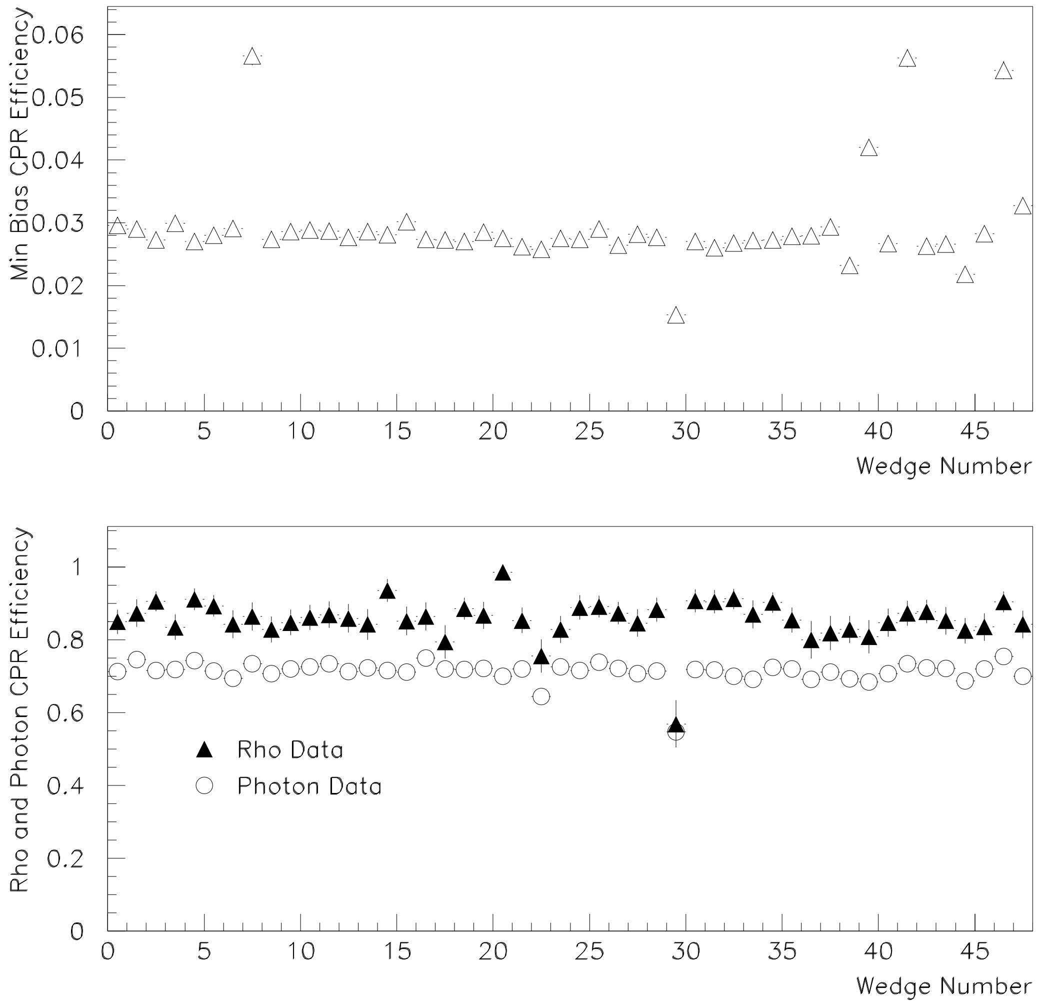

Figure 6.14: The measured CPR hit rate efficiency (fraction of events with a CPR pulse height > 500 fc of all events) as a function of the calorimeter wedge number from the minimum bias, rho, and photon data samples.

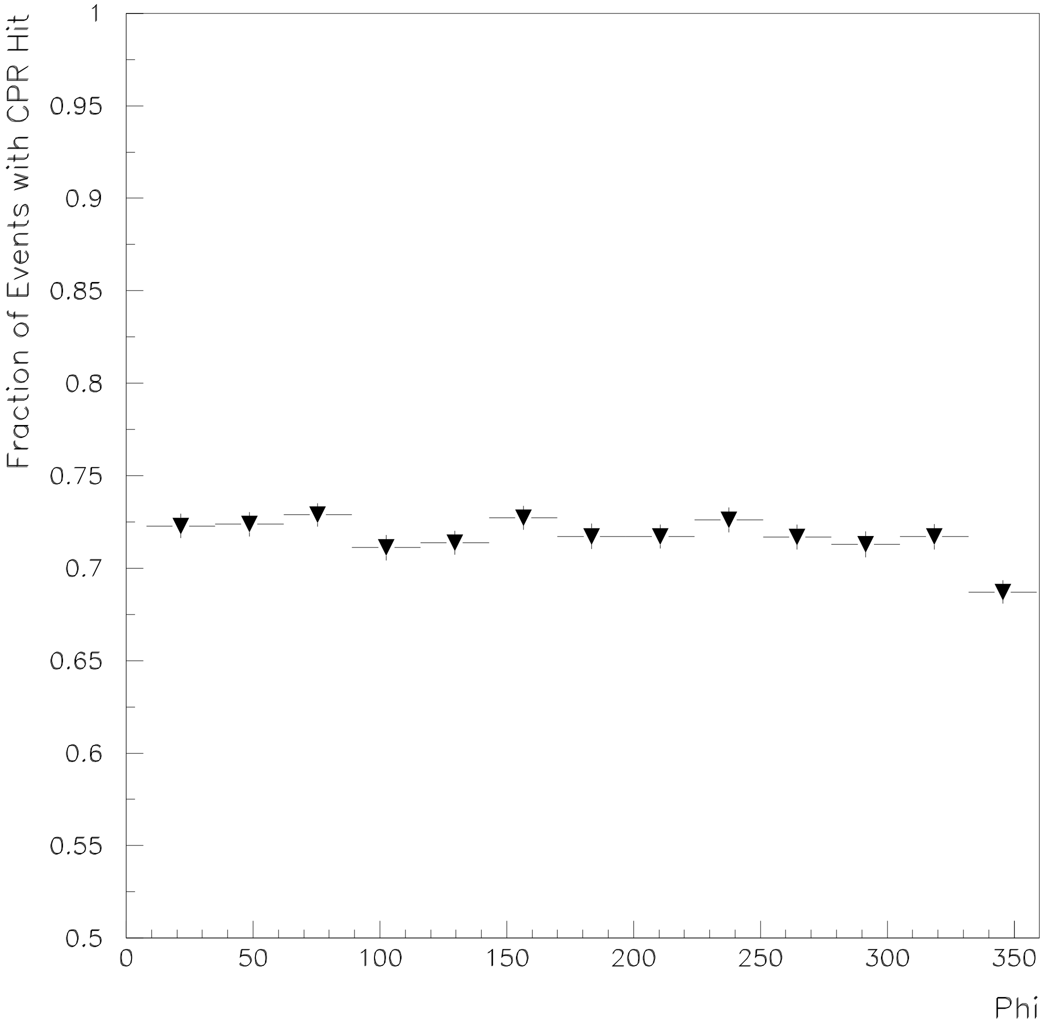

Figure 6.15: The measured CPR hit rate efficiency (fraction of events with a CPR pulse height of 500 fc of all events) as a function of ϕ for the West half of the detector. The Time Of Flight detector component added an additional 0.1 X_0 to the amount of material in front of the CPR in the range $197^\circ < \phi < 224^\circ$, but it did not affect the CPR hit rate.

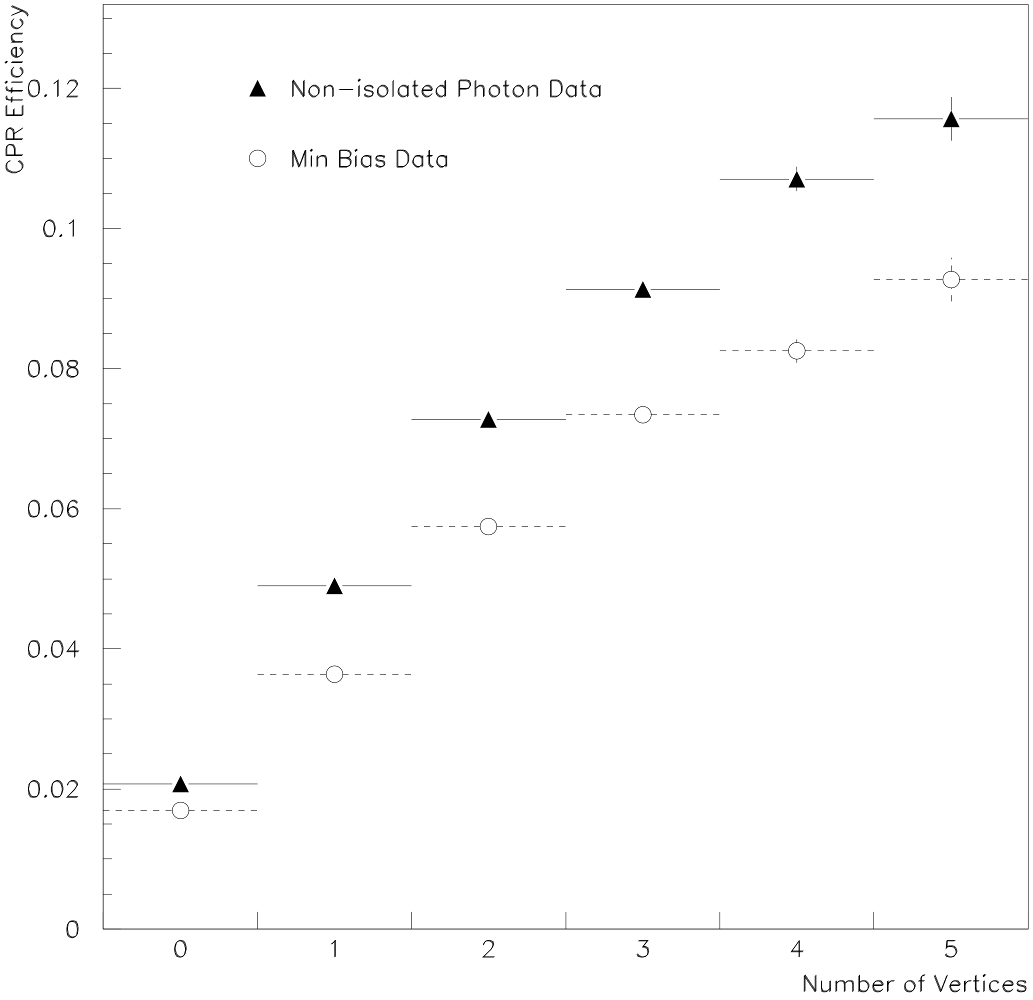

Figure 6.16: The measured CPR hit rate efficiency (fraction of events with a CPR pulse height > 500 fc of all events) as a function of the number of class 12 vertices in the event from the Run 1b minimum bias and non-isolated photon data samples.

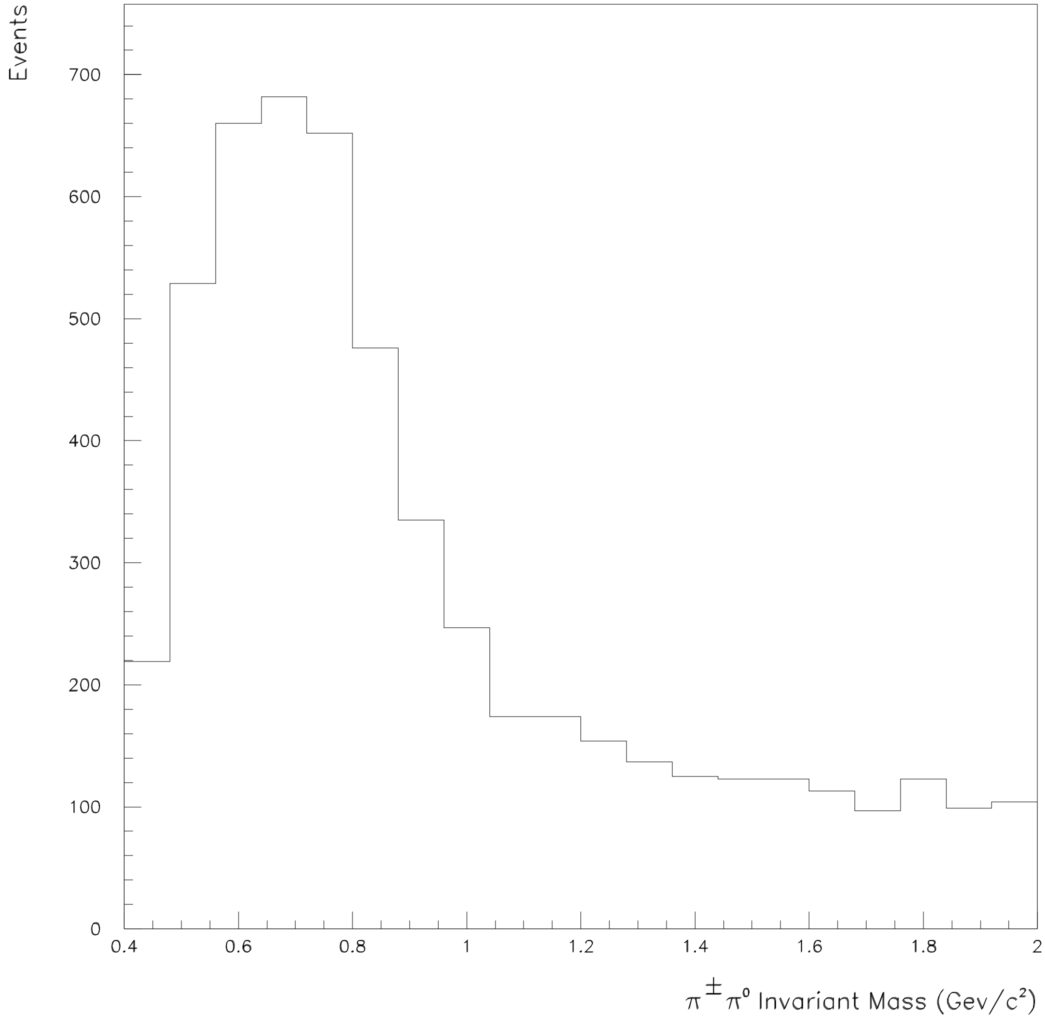

Figure 6.17: The measured $\pi^{\pm}\pi^{0}$ mass distribution from the 630 GeV data.

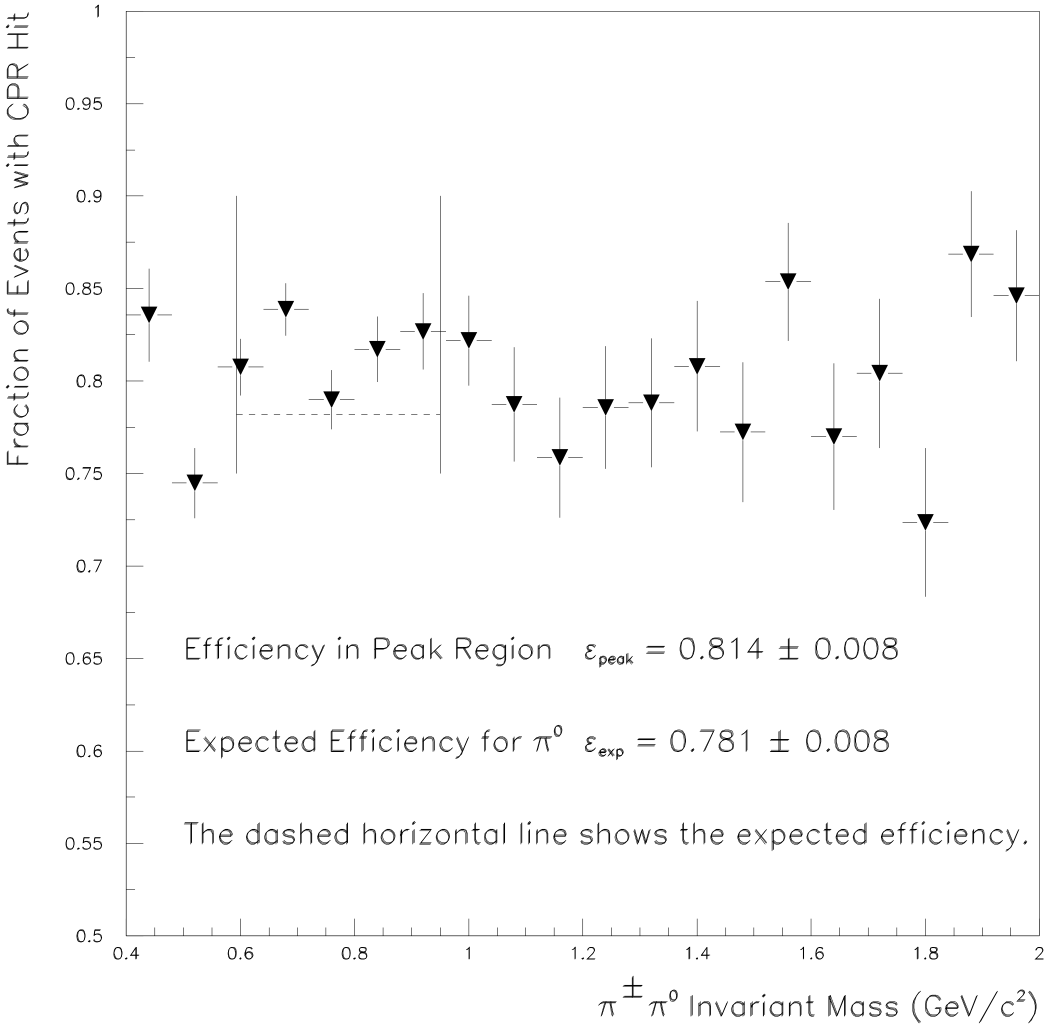

Figure 6.18: The measured CPR hit rate efficiency (fraction of events with CPR hit > 500 fc out of all events). The solid vertical lines on the plot indicate the the signal region. The dashed horizontal line indicates the expected efficiency. The peak efficiency is the average efficiency between the vertical lines.

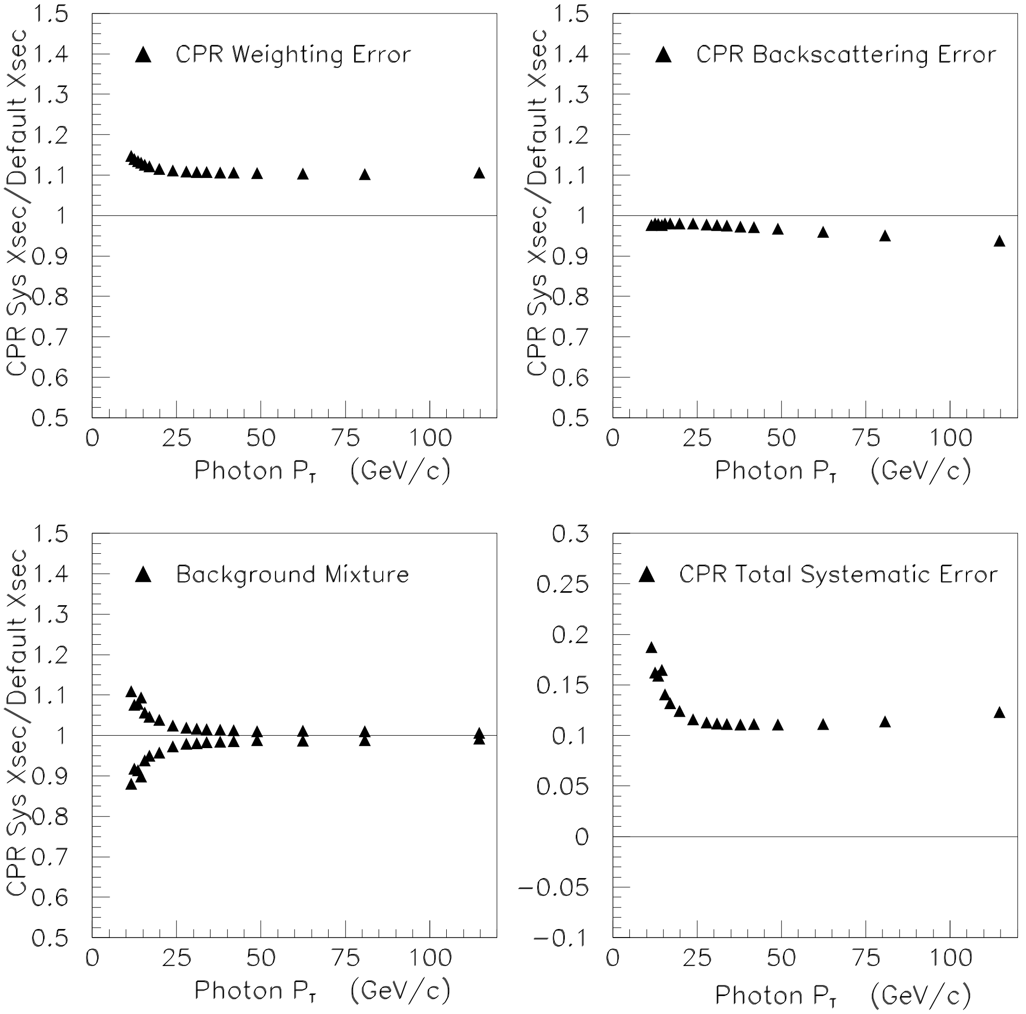

Figure 6.19: The Run 1b CPR systematics from the various sources of error. The first three plots contain the ratio the default and adjusted cross sections. The total error is the quadrature sum of the three sources of error.

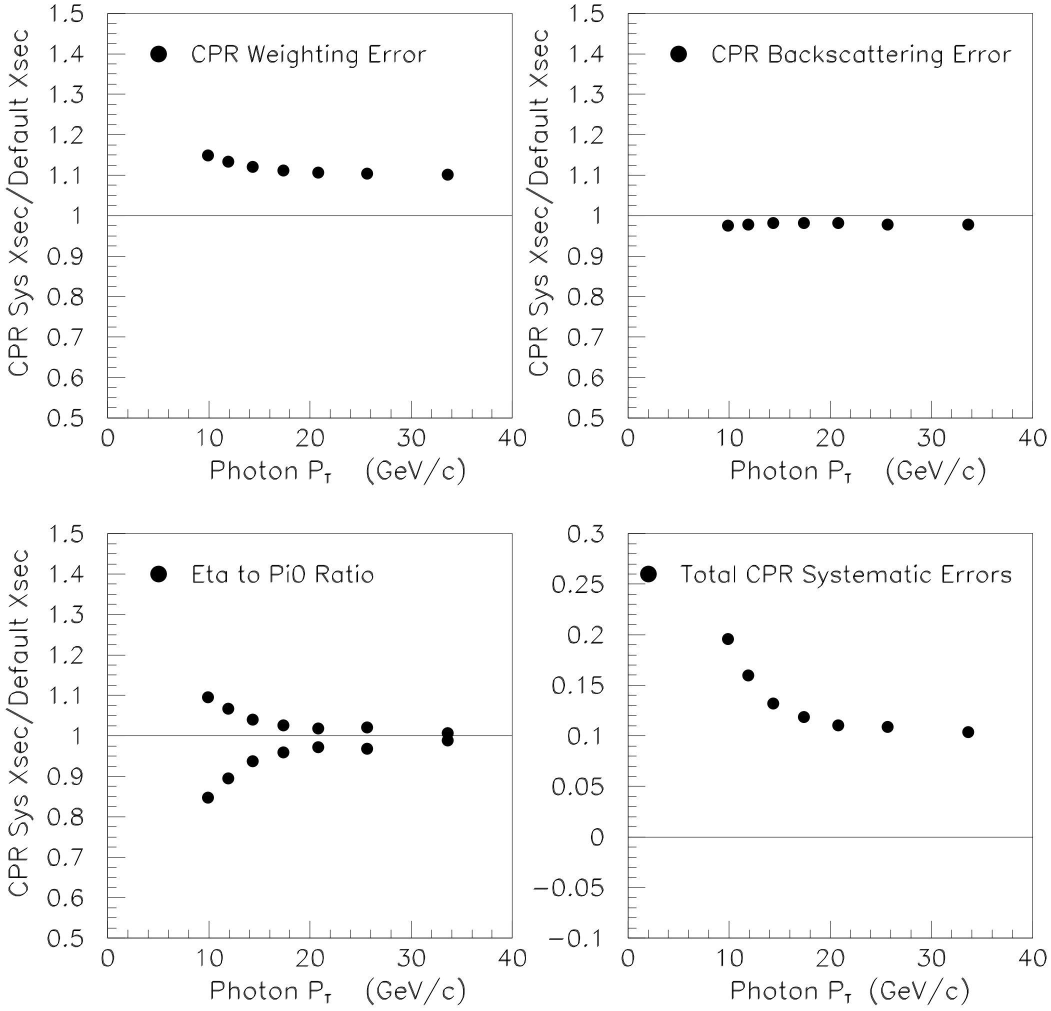

Figure 6.20: The 630 GeV CPR systematics from the various sources of error. The first three plots contain the ratio of the default and adjusted cross sections. The total error is the quadrature sum of the three sources of error.

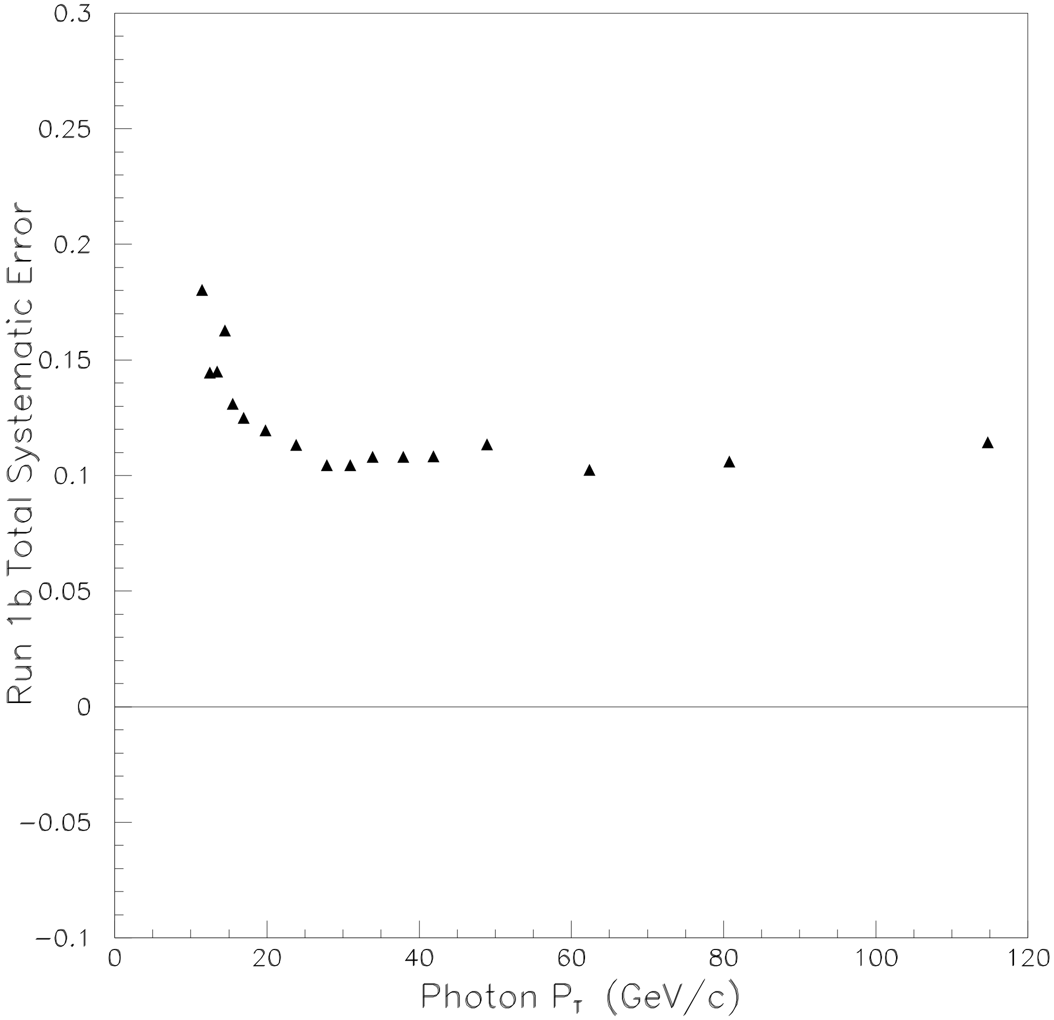

Figure 6.21: The Run 1b total systematic error.

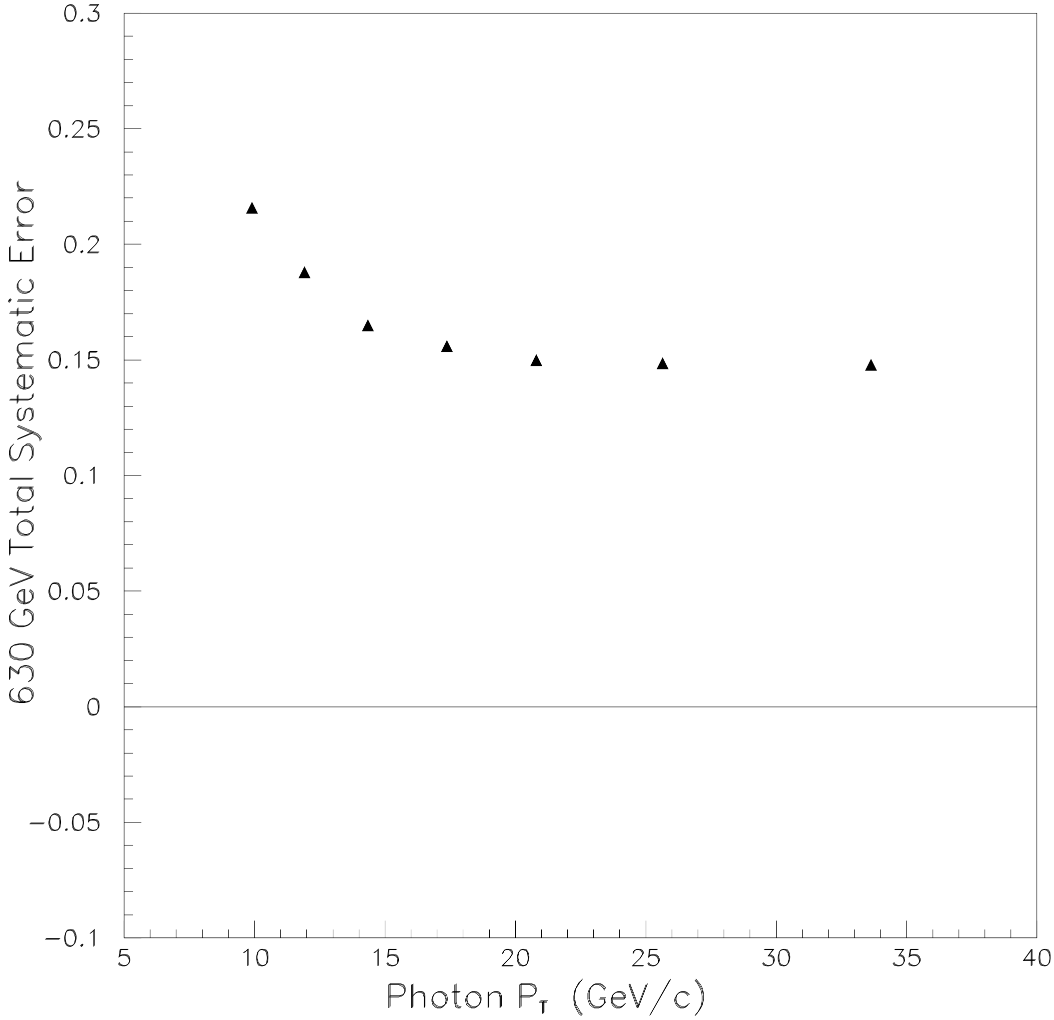

Figure 6.22: The 630 GeV total systematic error.

Chapter 7

Direct Photon Cross Section

At this point, from the number of prompt photons(N_γ) in a bin of transverse momentum (ΔP_T) and a range of pseudorapidity ($\Delta\eta$), along with the acceptance (a) for that bin and the integrated luminosity (L), we can obtain the isolated prompt photon cross section:

$$\frac{d^2\sigma}{dP_T d\eta} = \frac{N_\gamma}{\Delta P_T \Delta\eta a L} \tag{7.1}$$

The cross section is averaged over the pseudorapidity interval $|\eta| < 0.9$ ($\Delta\eta = 1.8$). The results are shown in Tables 7.1 and 7.2

While the CES method has better resolution at low P_T than the CPR method does, we chose to use the CPR method at all P_T in order to simplify the analysis. Before this was done, we checked to be sure that the two methods agreed as they were expected. The results are shown in Figs. 7.1 and 7.2. It is clear that the two methods agree within their systematic errors. The resulting cross sections are shown in 7.3.

Figure 7.4 shows a comparison of the Run 1a (the data taken at CDF during the 1992-1993 Run [24]) and 1b inclusive cross sections with CTEQ2M, the latest theory available when the 1a analysis was published. The two data sets used different isolation cuts (Run 1a had the isolation requirement energy in a cone of radius

0.7 less than 2 GeV) so each data set had to be compared to a theory with the appropriate isolation cut. The 1a and 1b cross sections are consistent with each other. There is good agreement between data and theory at high P_T and an excess of events at low P_T, which is consistent with the need for a k_T correction.

Figure 7.5 shows how the theory by Owens et al has changed since the 1a analysis was published [36]. The plot shows that changing the isolation cut changes the normalization by about 10%. Lowering the energy at which an event is considered to be a 2→3 body interaction instead of a 2→2 body interaction changes the normalization scale by approximately 5%. Finally, going from CTEQ2M to CTEQ4M changes the slope by 15 %. Figure 7.6 compares the 1b data to newer versions of the theories by Owens et al. The plot indicates that the theory with a higher energy scale is in better agreement with the data.

Vogelsang et al has also released new theories since the 1a analysis was published [37]. The differences between his theory curves and those by Owens are that he calculates the NLO fragmentation and allows the energy scales of the renormalization, factorization, and fragmentation parameters to move independently of each other. Figures 7.7 and 7.8 show how the theory has evolved and how it compares to the 1b data. Their latest theory is shown in Fig. 7.9. It has the normalization scale about right, but it still does not adequately predict the slope of the data.

CDF is one of only two experiments that has measured the photon cross section at two vastly different center of mass energies. That makes a comparison of the two cross sections extremely important. Any difference between the two cross sections cannot be the result of detector effects, which can be the case when the results of two different experiments are compared. Figure 7.10 shows a comparison of the Run 1b and 630 GeV cross sections as a function of photon P_T. The two cross sections are consistent with each other within the systematic errors. This is not the case, however, when the data sets are plotted as a function of photon x_T as shown in

Fig. 7.11. When the two cross sections are plotted as a function of photon x_T, any dependance on the choice of parton distribution function should cancel. It is not possible to bring the two cross sections into agreement by changing the PDF. Therefore, the theories need something along the lines of a k_T correction to fix this discrepancy.

Figure 7.12 shows a comparison of the Run 1b data to CTEQ5M by Vogelsang et al with the addition of a 4 GeV k_T correction and a parton shower correction. The data was multiplied by 1.25 in order to do a shape comparison more easily. The overall normalization is off by 25%, but the parton shower algorithm is the best predictor of the shape. Figure 7.13 shows a comparison of the 630 GeV photon cross section to CTEQ5M with a 3 GeV k_T correction and with the parton shower algorithm. For the 630 GeV data the k_T corrections predicts the shape better than the parton shower algorithm.

The CDF data sets can be compared to other the results of other experiments at the same energy. The experiment whose results should be the most similar to CDF is D0 [38]. The D0 experiment is located across the ring from CDF so it took data at the same time as CDF. The D0 detector is fairly similar to the CDF detector. The main differences between the CDF and D0 detectors that affect the photon measurements are: the lack of a magnetic field in its tracking chamber, the lack of an equivalent to the CPR chambers, and a more finely segmented calorimeter. At this time they have only published their Run 1b photon cross section. A comparison of the results is shown in Fig. 7.14. The data sets are consistent with each other, but CDF clearly has the advantage at low P_T.

D0's 630 GeV data has not yet been made public and is therefore not available for comparison. Therefore, we compared our 630 GeV data to UA2's results in Fig.7.15 [30]. Again, the two data are consistent with each other.

<table>
<tr><th colspan="7">$\sqrt{s} = 1.8$TeV</th></tr>
<tr><th>P_T</th><th># Events</th><th># Photons</th><th>$d^2\sigma/dP_T d\eta$</th><th>Stat.</th><th>Sys.</th><th>NLO QCD</th></tr>
<tr><th>(GeV/c)</th><th></th><th></th><th>(pb/(GeV/c))</th><th>(%)</th><th>(%)</th><th>(pb/(GeV/c))</th></tr>
<tr><td>11.5</td><td>13818</td><td>3839</td><td>8.84×10^3</td><td>9.0</td><td>18.0</td><td>7.36×10^3</td></tr>
<tr><td>12.5</td><td>12809</td><td>4437</td><td>7.89×10^3</td><td>8.5</td><td>14.4</td><td>5.21×10^3</td></tr>
<tr><td>13.5</td><td>9304</td><td>3074</td><td>4.50×10^3</td><td>10.0</td><td>14.5</td><td>3.77×10^3</td></tr>
<tr><td>14.5</td><td>6173</td><td>1772</td><td>2.61×10^3</td><td>9.3</td><td>16.3</td><td>2.78×10^3</td></tr>
<tr><td>15.5</td><td>4150</td><td>1626</td><td>2.40×10^3</td><td>8.4</td><td>12.1</td><td>2.09×10^3</td></tr>
<tr><td>17.0</td><td>4993</td><td>2173</td><td>1.61×10^3</td><td>6.8</td><td>12.5</td><td>1.43×10^3</td></tr>
<tr><td>19.8</td><td>4133</td><td>1945</td><td>7.38×10^2</td><td>6.7</td><td>12.0</td><td>7.26×10^2</td></tr>
<tr><td>23.8</td><td>1410</td><td>809</td><td>3.12×10^2</td><td>9.3</td><td>11.3</td><td>3.24×10^2</td></tr>
<tr><td>27.9</td><td>38033</td><td>25226</td><td>1.55×10^2</td><td>3.5</td><td>10.5</td><td>1.63×10^2</td></tr>
<tr><td>31.0</td><td>13283</td><td>9171</td><td>9.64×10^1</td><td>2.6</td><td>10.5</td><td>1.01×10^2</td></tr>
<tr><td>33.9</td><td>16767</td><td>11885</td><td>6.32×10^1</td><td>2.3</td><td>10.8</td><td>6.75×10^1</td></tr>
<tr><td>37.9</td><td>9244</td><td>6750</td><td>3.69×10^1</td><td>3.0</td><td>10.8</td><td>4.06×10^1</td></tr>
<tr><td>41.9</td><td>5467</td><td>4210</td><td>2.33×10^1</td><td>3.7</td><td>10.8</td><td>2.57×10^1</td></tr>
<tr><td>48.9</td><td>6683</td><td>5453</td><td>1.14×10^1</td><td>3.3</td><td>11.3</td><td>1.25×10^1</td></tr>
<tr><td>62.4</td><td>3253</td><td>2376</td><td>3.12×10^0</td><td>4.8</td><td>10.2</td><td>3.96×10^0</td></tr>
<tr><td>80.8</td><td>924</td><td>686</td><td>8.21×10^{-1}</td><td>12.0</td><td>10.6</td><td>1.12×10^0</td></tr>
<tr><td>114.7</td><td>386</td><td>316</td><td>1.43×10^{-1}</td><td>13.0</td><td>11.4</td><td>1.89×10^0</td></tr>
</table>

Table 7.1: The Run 1b photon data. P_T is the average P_T in the bin. The theory from the NLO QCD is CTEQ5M by Vogelsang et al.

$\sqrt{s} = 0.63\text{TeV}$						
P_T	# Events	# Photons	$d^2\sigma/dP_T d\eta$	Stat.	Sys.	NLO QCD
(GeV/c)			(pb/(GeV/c))	(%)	(%)	(pb/(GeV/c))
9.9	26606	6260	7.55×10^3	9.5	21.6	4.71×10^3
11.9	8531	2382	2.90×10^3	8.4	18.8	2.09×10^3
14.3	4048	1532	1.26×10^3	8.5	16.5	9.12×10^2
17.4	1269	590	4.89×10^2	11.9	15.6	3.83×10^2
20.8	550	302	1.92×10^2	15.0	15.0	1.66×10^2
25.7	245	125	5.40×10^1	23.0	14.9	6.11×10^1
33.6	112	84	2.03×10^1	25.2	14.8	1.61×10^1

Table 7.2: The 630 GeV photon data. P_T is the average P_T in the bin. The theory from the NLO QCD is CTEQ5M by Vogelsang et al.

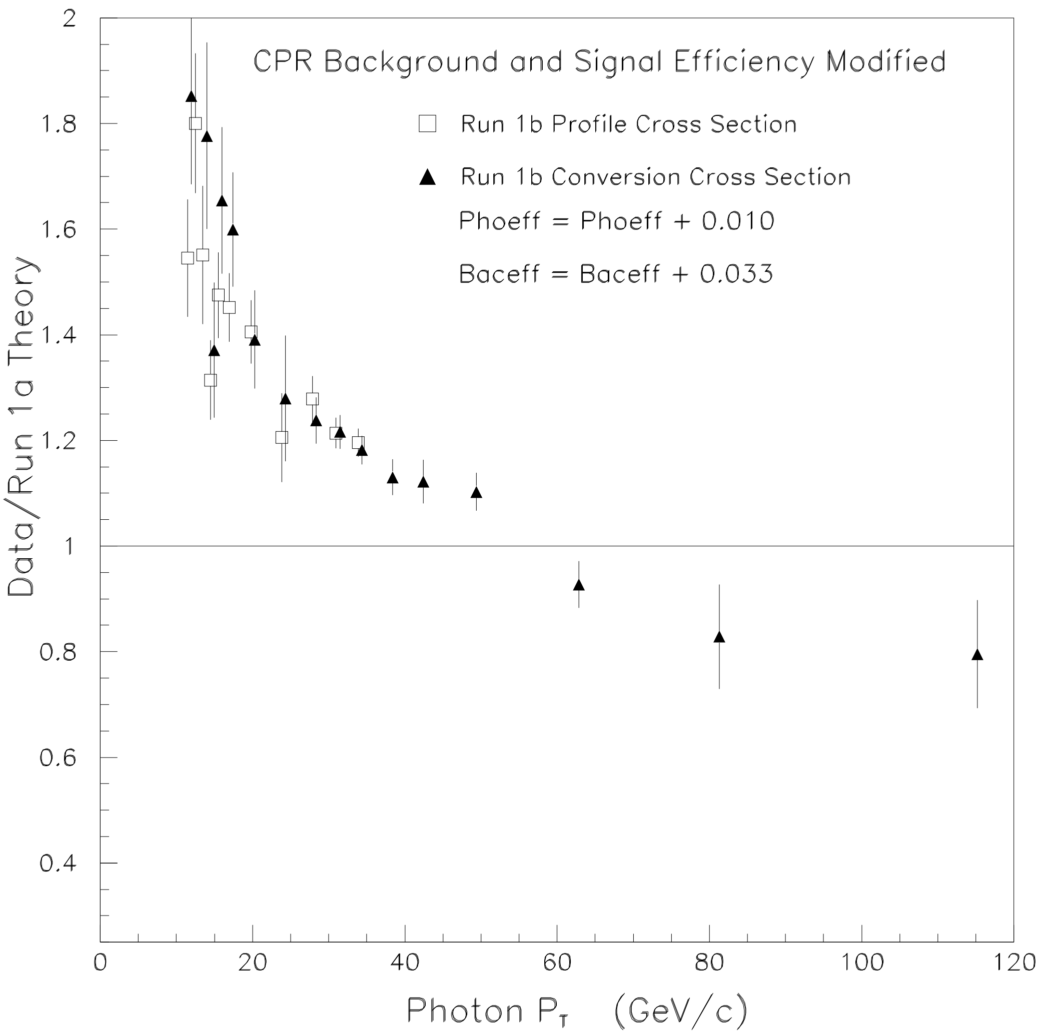

Figure 7.1: A comparison of the Run 1b CES and CPR cross sections after the CPR signal and background efficiencies have been modified with CTEQ2M. The CES and CPR methods agree within the systematic errors.

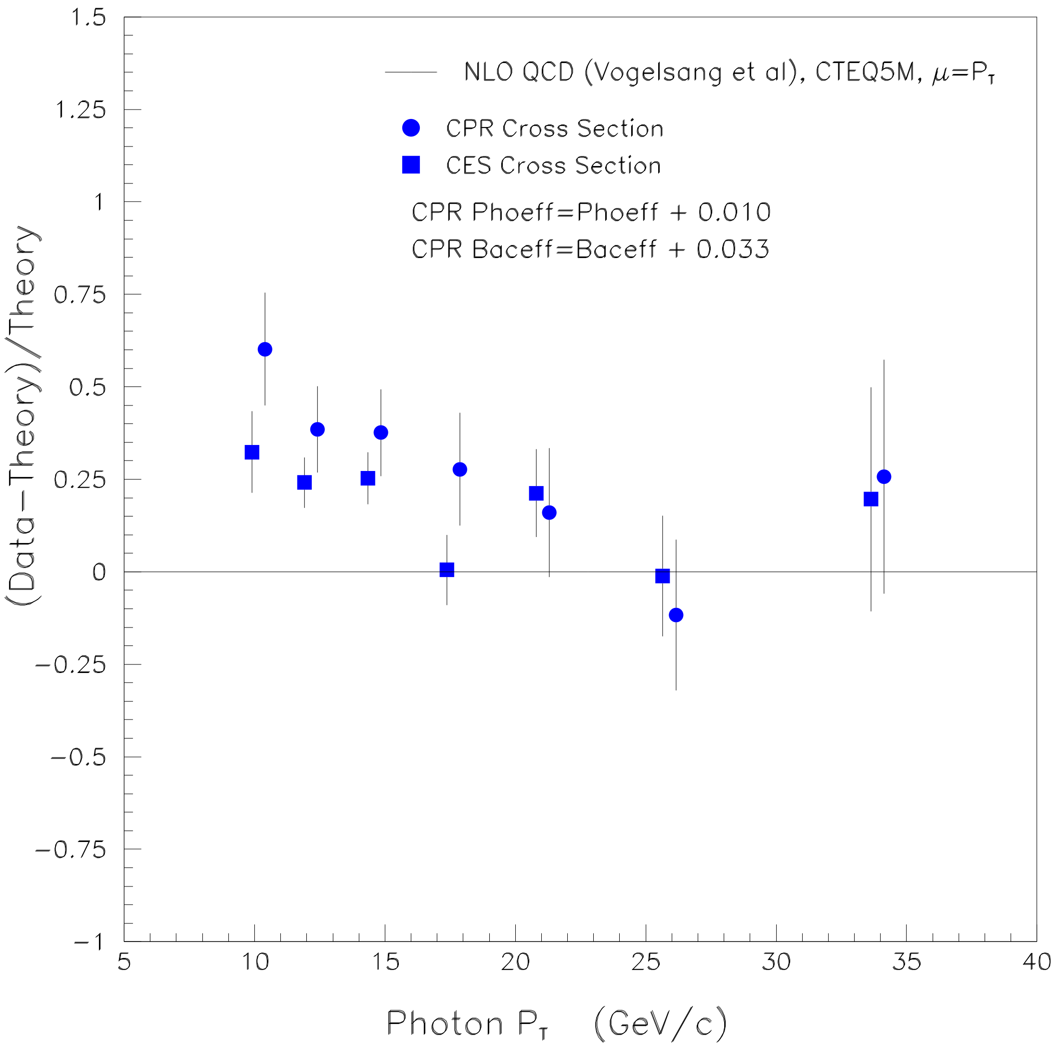

Figure 7.2: A comparison of the 630 GeV CES and CPR cross sections after the CPR signal and background efficiencies have been modified with CTEQ5M (Vogelsang et al). The CES and CPR methods agree within the systematic errors.

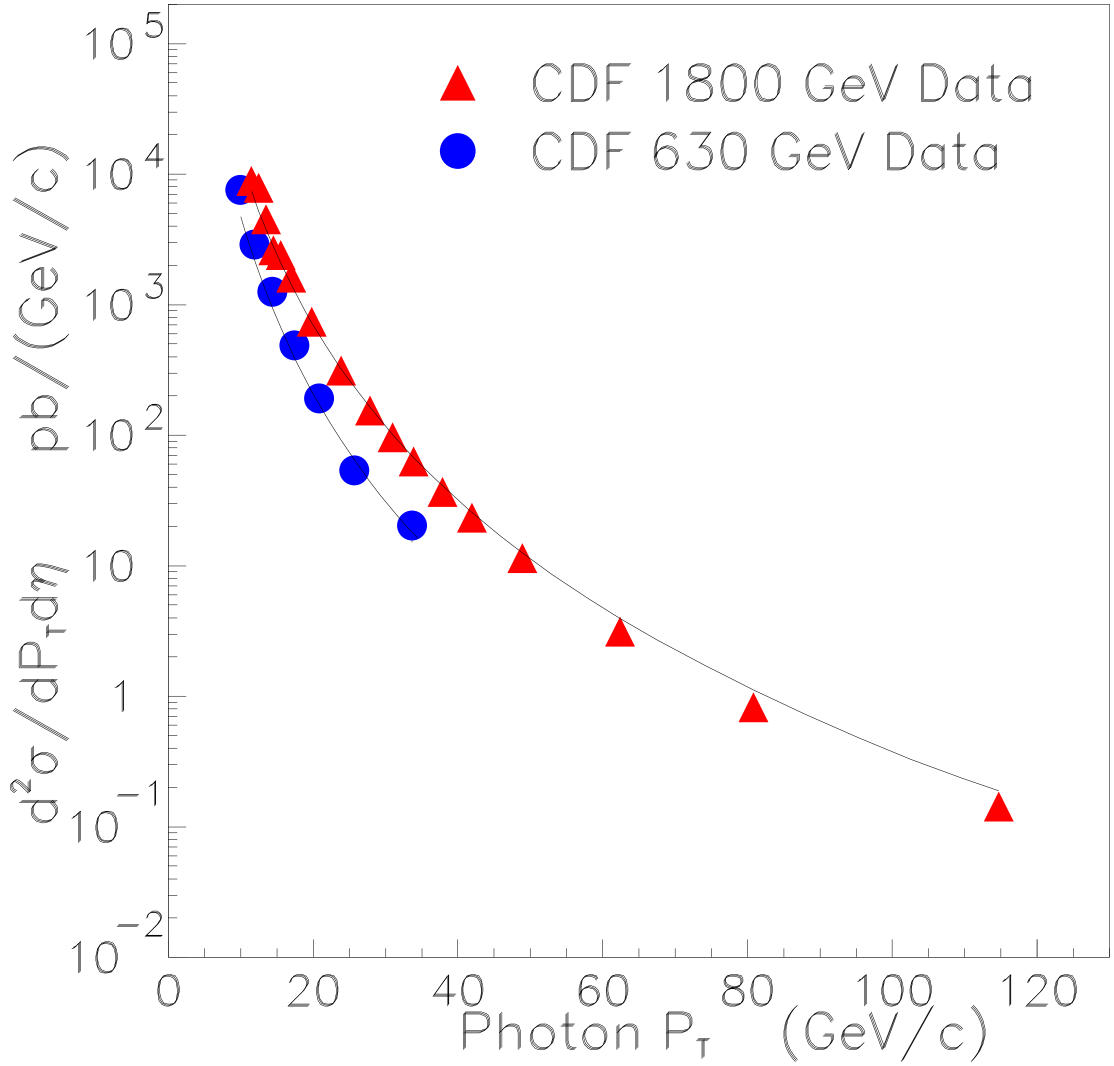

Figure 7.3: The Run 1B and 630 GeV cross sections compared to CTEQ5M (Vogelsang et al).

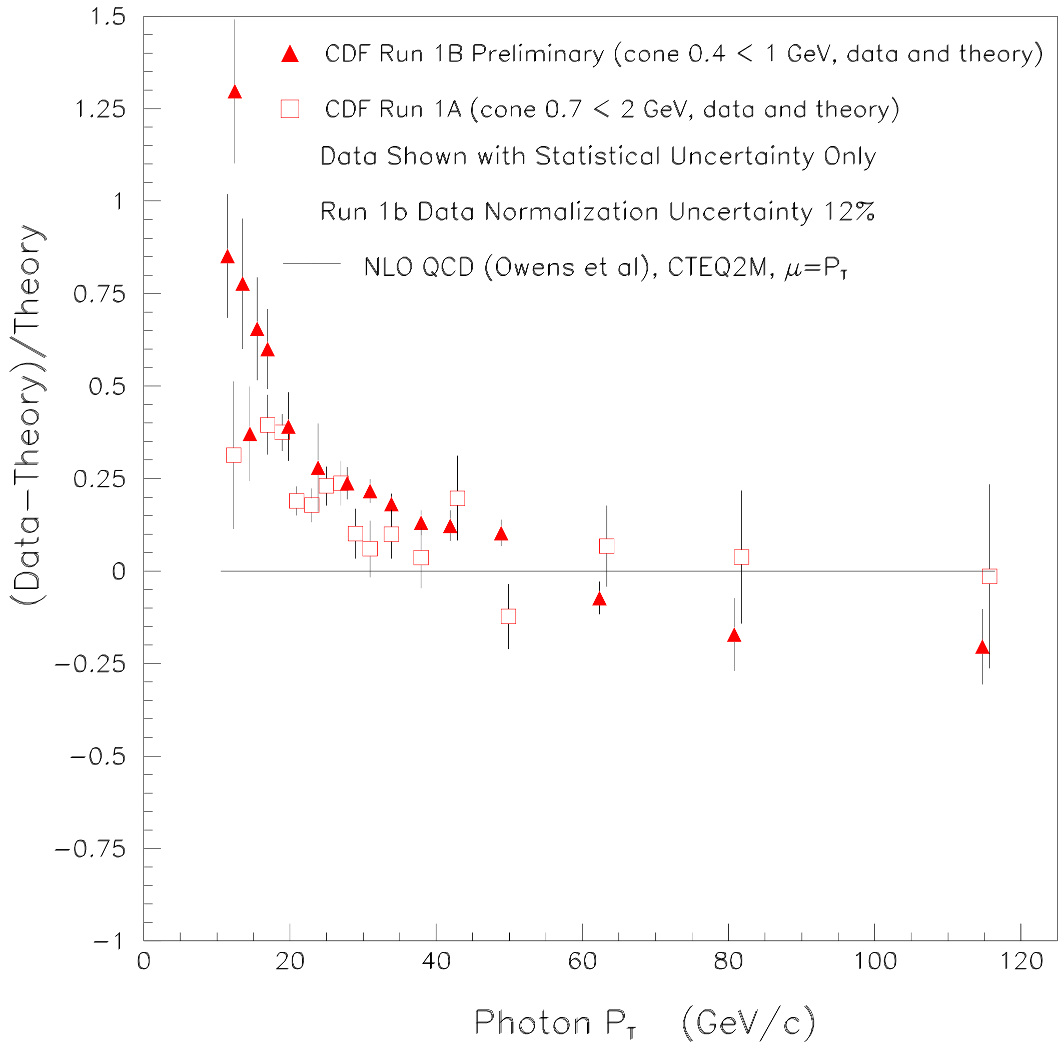

Figure 7.4: The run 1b inclusive photon cross section compared to the run 1a cross section. The two data sets are being compared to the same theory with the appropriate isolation cuts. The last five points from the 1a data have been shifted up by 1 GeV so the error bars on both data sets can be seen.

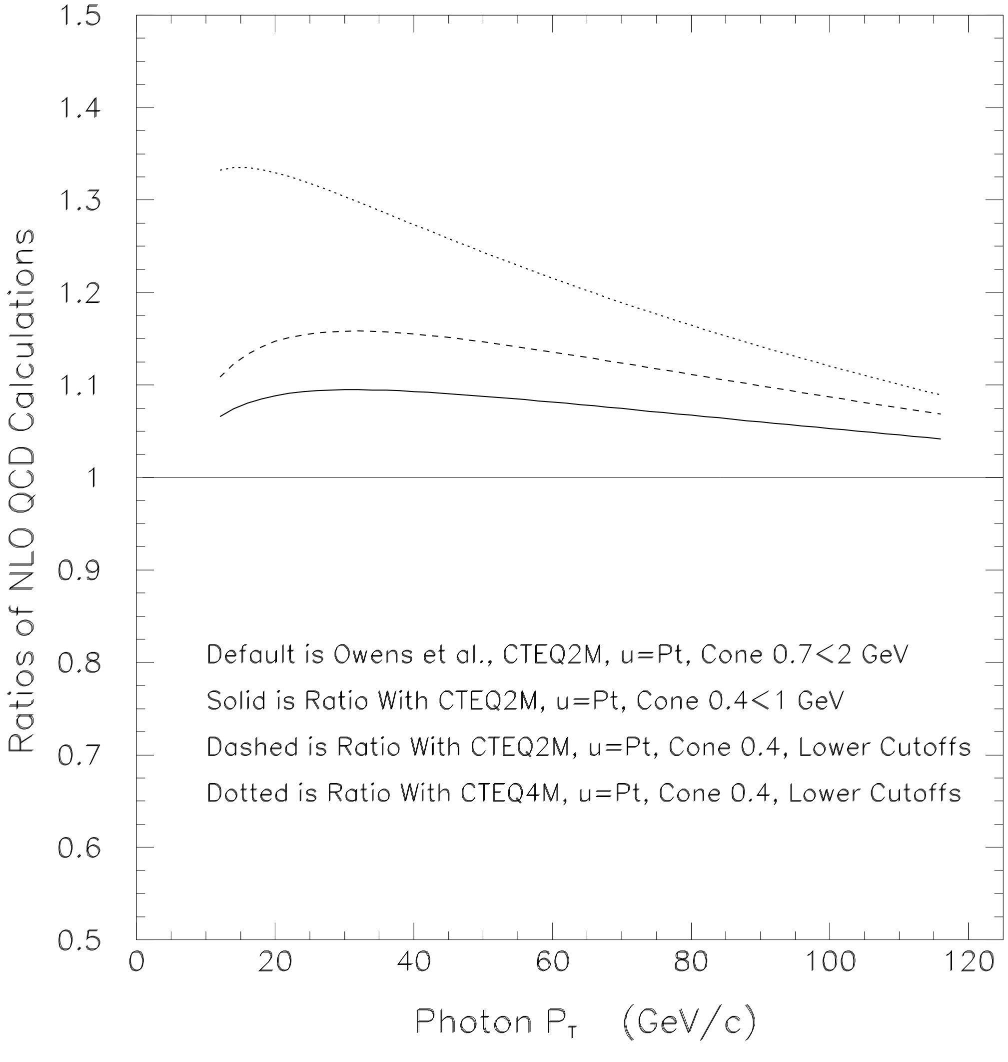

Figure 7.5: The changes in the theory by Owens et al since the 1a analysis was published.

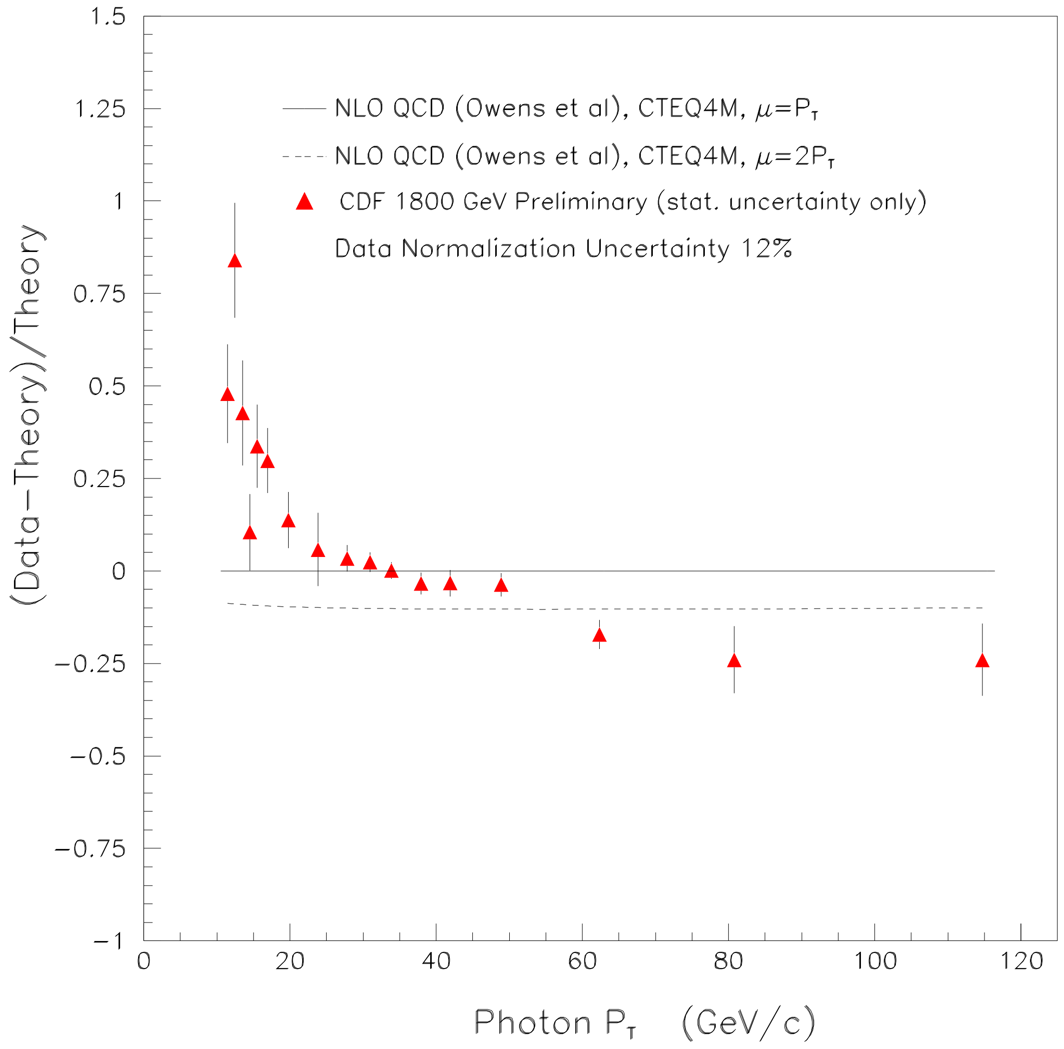

Figure 7.6: The 1b photon cross section compared to the latest theory by Owens et al at two energy scales. The theory with $\mu = 2P_T$ does a better job of describing the data.

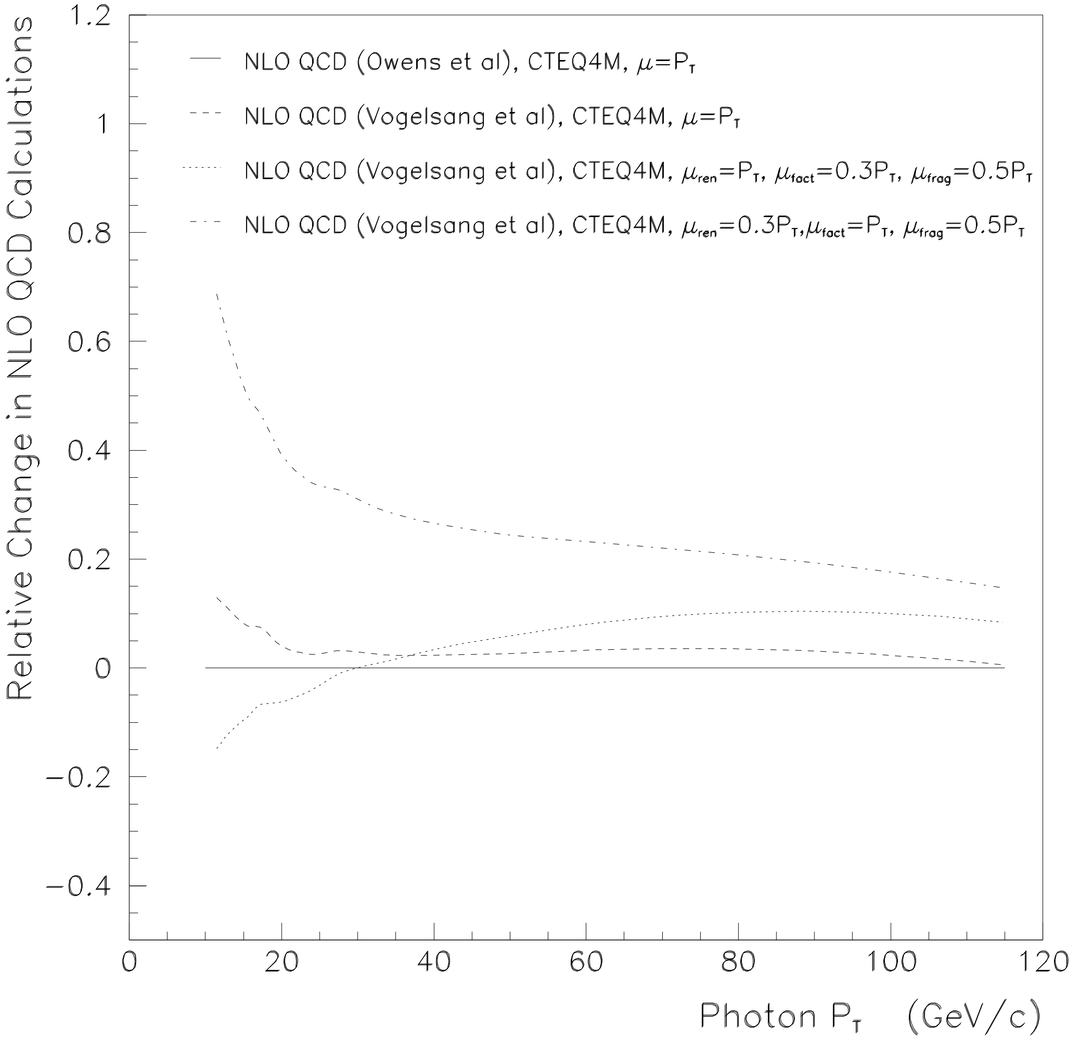

Figure 7.7: Theory curves by Vogelsang et al show how allowing the renormalization, factorization, and fragmentation scales to move independently of each can change the shape of the cross section.

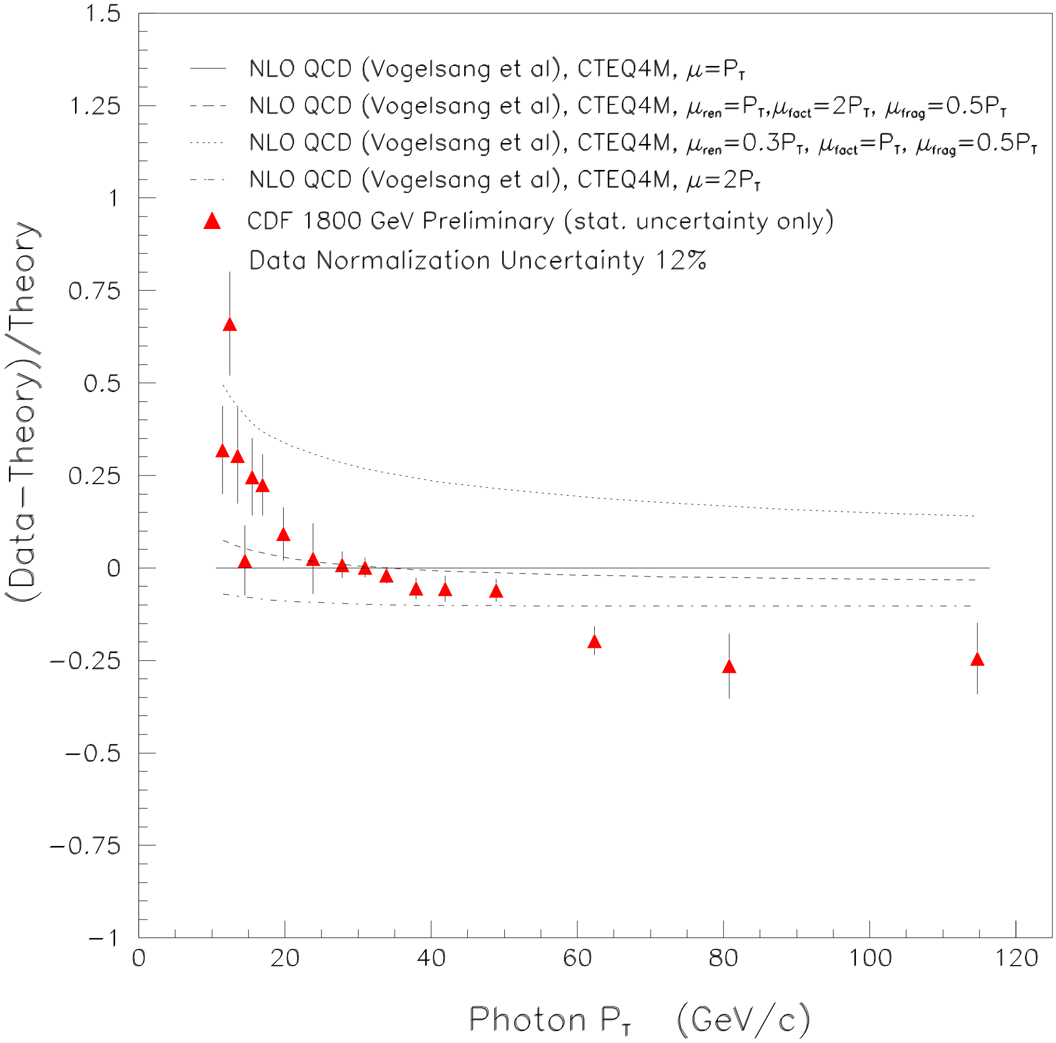

Figure 7.8: A comparison of the 1b data to theories by Vogelsang et al using four different parton distribution functions.

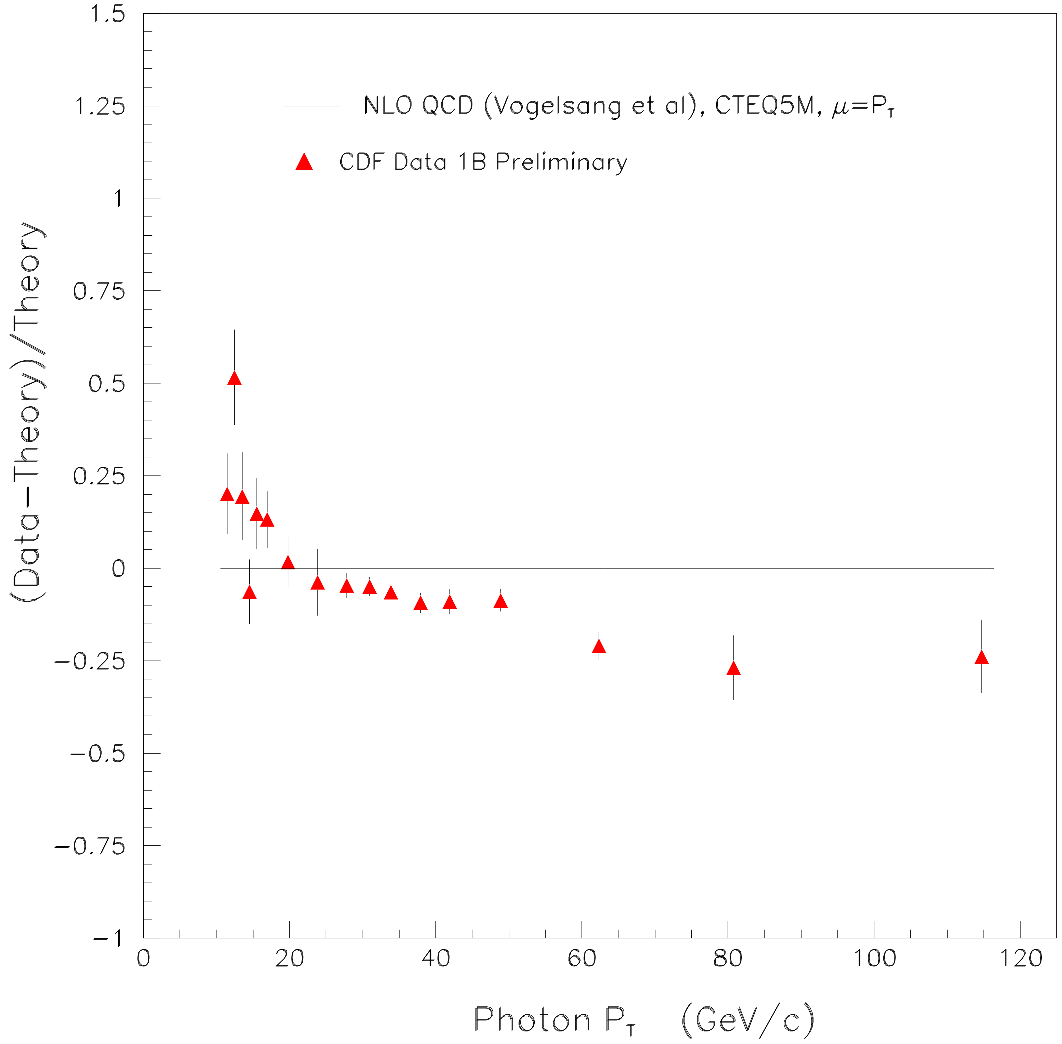

Figure 7.9: A comparison of the 1b data to CTEQ5M by Vogelsang et al. This theory best describes the data but it still does not get the slope of the data correct.

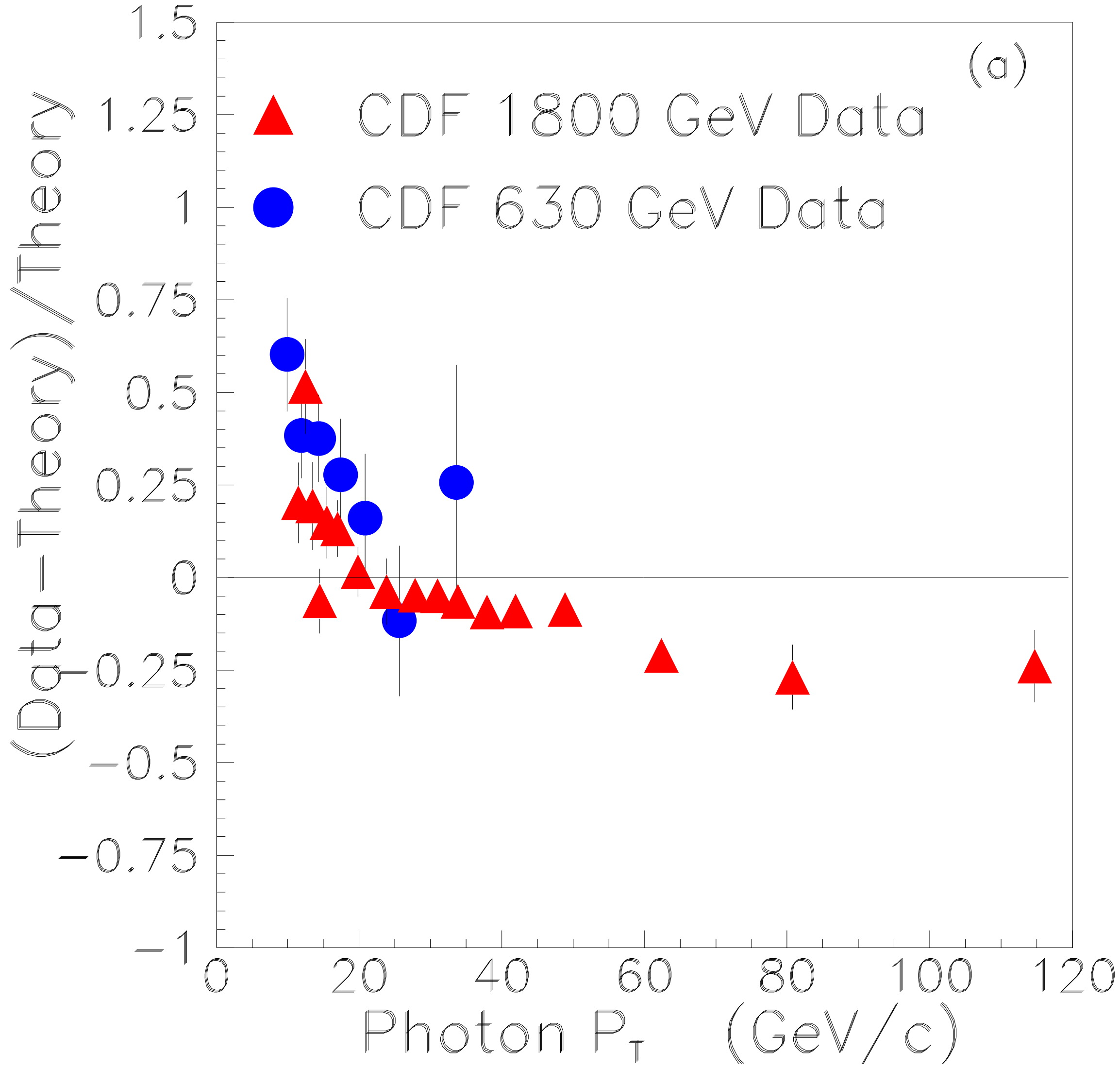

Figure 7.10: A comparison of the Run 1b data and 630 GeV data to CTEQ5M by Vogelsang et al. as a function of photon P_T. The data sets are consistent with each other. The theory does not correctly predict the slope of either data set.

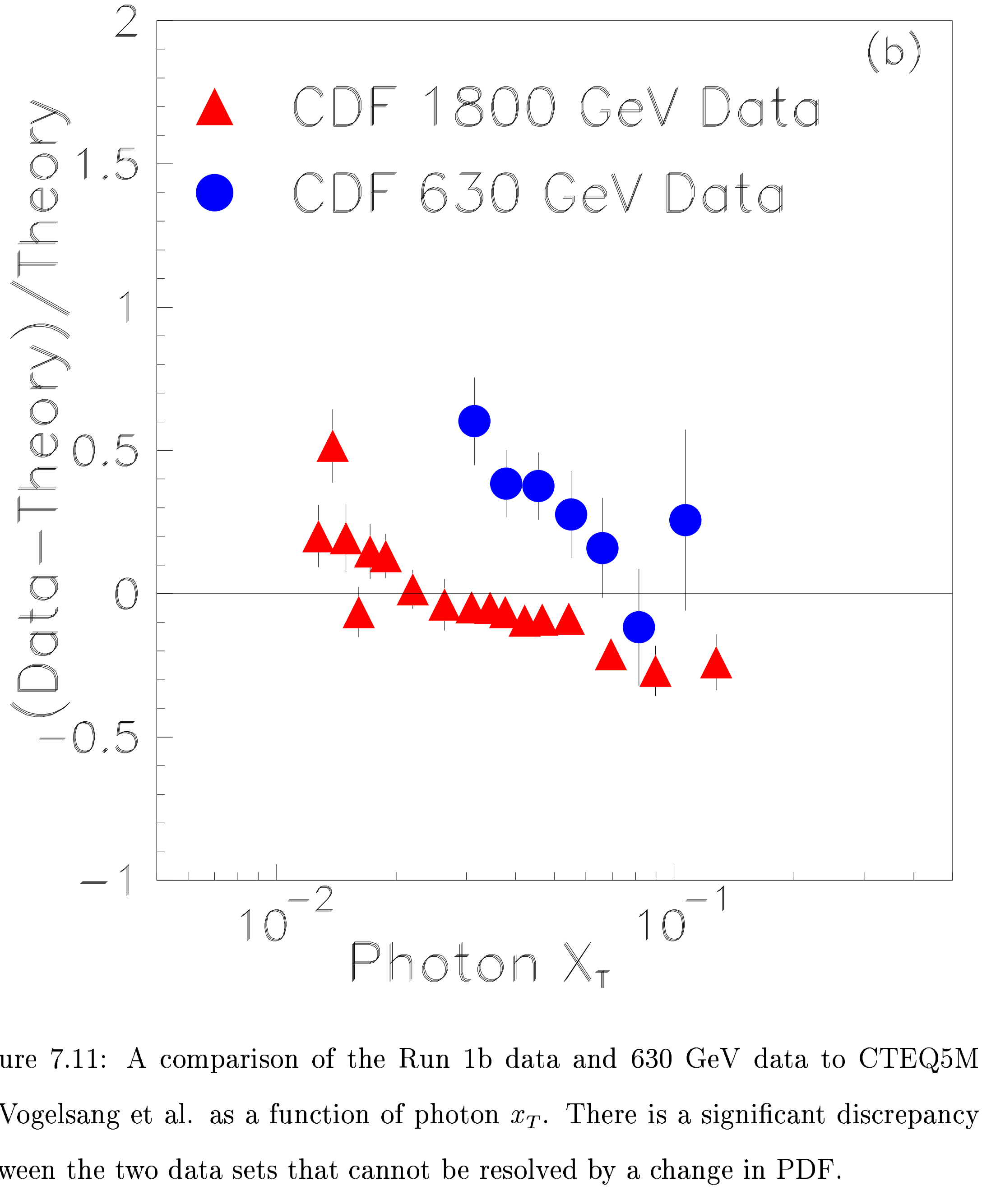

Figure 7.11: A comparison of the Run 1b data and 630 GeV data to CTEQ5M by Vogelsang et al. as a function of photon x_T. There is a significant discrepancy between the two data sets that cannot be resolved by a change in PDF.

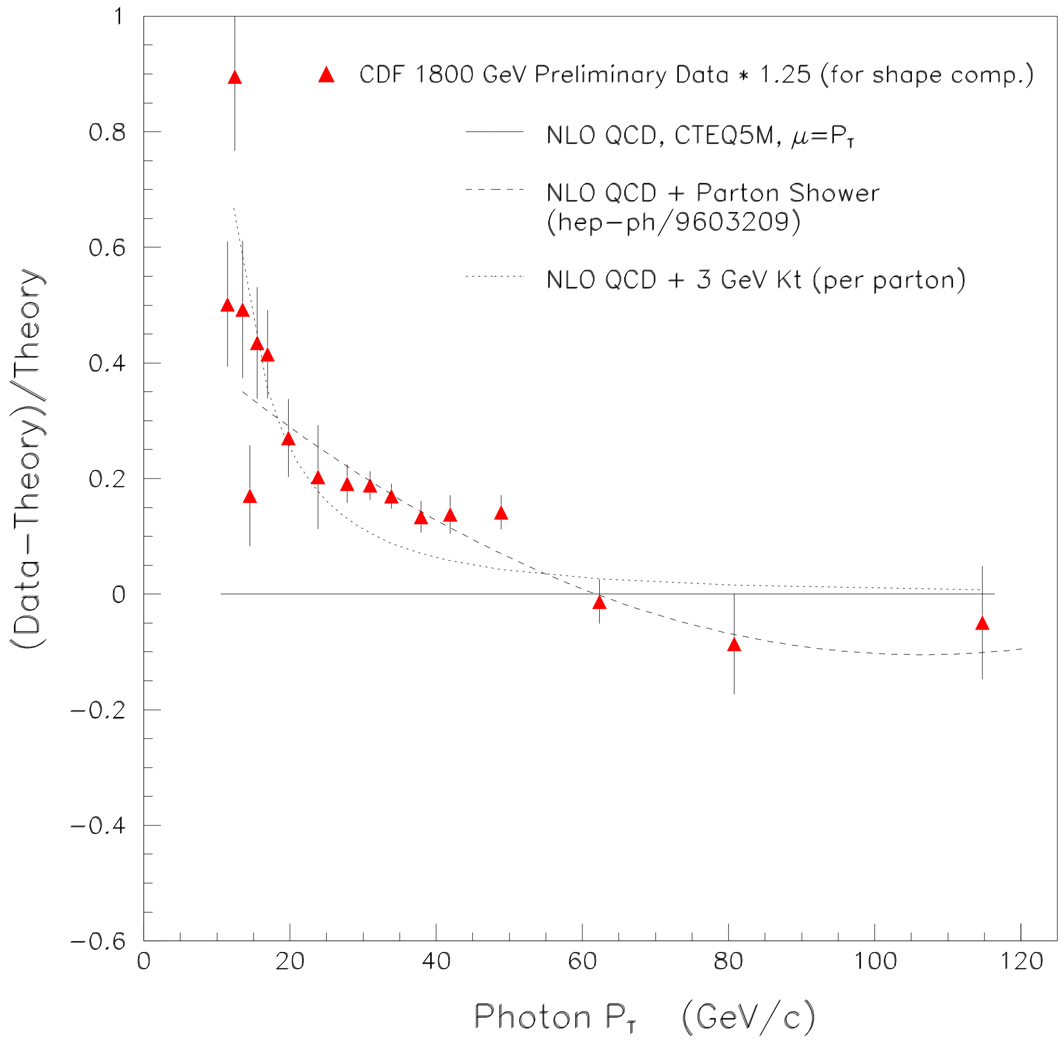

Figure 7.12: A comparison of the Run 1b data to CTEQ5M by Vogelsang et al. with the addition of a 3 GeV k_T correction and the parton shower algorithm. The data has been multiplied by 1.25 in order to do a shape comparison. CTEQ5M with parton shower algorithm is the best predictor of the shape.

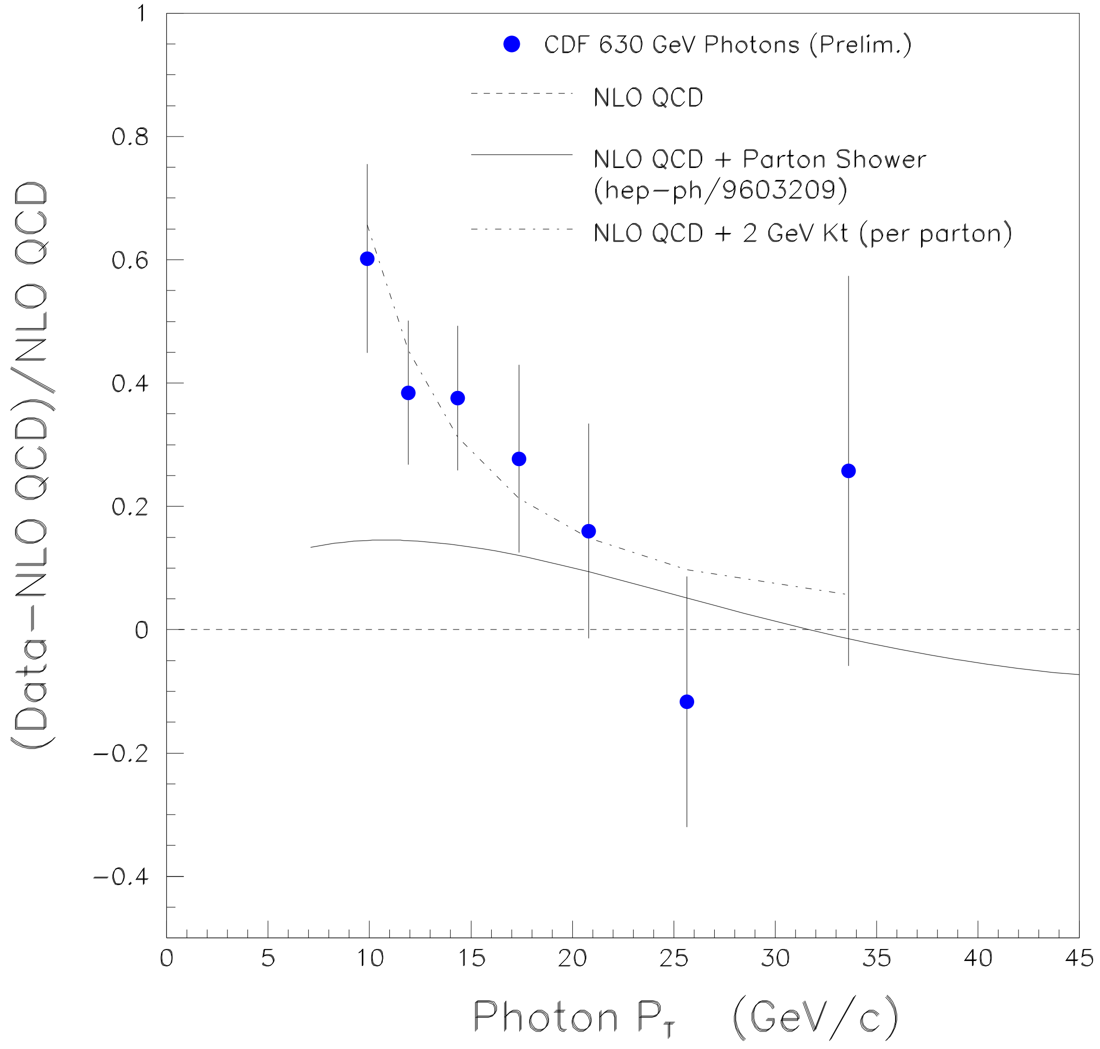

Figure 7.13: A comparison of the 630 GeV data to CTEQ5M by Vogelsang et al. with the addition of a 2 GeV k_T correction and the parton shower algorithm. The 3 GeV k_T correction best fits the data.

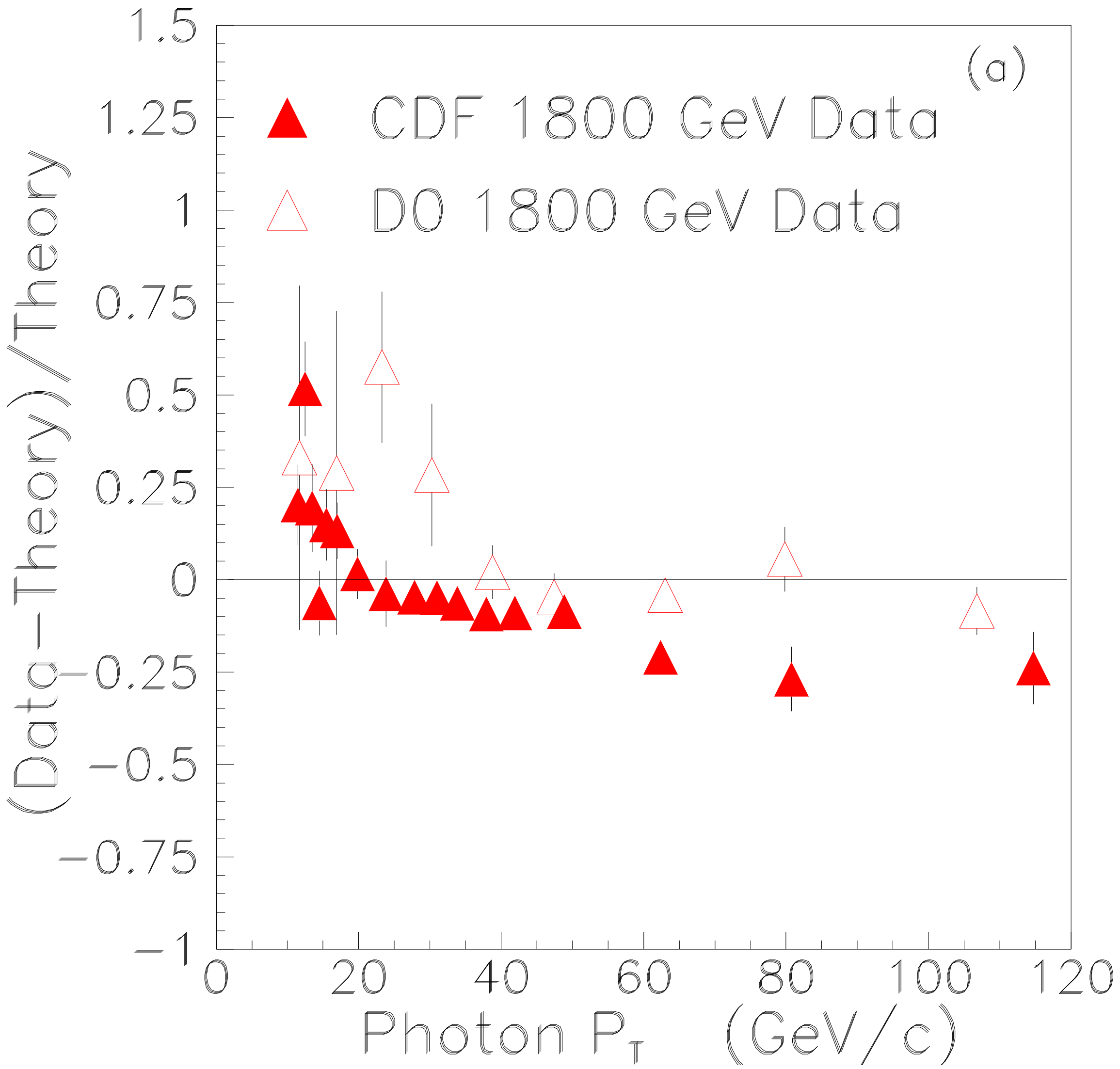

Figure 7.14: A comparison of the CDF and D0 Run 1b data sets to CTEQ5M by Vogelsang et al. as a function of photon P_T. The data sets are consistent with each other.

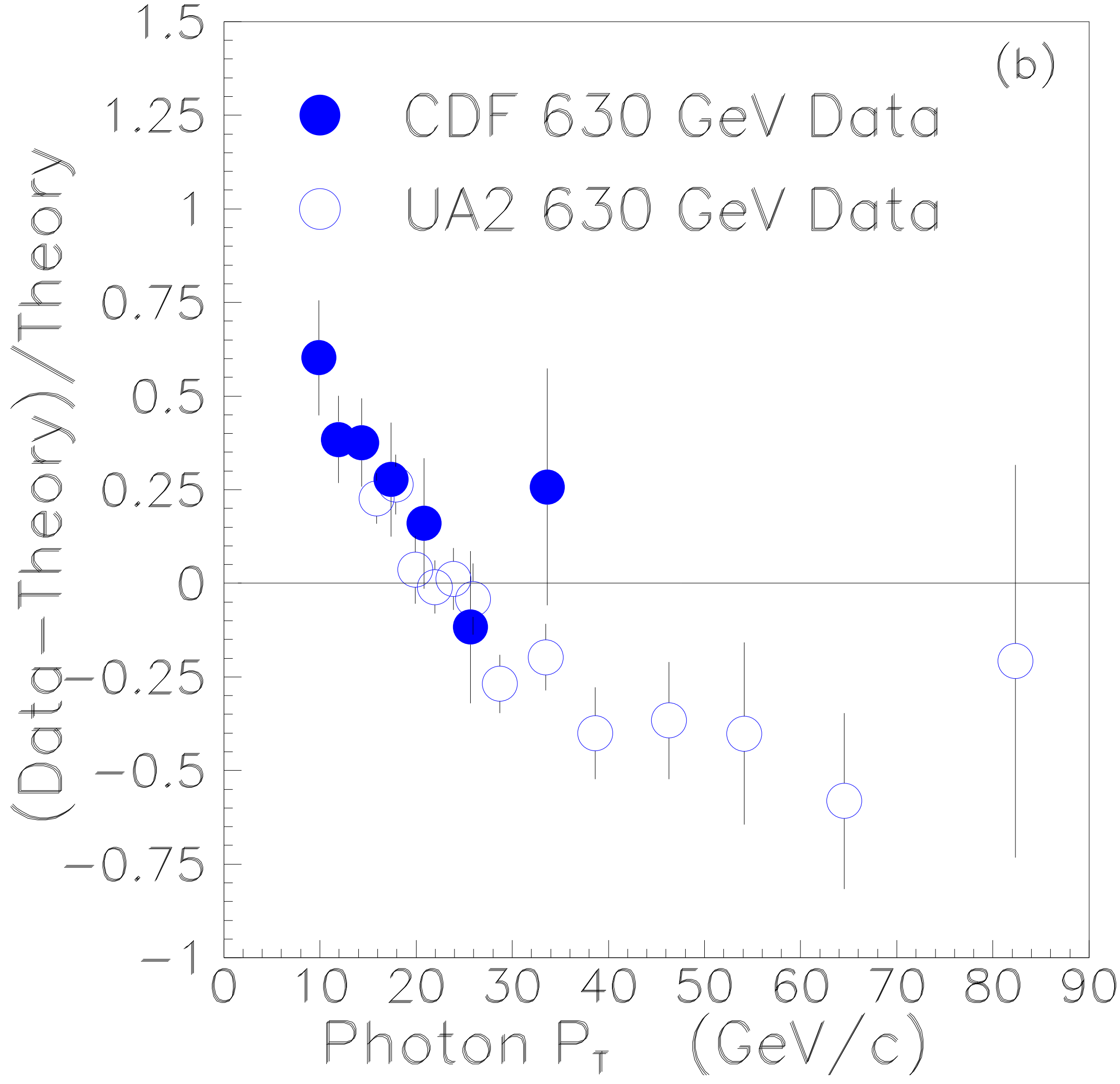

Figure 7.15: A comparison of the CDF and Ua2 630 GeV data sets to CTEQ5M by Vogelsang et al. as a function of photon P_T. The data sets are consistent with each other.

Bibliography

[1] D. Griffiths, *Introduction to Elementary Particles*, (John Wiley & Sons, Inc., New York, 1987).

[2] Review of Particle Physics, Phys. Rev. D (2000).

[3] R. Feynman, *Photon-Hadron Interactions*, (Benjamin, Inc., Massachusetts, 1972).

[4] J. Huston *et al.*, Phys. Rev. D **D51**, 6139 (1995).

[5] E. Laenen *et al.*, "Current Issues in Prompt Photon Production", eprint: hep-ph/00065352, June 2000.

[6] H. Baer and M. Reno, "Multiple Parton Emission Effects in Next-to-Leading-Order Direct Photon Production", eprint: hep-ph/9603209, March 29, 2001.

[7] S. D. Holmes FERMILAB-Conf-87/160 (unpublished).

[8] http://www.fnal.gov/pub/accelerator.html

[9] F. Abe, *et al.* (CDF Collaboration), Nucl. Inst. and Meth. **A 271**, 387 (1988), and the references therein.

[10] L. Balka,*et al.* (CDF Collaboration), Nucl. Inst. and Meth. **A 267**, 272 (1988).

[11] S. Kuhlmann, "Central Preradiator Detector Tests", CDF Note 1248.

[12] D. Wu and M. Cambell, "Calorimeter trigger applications, training, and assessment of a feed-forward neural net", CDF Note 2192.

[13] K. Byrum and A. B. Wickland, "The Level-2 Trigger Efficiency for 9 GeV Electrons in Run 1A", CDF Note 3120.

[14] D. Cronin-Hennessey and A. Baretvas "Luminosity at CDF" CDF Note 4721.

[15] A. Beretvas *et al.*, "Event z Vertex Cut Efficiency as a Luminosity Correction for Run 1b", CDF Note 5066

[16] S. Kuhlmann and A. Maghakian, "CDF Direct Photon Cross Sections at 630 GeV", CDF Note 3593.

[17] A. Maghakian, S. Kuhlmann, "Isolation Cut Efficiency in Direct Photon Analysis", CDF Note 2214.

[18] D. Partos and S. Kuhlmann, "Corrections to the Run 1B Photon Cross Section", CDF Note 5457.

[19] P. Wilson, "Calorimeter Isolation and Lateral Shower Leakage for Photons and Electrons", CDF Note 4170.

[20] R. Harris, R. Blair, and S. Kuhlmann, "Systematic Uncertainty in the Measurement of Isolated Direct Photons with the CES", CDF Note 1509.

[21] R. Harris, R. Blair, and S. Kuhlmann,"CES Response and χ^2 for 1990 Testbeam Electrons", CDF Note 1432

[22] S. Kuhlmann *et al.*, "Inclusive Photon Cross Section 1992", CDF Note 1963.

[23] F. Abe, *et al.*, (CDF Collaboration), Phys. Rev. **D 48,** 2998 (1993).

[24] F. Abe, *et al.*, (CDF Collaboration), Phys. Rev. Lett. **68,** 2734 (1992).

[25] R. Harris *et al.*, "Calibration of CPR Conversion Probability from Fully Reconstructed η and π^0 Mesons", CDF Note 2318.

[26] Y. Tsai, Rev. Mod. Phys. **46**, 815 (1974).

[27] R. Brun *et al.*, GEANT3, CERN DD/EE/84-1.

[28] R. Harris, "Definition of CES χ^2", CDF Note 1329.

[29] R. Harris, "Measurement of η/π^0 from Isolated Decays into Two Photons", CDF Note 1472.

[30] J. Alitti *et al.*, Phy. Lett. **B 263**, 544 (1991).

[31] D. Partos, S. Kuhlmann, and J. Lamoureux, "Run 1b Prompt Photon Cross Section", CDF note 4910.

[32] S. Kuhlmann *et al.*, "Calibration of CPR Conversion Probability from $\rho^{\pm} \rightarrow \pi^{\pm}\pi^0$ Decay", CDF Note 2478.

[33] QFL provides a fast detector simulation by parameterizing the detector response rather than deriving the response from first principles. It is possible to input single particles and their decays into QFL.

D. Brown, S. Kannappan, and M. Shapiro, "QFL Version 2: Improvements and Checks", CDF Note 753.

[34] M. Shapiro *et al.*, "A User's Guide to QFL" CDF Note 1810.

[35] F. Abe *et al.*, (CDF Collaboration), Phys. Rev. **D 43,** 2070 (1991).

[36] Jeff Owens (private communication).

[37] Werner Vogelsang (private communication).

[38] B. Abbot *et al.*, (D0 Collaboration), "The Isolated Photon Cross Section in $p\bar{p}$ Collisions at $\sqrt{s}$=1.8 TeV", eprint: hep-ex/9912017, Dec. 1999.